UNIVERSIDAD COMPLUTENSE DE MADRID
FACULTAD DE MEDICINA
Departamento de Radiología y Medicina Física

TESIS DOCTORAL

Multimodality functional imaging for adpative radiotherapy in cancer

Imágenes funcionales multimodales para radioterapia adaptativa en cáncer

MEMORIA PARA OPTAR AL GRADO DE DOCTOR

PRESENTADA POR

David Aramburu Núñez

Directores

Alfonso Calzado Cantera
Amita Shukla-Dave
Antonio López Medina

Madrid, 2017

UNIVERSIDAD COMPLUTENSE DE MADRID

FACULTAD DE MEDICINA

Programa de doctorado en Ciencias Biomédicas

Departamento de Radiología y Medicina Física

TESIS DOCTORAL

Multimodality Functional Imaging for Adaptive Radiotherapy in Cancer

Imágenes funcionales Multimodales para Radioterapia Adaptativa en Cáncer.

Memoria para optar al grado de doctor presentada por

David Aramburu Núñez

Directores

Alfonso Calzado Cantera

Amita Shukla-Dave

Antonio López Medina

Madrid, 2016

UNIVERSIDAD COMPLUTENSE DE MADRID

FACULTAD DE MEDICINA

Programa de doctorado en Ciencias Biomédicas

Departamento de Radiología y Medicina Física

TESIS DOCTORAL

Multimodality Functional Imaging for Adaptive Radiotherapy in Cancer

Imágenes funcionales Multimodales para Radioterapia Adaptativa en Cáncer.

Memoria para optar al grado de doctor presentada por

David Aramburu Núñez

Directores

Alfonso Calzado Cantera

Amita Shukla-Dave

Antonio López Medina

Madrid, 2016

A papá, mamá y Marta

Agradecimientos/Acknowledgments

Esta es una de las partes que me hace mucha ilusión escribir en mi tesis doctoral. No se si normalmente solemos decirles a los demás lo valiosos y de ayuda que han podido llegar a ser a lo largo de un proceso profesional y científico tan duro de conseguir. Aun haciéndolo, tengo la sensación de que la tinta, convierte a ese agradecimiento si cabe en aun mas verdadero. Pero, ¿qué es lo que se debe agradecer?; la carrera profesional, científica y vital de una persona está marcada por numerosos momentos que los valoramos a través de diferentes estados de ánimo. Alegría, tristeza, entusiasmo, decepción, ilusión, confusión, satisfacción, frustración, cansancio, inseguridad, miedo, éxito y fracaso. Todos tienen un antídoto siendo las personas que causal o casualmente te acompañan, condicionantes y determinantes de su efecto. Es cierto que caminamos solos y que somos el resultado de nuestros actos, sin embargo ya en nuestros primeros momentos de vida ha habido un apoyo o un empujón para que saliésemos adelante.

No tengo la capacidad de recordar mis primeros pasos, pero sé que mis padres estuvieron ahí sujetándome y levantándome cada vez que me caía, animándome para que consiguiese uno de los primeros objetivos vitales, andar. ¿Por qué lo sé? porque desde aquel momento y hasta el día de hoy han seguido haciéndolo, estando a mi lado para ayudarme a superar esos estados de ánimo. Ellos son el símbolo de la superación y el trabajo duro, la admiración que siento por ellos no para de crecer, al igual que la que siento por mi hermana, ella es la persona mas inteligente de la familia y cada día me sorprende con algo nuevo, gracias por aguantarme y apoyarme "Enana". Los tres son las personas más importantes y valiosas de mi vida, sin sus figuras no estaría escribiendo estas palabras. Por supuesto, mi Abuela por ser "la mejor Buela del mundo", Juan por su sentido de la vida, Toni por su Bondad, Lola por ser la alegría de la fiesta, la familia de Ribadeo por ser mi segundo hogar, Ayanta, Canna y Wolf por haber sido y ser ¡Guau! sin palabras; todos ellos completan el círculo familiar que me ha apoyado en esta larga y dura carrera. Claro que no me puedo olvidar de mi segunda familia, mis Amigos y Amigas, ellos son los mejores y ellas son imprescindibles. Todas estas personas son clave en la superación de las dificul-

tades vitales, pero las dificultades profesionales y científicas requieren de personas que tengan ciertas capacidades que complementan a la perfección la ayuda necesaria para solventarlas y en ese proceso se conviertan también en apoyos vitales. Como el Dr. Antonio López Medina, Dr. Alfonso Calzado Cantera y Dra. Amita Shukla-Dave, ellos representan el orden cronológico y espacial de esta tesis con su comienzo en España y su fin en Estados Unidos. **Amita** thank you for opening the doors of the USA to me, for giving me the opportunity to work in your group, for teaching teach me that in NY, September is around the corner from January and for your support and vision in this Ph.D. thesis. **Antonio** por enseñarme lo que es ARTFIBio, por empujarme y mantener viva esta carrera, por ser científicamente valiente, por mostrarme la ESTRO y por hacerme comprender que significa DA. **Alfonso** gracias por aceptar esta propuesta, por darle sustento, rigor, por hacer que las cosas parezcan fáciles y por ser tan cercano y accesible. Y en ese viaje espacial y temporal que ha hecho esta tesis numerosos colaboradores han sido esenciales. Como **Ramesh,** thank you for helping me to understand DCE, for your valuable time, and for being an awesome coworker. **Erica** your edits in "this" were very helpful. **Moisés** por ADC vs K^{trans} y por ser un R mayor de diez. **Iago, Francisco, Yonggang** and **Carlos** for coding such great software programs. **Vaios** for the contours and great learning sessions every time we check patients. **Iñigo, Virginia** y **Victor** por el apoyo clínico**. Pacientes** y **Research Assistants** gracias por confiar en la Ciencia, thank you for trust in Science. **SIHO** por su disponibilidad para construir nuevos dispositivos. A las instituciones **Hospital Meixoeiro de Vigo, Universidad Complutense de Madrid, Instituto de Salud Carlos III, BIOCAPS, Xunta de Galicia** y **Memorial Sloan-Kettering Cancer Center (MSKCC)** through an internal IMRS grant. A todos ellos gracias por el apoyo a los estudios que se han desarrollado en esta tesis. También me gustaría agradecer el convenio **AAPM-SEFM** que a través de la **Dra. Caridad Borras** y la **Dra. Doracy Fontela** me han dado la oportunidad de acceder a centro tan prestigioso y único en el mundo como es MSKCC. Y como un paso lleva a otro, mi residencia de Radiofísica Hospitalaria ha coexistido con esta tesis, por lo que aprovecho para agradecer a **Ana** todo su apoyo cuando prueba tan exigente como el RFIR parecía un muro imposible de superar. A **Lore** por enseñarme a gatear y andar en el campo tan maravilloso de la Física Médica. A **Manuel** por en-

tender lo importante del trabajo científico durante el periodo de residencia. A **Teijeiro**, **Benito**, **Julio**, **Daniela**, **Francisco**, **Alfaya**, **Adrian**, **Rocío** por ser mentores y permitirnos ARTFIBear de vez en cuando, **Residentes, Médicos, Enfermeras** y Técnicos de Oncología **radioterápica** y a **Galaria** en general por hacer que tenga siempre muchas ganas de volver.

Puede que el apoyo científico, profesional, laboral, anímico, visionario, realista y ocioso sean los antídotos a todos los estados de ánimo que nos afectan cuando nos proponemos objetivos desafiantes, pero sin ninguna duda estos son los apoyos que creo debemos agradecer. Estas palabras han querido expresar mi más sincero y profundo agradecimiento a todas y todos los que han hecho posible que pueda presentar esta tesis doctoral. ¡Muchas Gracias a todos!

Index

Contents

SUMMARY

Introduction

Contemporary techniques in radiotherapy (RT), which include intensity modulated radiation therapy (IMRT), volumetric modulated arc therapy (VMAT), and proton and heavy ion therapy, enable the delivery of high dose coverage of tumor volume while sparing healthy surrounding tissue. At the same time, imaging techniques such as positron emission tomography/computed tomography (PET/CT) and magnetic resonance imaging (MRI) have evolved to allow for the visualization of a wide range of pathophysiological characteristics of tumor, from metabolism to perfusion. Diffusion-weighted (DW)-MRI provides an estimate of the diffusivity of water molecules in tissue, with the quantitative imaging metric apparent diffusion coefficient (ADC) providing valuable information about changes in tissue cellularity associated with tumors in addition to predictions of treatment outcomes after RT. Dynamic contrast enhanced (DCE-) MRI provides information on tumor perfusion using contrast agents (CA) to assess the vascular properties of tissue through a gadolinium (Gd)-based CA, also associated with therapy response. On the other hand, PET/CT imaging relies on specific radiotracers, with 18-fluorine fluorodeoxyglucose (^{18}F-FDG) being the most widely used in cancer. This radiotracer can be used to measure metabolic and functional properties of tumors.

The combination of functional and molecular information that can be derived from MRI and PET/CT imaging techniques has led to the development of new tools that go beyond uniform dose delivery. Clinical practice in the coming years is expected to progress further down the path of RT treatment adapted to an individualized response - turning from prescribing dose to volume towards prescribing dose to optimizing treatment, minimizing the number of tumoral cells that survive treatment with acceptable comorbidity. This thesis will focus on the building blocks of adaptive RT for Human Papilloma Virus negative (HPV-) Head and Neck Squamous Cell Carcinoma (HNSCC) and Brain Metastases (BM) patients.

Motivation and objectives

In the modern era of adaptive RT, it has become vital to understand how different functional imaging techniques interact and link together in tumors. There is an urgent need to assess tumor response during treatment using functional imaging. Hence, in clinical settings it is extremely essential to accurately assess whether or not a tumor has been successfully treated and whether the tumor requires additional treatment. Quantitative Imaging Biomarkers (QIBs) may play a crucial role in deciphering treatment efficacy. However, the implementation of these functional techniques is one of the most challenging issues in RT.

The objectives of this dissertation are divided into the three parts below, each corresponding to its respective study.

Part I - DW-MRI and ^{18}F FDG PET/CT are two valuable imaging techniques that may help build the framework for adaptive radiotherapy based on functional images in the future by investigating tumor cellularity and glucose metabolism before, during and after RT in HPV- HNSCC.

Part II - A constant challenge in functional imaging is the improvement of image quality and the reduction of distortion to obtain quality images for radiation treatment planning and delivery. This study investigates the application of the reversed gradient method in DW-MRI for the reduction of geometric distortion and measurement of accurate ADC.

Part III – a. For QIBs to be used in Adaptive RT, it is a prerequisite to perform exhaustive phantom studies detailing the repeatability and reproducibility of the functional imaging technique.

Part III – b. Intra Voxel Incoherent Motion (IVIM) DW- and DCE- MRI are two promising imaging techniques that may help evaluate early treatment response in BM patients treated with SRS.

Results

Results from the studies related to the objectives above are divided into three corresponding parts. The studies in **Part I** and **Part II** were performed at Meixoeiro University Hospital of Vigo, Spain. The study in **Part III a.** and **Part III b.** was conducted at Memorial Sloan-Kettering Cancer Center, USA.

Part I - The study showed an increase in the relative percent change in ADC at week 2 for the patient with no evidence of disease (NED) reflecting a good response to treatment in both primary tumor and neck nodal metastases. ADC histograms showed microstructural heterogeneity in primary tumor and neck nodal metastases in the three groups NED, dead of disease (DOD) and alive with disease (AWD). In addition, in the NED patient, a shift towards high ADC values for both primary tumor and neck nodal metastases reflected the improved pathologic response to RT. The ADC relative percent change trends shown for primary tumor and neck nodal metastases depict the different responses to treatment, suggesting the possibility of identifying at an early stage patients with good or bad prognoses to individualize and adapt RT treatment.

Part II - In this study, a new phantom was specifically designed to evaluate geometrical distortion. The visual improvement in registration with the reversed gradient method applied was notable, showing a better fit with the real anatomic position indicated by CT. The numerical quantification of distortion calculated through the mutual information metric in undistorted DW-MRI images for both phantom and patients with different b-values showed an improvement in the mutual information metric with respect to distorted images.

Part III – a. This study assessed the repeatability, reproducibility and quantitative quality control of ADC measurements across vendors of the same field

strength using a standardized acquisition protocol and a temperature-controlled fluid phantom. ADC values acquired for the phantom from different vendors showed no statistical difference between the four measurements performed within and across vendors and between different ROIs. In addition, coefficient of variation of the repeatability measurements for each vendor was < 2%.

Part III – b. The present study showed a significantly strong positive correlation between mean ADC and mean true diffusion coefficent (D), mean perfusion factor (f) and mean plasma volume fraction (v_p) and volume transfer constant (K^{trans}), mean K^{trans} and mean extracellular volume fraction (v_e). ADC, D and K^{trans} histograms display microstructural and microvasculature heterogeneity in tumor tissue. The distribution curves of early post-treatment ADC and K^{trans} show a shift towards higher ADC and lower K^{trans} values, reflecting the improved pathologic response to SRS. In terms of response to treatment, in a long term follow up of 12 months, ADC values and tumor volumes showed the same behavior.

Conclusions

The conclusions drawn from these results have also been divided into three corresponding parts.

Part I - Multimodality imaging in HPV- HNSCC suggests that tumor cell density is inversely proportional to glucose metabolism. The survival status and functional metrics show different trends.

Part II - A clear improvement in mutual information for registration processes were observed when the reversed gradient method was applied. Thus, this method improves registration and provides accurate ADC measurement in tumors.

Part III – a. The establishment of methodological procedures and the standardization of data acquisition conditions are needed for the systematic reproducibility and repeatability of DW-MRI studies.

Part III – b. Early changes in diffusion and perfusion imaging metrics to SRS can be detected in a manner similar to the changes associated with radiation effects in other studies. Predicting response at the early stages would be advantageous over methods that require long term clinical follow up and will help to individualize and adapt RT treatment.

RESUMEN

Introducción

Hoy en día, novedosas técnicas radioterápicas como la radioterapia de intensidad modulada (IMRT), la arcoterapia volumétrica modulada (VMAT), la protonterapia y la hadronterapia permiten administrar una alta dosis de cobertura al volumen tumoral evitando el tejido sano circundante. Al mismo tiempo, técnicas de imagen como la tomografía de emisión de positrones-tomografía computarizada (PET/CT) y las imágenes por resonancia magnética (MRI) han madurado permitiendo visualizar un amplio rango de características pato-fisiológicas del tumor, desde el metabolismo a la perfusión. La técnica Diffusion Weighted (DW-) MRI proporciona una estimación de la difusión de las moléculas de agua en tejido a través de la métrica de imagen cuantitativa, coeficiente de difusión aparente (ADC). Dicha métrica proporciona valiosa información tanto acerca de la celularidad del tumor así como un valioso indicador de la respuesta tumoral al tratamiento con radioterapia. Además, la técnica dynamic contrast enhanced (DCE-) MRI proporciona información de la perfusión tumoral utilizando medios de contraste; las métricas derivadas de esta técnica nos permiten evaluar las propiedades vasculares del tejido a través de un medio de contraste basado en gadolinio, estas métricas están también asociadas con la respuesta al tratamiento. Por otro lado, las imágenes de PET/CT dependen de radiotrazadores específicos, siendo ^{18}F-labeled fluorodeoxyglucose (^{18}F-FDG) el más extendido y usado en cáncer. Este radiotrazador puede ser usado para medir las propiedades metabólicas y funcionales de los tumores.

La combinación de información funcional y molecular que puede ser obtenida de técnicas de imagen como MRI y PET/CT, ha conllevado al desarrollo de nuevas herramientas que van mas allá de la administración de una dosis uniforme. Se espera que la práctica clínica

en los próximos años evolucione, convirtiendo la dosis prescrita al volumen hacia la prescripción de dosis para optimizar el tratamiento, minimizando el número de células tumorales que sobreviven al tratamiento con comorbilidad aceptable y adaptando el tratamiento radioterápico a una respuesta individualizada. Esta tesis se enfocara en el elemento esencial de la radioterapia adaptativa basada en imágenes funcionales para Carcinomas de cabeza y cuello de células escamosas (HNSCC) y metástasis cerebrales (BM).

Motivación y Objetivos

En la era moderna de la radioterapia adaptativa, se ha convertido de vital importancia entender como diferentes técnicas de imagen funcional interactúan en su aplicación a tumores. Hay una necesidad urgente de evaluar la respuesta tumoral durante el tratamiento utilizando imágenes funcionales. Por lo tanto en la práctica clínica es extremadamente esencial evaluar con precisión si un tumor ha sido tratado con éxito o si el tumor necesita de tratamiento adicional. Los biomarcadores de imagen cuantitativa deben jugar un papel crucial en descifrar la eficacia del tratamiento. Sin embargo, la implementación de estas técnicas funcionales es uno de los aspectos más desafiantes en radioterapia.

Los objetivos de esta tesis están divididos en tres partes correspondiéndose cada una a su respectivo estudio.

Parte I – DW-MRI y ^{18}F FDG PET/CT son dos valiosas técnicas de imagen que pueden ayudar a construir el marco de la futura radioterapia adaptativa basada en imágenes funcionales, investigando la celularidad del tumor y el metabolismo de la glucosa antes, durante y después del tratamiento radioterápico, en cánceres de cabeza y cuello de células escamosas en pacientes negativos al virus papiloma humano (HPV-).

Parte II – Un reto constante en imagen funcional es el de mejorar la calidad de imagen y reducir la distorsión para obtener imágenes de calidad para la

planificación y tratamiento en radioterapia. Este estudio investiga la aplicación del método de los gradientes invertidos in DW-MRI para reducir la distorsión geométrica y medir con precisión el ADC.

Parte III – a. Para usar biomarcadores de imagen cuantitativa en radioterapia adaptativa, es un prerrequisito realizar exhaustivos estudios con maniquís que detallen la repetitividad y reproducibilidad de la técnica de imagen funcional.

Parte III – b. Intravoxel Incoherent Motion DW-MRI y DCE-MRI son dos prometedoras técnicas de imagen que pueden ayudar a evaluar la respuesta al tratamiento temprana en pacientes con BM tratados con radiocirugía estereotáctica (SRS).

Resultados

Los resultados obtenidos de los objetivos detallados por partes anteriormente están divididos igualmente en tres partes. Los estudios de la Parte I y la Parte II se han desarrollado en el Hospital Meixoeiro de Vigo, España. El estudio de la Parte III a. y b. se han desarrollado en Memorial Sloan-Kettering Cancer Center, USA.

Parte I – Este estudio muestra un incremento en el cambio relativo en porcentaje de ADC en la segunda semana de tratamiento para un paciente sin evidencia de enfermedad (NED), en comparación con pacientes muertos por enfermedad (DOD) y vivos pero con enfermedad (AWD), tanto en tumor primario como en nódulos metastásicos de cuello, reflejando una buena respuesta al tratamiento. Los histogramas de ADC muestran heterogeneidad microestructural en el tumor primario y en los nódulos metastásicos de cuello, en los tres grupos (NED, DOD y AWD). Además, en el paciente NED un desplazamiento hacia valores mas altos de ADC

en el tumor primario y en el nódulo metastásico de cuello, reflejan la mejora patológica en la respuesta a radioterapia. Las tendencias del cambio relativo en porcentaje de ADC para el tumor primario y el nódulo metastásico de cuello describen diferentes respuestas al tratamiento sugiriendo que la identificación en un estado temprano de pacientes con buen o mal pronóstico pude ayudar a la individualización y adaptación del tratamiento radioterápico.

Parte II – En esta segunda parte, un novedoso maniquí fue específicamente diseñado para evaluar la distorsión geométrica. La mejora visual en el registro de imágenes aplicando el método de los gradientes invertidos, mostró un mejor ajuste a la posición anatómica real en la CT. La cuantificación numérica de la distorsión calculada a través de la métrica de información mutua en imágenes corregidas de DW-MRI, tanto para el maniquí como para los pacientes mostró una mejora con respecto a las imágenes no corregidas.

Parte III – a. Este estudio evaluó la repetitividad, reproducibilidad y el control de calidad cuantitativo en medidas de ADC entre resonancias de distinta marca de la misma intensidad de campo magnético, utilizando un protocolo de adquisición estandarizado y un maniquí liquido de temperatura controlada. Los valores adquiridos de ADC para el maniquí en diferentes marcas, no mostraron diferencias significativas entre las cuatro medidas realizadas en cada una de ellas y entre marcas. Por otro lado se ha obtenido un coeficiente de variación menor del 2% en las medidas de repetitividad para cada marca.

Parte III – b. El presente estudio mostró una fuerte correlación positiva y significativa entre ADC y D, f y v_p, f y K^{trans}, K^{trans} y v_e. Los histogramas de ADC, D y K^{trans} reflejan la heterogeneidad de la microestructura y la microvas-

culatura del tejido tumoral. Las curvas de distribución en un momento temprano postratamiento muestran para ADC y K^{trans} un desplazamiento hacia valores elevados de ADC y bajos de K^{trans}, reflejando la mejora de la respuesta patológica a la SRS. En términos de respuesta al tratamiento, en un seguimiento a 12 meses de los pacientes postratamiento, los valores de ADC y de volumen tumoral muestran un mismo comportamiento.

Conclusiones

Las conclusiones relacionadas con los resultados están divididas en tres partes:

Parte I – Las imágenes multimodales en HPV- HNSCC sugieren que la densidad de células tumorales es inversamente proporcional al metabolismo de la glucosa. Se han observado diferentes tendencias en las diferentes métricas dependiendo del estatus de supervivencia de los pacientes estudiados.

Parte II – Se observa una clara mejora en la información mutua para el proceso de registro de imágenes cuando aplicamos el método de los gradientes invertidos. Este método por lo tanto, mejora el registro ayudando a una medida más precisa de ADC en tumores.

Parte III – a. Es necesario un procedimiento específico y estandarizado de las condiciones de adquisición de datos para un sistemático nivel de reproducibilidad en estudios de DWMRI.

Parte III – b. Cambios tempranos al tratamiento de SRS en las métricas de difusión y perfusión, pueden ser detectados de una manera similar a los cambios que se han visto por efectos de la radiación en otros estudios. La predic-

ción de la respuesta en momentos tempranos, seria ventajosa con respecto a métodos que requieren largos plazos de detección en el seguimiento de los pacientes y ayudara a individualizar y adaptar el tratamiento radioterápico.

List of Key Acronyms

^{18}F-FDG Fluorine-18 Fludeoxyglucose

Δ	Relative percentage change
ADC	Apparent diffusion coefficient
AIF	Arterial input function
AWD	Alive with disease
BM	Brain Metastases
CA	Contrast agent
CRT	Chemo-radiation therapy
D	True diffusion coefficient
D*	Pseudo-diffusion coefficient
DCE-MRI	Dynamic contrast enhanced magnetic resonance imaging
DOC	Dead of other causes
DOD	Dead of disease
DW-MRI	Diffusion-weighted magnetic resonance imaging
EPI	Echo planar imaging
f	Perfusion factor
FOV	Field of view
Gd	Gadolinium

HNC	Head and neck cancer
HNSCC	Head and Neck Squamous Cell Carcinoma
HPV-	Human papillomavirus negative
HPV+	Human papillomavirus positive
IMRT	Intensity modulated radiation therapy
IVIM	Intravoxel incoherent motion
$\mathbf{k_{ep}}$	Rate constant from extracellular to intravascular space
$\mathbf{K^{trans}}$	Volume transfer constant
MRI	Magnetic resonance imaging
NED	No evidence of disease
NEX	Number of excitations
PET/CT	Positron emission tomography/computed tomography
qMRI	Quantitative MRI
QIB	Quantitative Imaging Biomarkers
ROI	Region of interest
RT	Radiotherapy
SI	Signal intensity
SM	Standard model
SRS	Stereotactic radiosurgery
SSEPI	Single-shot Spin-echo Echo Planar Imaging
TE	Echo time

TR	Repetition time
Tx	Treatment
$\mathbf{v_e}$	Extracellular volume fraction
$\mathbf{v_p}$	Plasma volume fraction
w	Weighted
Wk	Week

Chapter I

Chapter I – Introduction

1. Adaptive radiotherapy based on functional imaging

Over the past 60 years, transformative developments have occurred in the practice of radiotherapy (RT) in oncology. These include the Cobalt-60 teletherapy unit, medical linear accelerators, treatment simulators, afterloading and remote afterloading techniques, radium and radon substitutes, computerized treatment planning, intensity modulated radiation therapy (IMRT) and image-guided RT, among others (1). These major technological advances have significantly impacted the practice of radiotherapy and incrementally improved its therapeutic efficacy by more accurate dose delivery to tumors. What is needed today is a better understanding of a individual tumor's response to RT that would allow a more tailored prescription. Functional imaging with positron emission tomography/computed tomography (PET/CT) and magnetic resonance imaging (MRI) have shown promise in clinical applications ranging from prognosis to prediction of treatment response in cancer patients (2, 3). Hence RT coupled with functional information is a key tool for improved treatment in radiation oncology (4, 5). This thesis will focus on the role of functional imaging in future adaptive radiotherapy in cancer by providing quantitative imaging biomarkers for individualized clinical practice in contemporary radiation oncology. The three novel studies that constitute this thesis are an attempt to deepen our understanding of how to manage and use valuable information derived from the above mentioned functional imaging modalities.

1.1. Current functional imaging status in RT

Today, RT techniques offer unprecedented levels of flexibility and freedom in treatment planning and in radiation dose delivery. These techniques – which include IMRT, volumetric modulated arc therapy (VMAT), and proton and heavy ion therapy –

enable high dose coverage of tumor volume while sparing healthy surrounding tissue, even allowing for the escalation of radiation dose to radioresistant areas of gross tumor volume (GTV) without increasing RT-induced side effects (6).

At the same time, imaging techniques such as PET/CT and MRI have matured to the extent where it is now possible to better delineate the tumor volume and visualize a wide range of the pathophysiological characteristics of tumor, from metabolism to perfusion (7, 8). Diffusion-weighted (DW)-MRI provides an estimate of the diffusivity of water molecules in tissue, while both dynamic contrast enhanced (DCE)-CT and DCE-MRI provide information on tissue perfusion using contrast agents (CA). On the other hand, PET/CT imaging relies on specific radiotracers which can be used to measure metabolic and functional properties of tissues. Given the scope and depth of information that can be made available through the integration of these imaging techniques, functional imaging today presents a tremendous opportunity in furthering individualized RT treatment planning in cancer.

DW-MRI and DCE-MRI both have remarkable potential in enhancing RT outcomes (9, 10). By assessing the diffusion properties of water molecules in tissue, DW-MRI allows to quantify voxel-based diffusion coefficients, or signal-derived quantitative maps of the quantitative imaging metric, apparent diffusion coefficient (ADC), which varies from tissue to tissue. ADC values provide valuable information about changes in tissue cellularity associated with tumors; as cell density increases, the ADC decreases as the movement of water molecules becomes more restricted. It has been reported that ADC has potential in characterize tumors as well as in predicting treatment outcomes after RT (9, 11-16). DCE-MRI, on the other hand, assesses the vascular properties of tissue through a gadolinium (Gd)-based CA, which allows the acquisition of a dynamic set of images. DCE-MRI also has been associated with therapy response (10, 17). A recent clinical study confirmed that DCE-MRI data can successfully be used for response assessment after therapy has been completed (18).

PET complements the information provided by CT and MRI techniques through the provision of information about the molecular and metabolic status of tumors. PET's unique ability to assess molecular alterations without varying fundamental molecular and biochemical processes is possible due to the use of molecules (radiopharmaceuticals) that are labeled with radioactive nuclides. Fluorine-18 fluorodeoxyglucose (^{18}F-FDG) is the most widely used radiopharmaceutical for PET studies of cancer since its invention in 1978 (19). As a glucose analogue, ^{18}F-FDG concentrates in cells using glucose as an energy source in cellular metabolic processes; it is thus able to trace an increased dependence on glucose, (i.e. an increase in glycolytic rates), a key pathophysiological alteration associated with cancer cells. PET/CT's utility in RT treatment planning, primarily in regards to tumor grading and staging, is widely acknowledged today (20, 21).

Recent studies have explored the use of ^{18}F-FDG PET/CT as a tool to enhance the accuracy of target volume delineation, and a large number of studies and research projects have developed and validated automatic and semi-automatic algorithms for the accurate delineation of RT target volumes based on ^{18}F-FDG PET (7, 22). Some clinical trials are currently under way to test the potential of redistributing radiation dose to the most metabolically avid parts of tumor in non small-cell lung cancer and in head and neck cancer (HNC) (23, 24). Radiotracers other than ^{18}F-FDG are also being studied for their role in detecting tumor hypoxia (25-27), a key factor in radiation resistance and of consequent significance in potential RT adaptations. These radiotracers include ^{18}F-fluoromisonidazole (^{18}F-FMISO), ^{18}F-fluoroazomycin arabinoside (^{18}F-FAZA, and ^{18}F-flortanidazole (^{18}F-HX4) (28-30).

The combination of functional and molecular information that can be derived from CT, MRI and PET imaging techniques has paved the way for considerable improvements to the accuracy of tumor delineation and subvolume determination. Complementary information obtained from functional and molecular images do not only improve overall accuracy in target volume delineation, but it also has led to the develop-

ment of new tools that go beyond uniform dose delivery. Dose painting, the prescription and delivery of a nonuniform radiation dose to targeted volume based on molecular and functional images, is a relatively new paradigm in radiation oncology made possible by these new techniques in functional imaging, as they identify high risk tumor subvolumes that can be specifically targeted by higher radiation doses (31, 32). Moreover, RT treatment machines with MR integrated into the RT system are being tested through collaborative partnerships between hospitals and private medical technology vendors, with the imminent incorporation of these new technologies into regular clinical workflow (33, 34). Clinical practice in the coming years is expected to evolve - turning from prescribing dose to volume towards prescribing dose to optimize treatment, minimizing the number of tumoral cells that survive treatment with acceptable comorbidity and adapting RT treatment to an individualized response. This thesis will focus on the building blocks of adaptive RT for Head and Neck Squamous Cell Carcinoma (HNSCC) and Brain Metastases (BM).

1.2. Role of Quantitative Imaging Biomarkers in radiotherapy

In quantitative imaging, biomarkers allow information about a biological process to be extracted from an image; this imaged characteristic allows objective measurement and evaluation of a biological process, pathological process, or response to a therapeutic intervention, similar to laboratory or physiological assays (35). To ensure an active role for imaging biomarkers in future iterations of adaptive RT based on functional imaging, a rigorous evaluation of their technical and clinical performance is necessary. Technical performance for a given biomarker, or its performance in reference objects or subjects under controlled conditions, can form the basis for additional research to determine clinical validation and clinical usefulness, with the ultimate aim of determining which biomarkers are clinically relevant.

The term Quantitative Imaging Biomarker (QIB) is generally defined as "an objective characteristic derived from an in vivo image measured on a ratio or interval scale as indicators of normal biological processes, pathogenic processes or a response to a therapeutic intervention." (36, 37). The standardization and optimization of quantitative imaging is still an ongoing process, although the Radiological Society of North America (RSNA)'s Quantitative Imaging Biomarker Alliance (QIBA) is developing profiles that provide a useful starting point for selected QIBs. For the purposes of this thesis, the following QIBs have been used:

1.2.1. Quantitative MRI: Diffusion-Weighted MRI and Dynamic Contrast Enhanced MRI

Recent advances in the field of MRI include new developments in hardware, MR acquisition pulse sequences and MR data analysis algorithms (2, 38-40). Lately there has been a timely focus on Quantitative MRI (qMRI) as its utility and applications increase in the clinical realm, particularly in the field of oncology. As qMRI is a technique to measure specific image properties, it is necessary to maximize the sensitivity, specificity and accuracy of the imaging metric in order to obtain the best possible quantification of a specific property (2, 38-40).

1.2.1.1. **Diffusion-Weighted MRI**

As mentioned above, DW-MRI measures also the Brownian movement of water molecules; however, the movement of water molecules is not free in the human body, being limited by different cells, membranes and macromolecular components.

The use of two magnetic field gradient pulses in a T2-weighted spin-echo sequence allow to generate MR signals sensitive to diffusion (41). These gradient pulses

can be tuned in duration and spacing. The water molecules (i.e. hydrogen nucleus) change its location due to the process of diffusion. This movement along the gradient direction has two effects. First, a change occurs in the magnetic field that this nucleus perceives, and second, a phase shift that is proportional to the net displacement also occurs. If we extend these two effects to a population of water molecules, a distribution of phase shifts will be obtained, resulting in a slight attenuation of the MRI signal when compared with hypothetical static water molecules (**Fig. 1**).

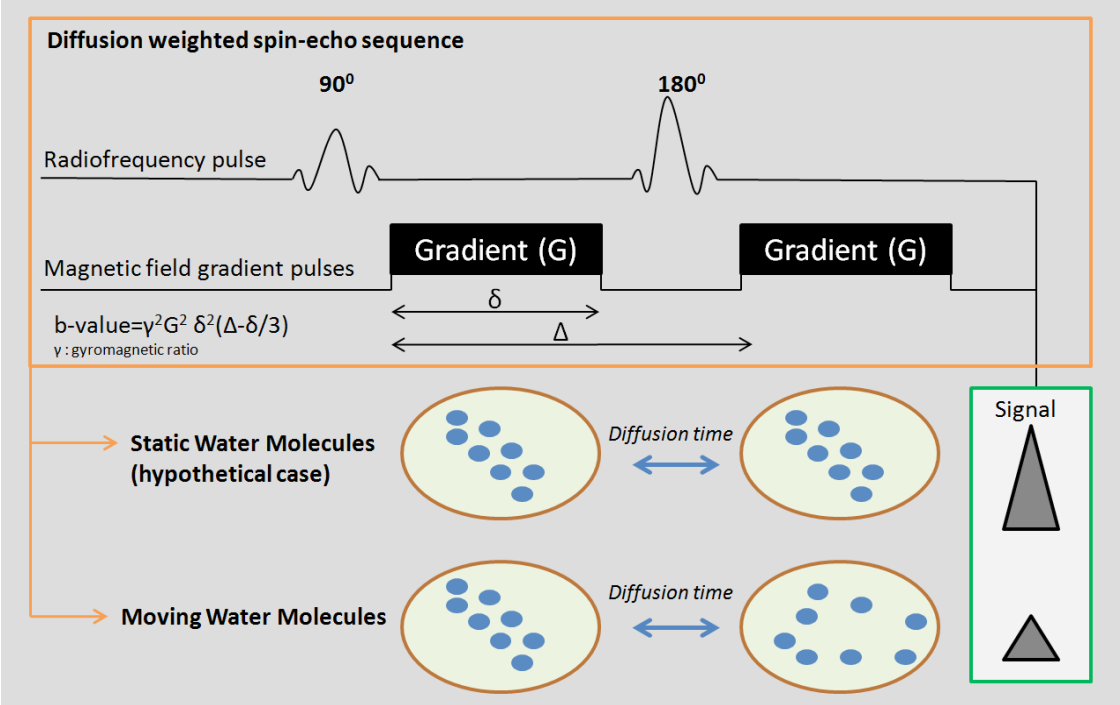

Fig. 1. Schematic diagram showing a T2-weighted spin-echo sequence with two magnetic field gradient pulses of strength G, duration δ, and spacing Δ (diffusion-weighted spin-echo sequence), applied to a group of static and moving water molecules. The moving water molecules are affected showing a loss of signal respect to the static group. Water diffusion is detected as attenuation of measured MR signal intensity.

The signal attenuation is precisely and quantitatively connected to the amplitude of the displacement distribution (2, 42). The tuning of the magnetic field gradient pulses through the b-value, a factor that reflects the strength and timing of the gradients, gener-

ates different degrees of diffusion sensitivity as illustrated in **Fig. 2**. The common pulse sequence in clinical settings for DW-MRI is the Single-shot Spin-echo Echo Planar Imaging (SSEPI) (43).

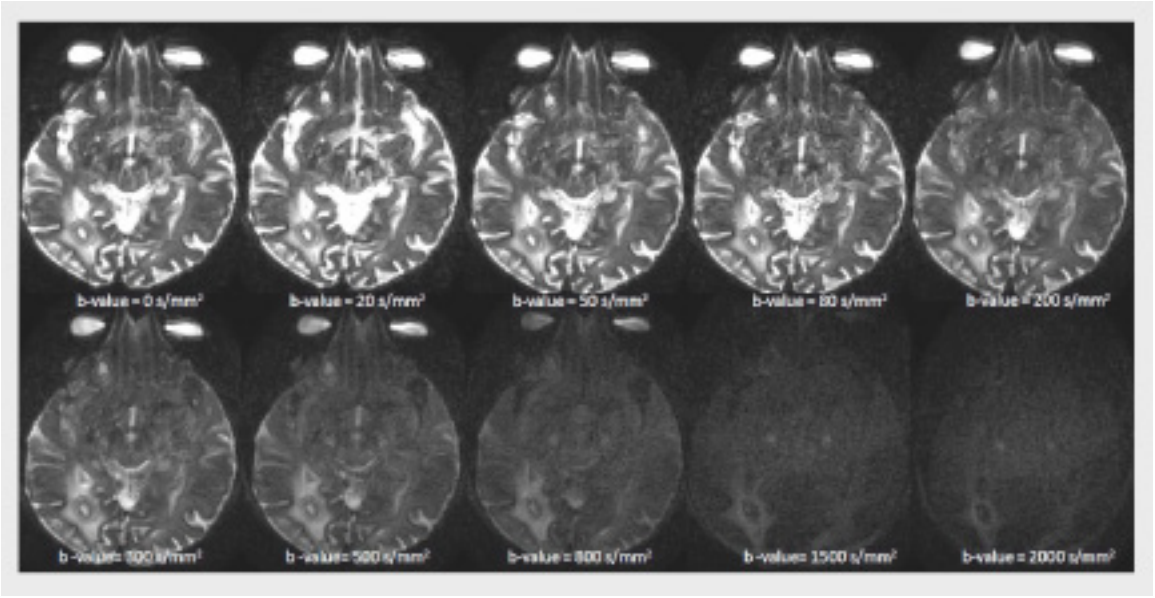

Fig. 2. Diffusion-weighted images of a brain metastasis located in the right occipital region of the brain in a patient. The MR signal is attenuated with the increasing b-values (0, 20, 50, 80, 200, 300, 500, 800, 1500, 2000 s/mm^2).

The attenuation of signal intensities in diffusion-weighted images with different b-values allows for the estimation of the diffusion coefficients in each image location (voxel) through appropriate model fitting (**Fig. 3**).

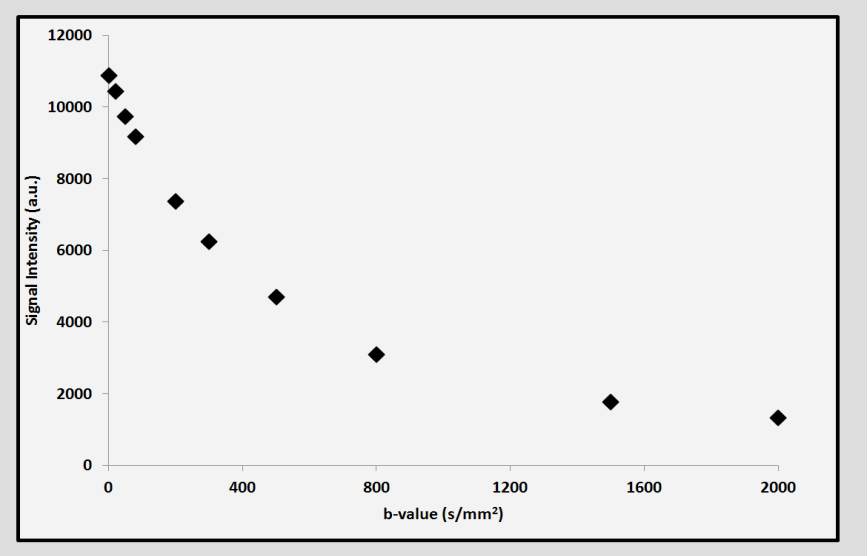

Fig. 3. Diffusion-weighted signal intensity versus b-value in a brain metastasis patient, exhibiting the non-monoexponential decay behavior. The graph illustrates typical in vivo signal attenuation of DW-MRI.

The monoexponential model considers biological tissue as one compartment. The metric that we estimate from this model is the ADC. There are biophysical properties that have an influence on the mobility of water molecules in tissue. Tumors have lower values of ADC than benign tissues because cells in tumors are more tightly packed; in other words, water diffusion is more restricted in tumors because malignant tissues have more chaotic tissue organization and greater cellular density than benign tissues.

An example of the bi-exponential model is the intravoxel incoherent motion (IVIM) introduced by Le Bihan. This model considers biological tissue as two compartments: intra-vascular and extracellular space having the same diffusion and magnetic relaxation properties as depicted in **Fig. 4** (42). IVIM measures the Brownian water molecular diffusion and capillary perfusion and estimates the quantitative imaging metrics: D (i.e., true diffusion coefficient (mm^2/s)), blood perfusion fraction in capillary networks through f (i.e., vascular volume fraction or perfusion factor), and D* which is the pseudo-diffusion coefficient (mm^2/s) associated with blood flow and capillary geometry (42).

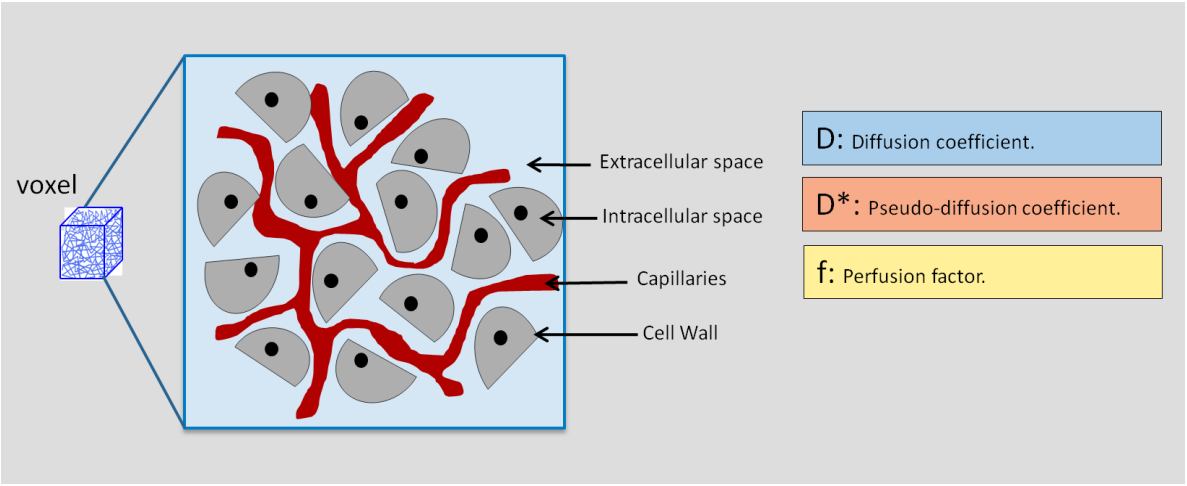

Fig. 4. Schematic diagram depicting different compartments at a voxel level in the tissue. IVIM model consider two compartments extra- and intra-cellular space. The D, D^* and f represent the true diffusion coefficent, pseudo-diffusion coefficent and perfusion factor.

1.2.1.2. **Dynamic contrast-enhanced MRI**

DCE-MRI provides a measurement of tissue perfusion through the acquisition of fast high-temporal T1weighted (w) MR images before, during, and after the administration of a small paramagnetic contrast agent (CA) like gadolinium-diethylenetriamine pentaacetic acid (Gd-DTPA). **Fig. 5** exhibits the standard T1w and T2w images along with DCE-MRI images in a patient with a brain metastasis.

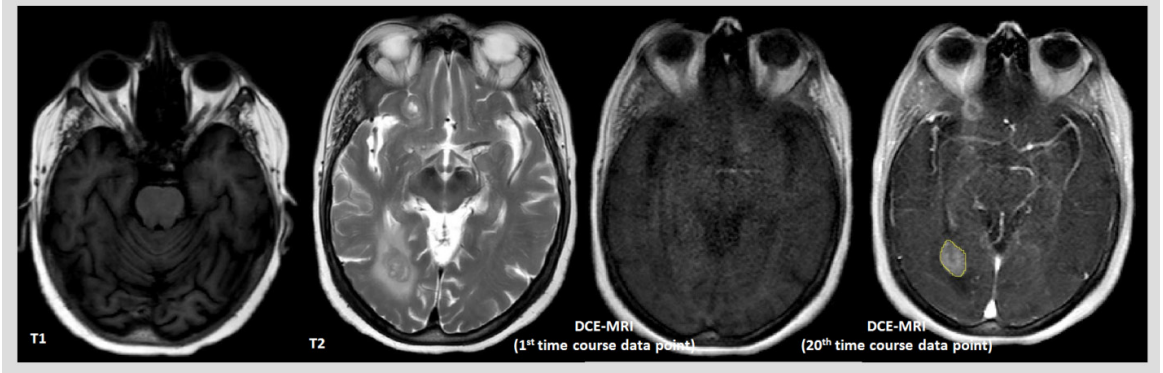

Fig. 5. Representative MRI images of a patient with a brain metastasis: Axial T1w, T2w, DCE-MRI images during 1st and 20th time course data points.

Biological tissue contains intravascular, extracellular or interstitial, and intracellular compartments. Water exchange between erythrocytes and plasma is fast on the MR time scale; thus, the intravascular pool is considered a single compartment. Following intravenous administration, CA leaks through the intravascular compartment to the extracelluar space by passive diffusion in tumors, altering signal intensity of the tissue by changing the relaxation rates of water protons.

The extended standard model (i.e. also called Toft's) (44, 45) , based on the decades old single capillary model (46), utilizes the contrast agent concentration in blood plasma, also called the arterial input function (AIF), to estimate K^{trans} - volume transfer constant between intravascular and extracellular space, v_e - extracellular volume fraction and v_p - plasma volume fraction. The rate constant from extracellular to intravascular space (k_{ep}) is related to K^{trans}/v_e (**Fig.6**).

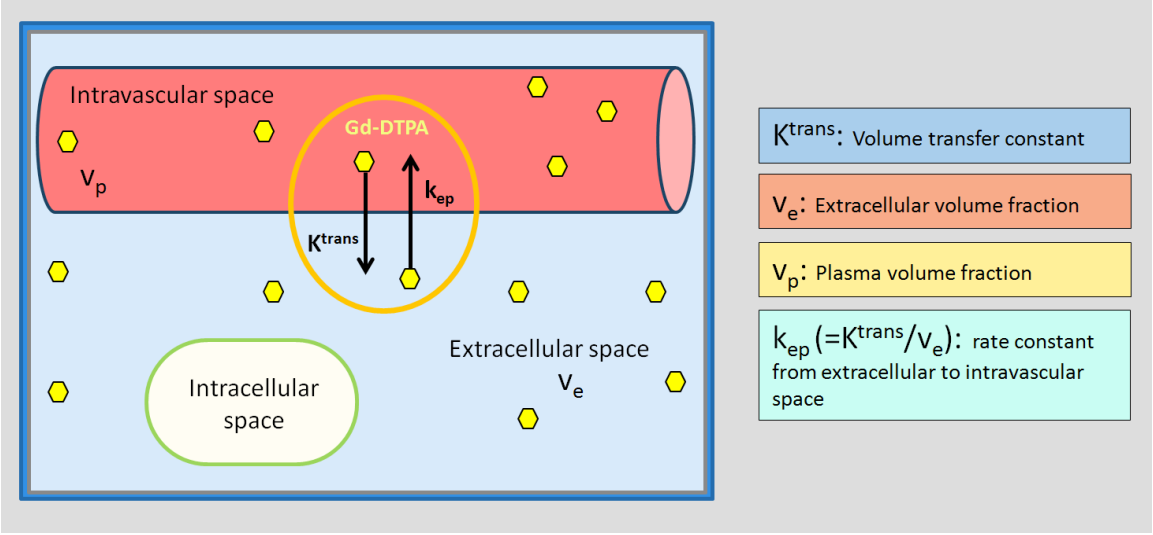

Fig. 6. Schematic illustration of three compartments: intravascular, extra- and intracellular space. K^{trans} is volume transfer constant from intravascular to extracellular space; k_{ep} is the rate constant from extracellular space to intravascular space; v_p and v_e are the volume fraction of plasma and extracellular space, respectively.

A T_1w spoiled gradient recalled echo (SPGR) sequence is commonly used in clinical setting to acquire DCE- MRI data. The DCE-MRI signal-versus-time curves for artery and tumor, obtained from a BM patient are shown in **Fig. 7** and **8.**

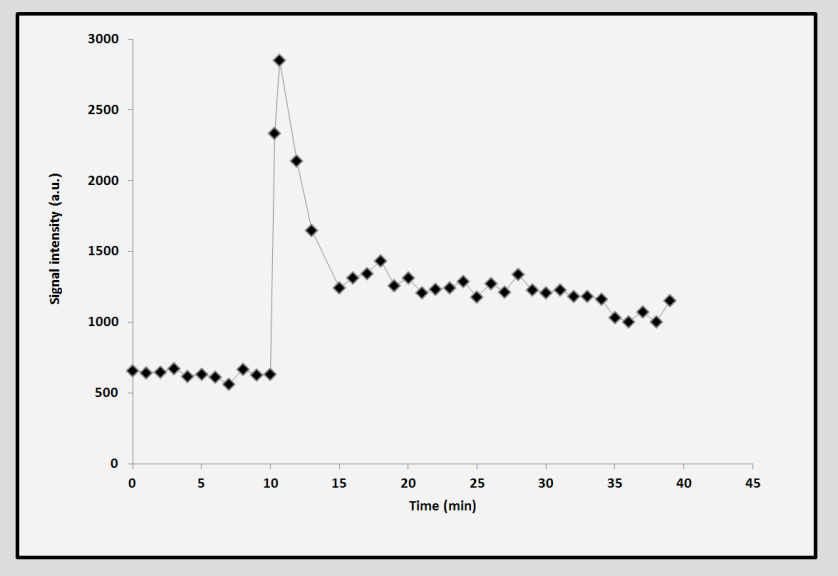

Fig. 7. Signal intensity over time curve extracted from the middle cerebral artery of a BM patient following bolus injection of CA.

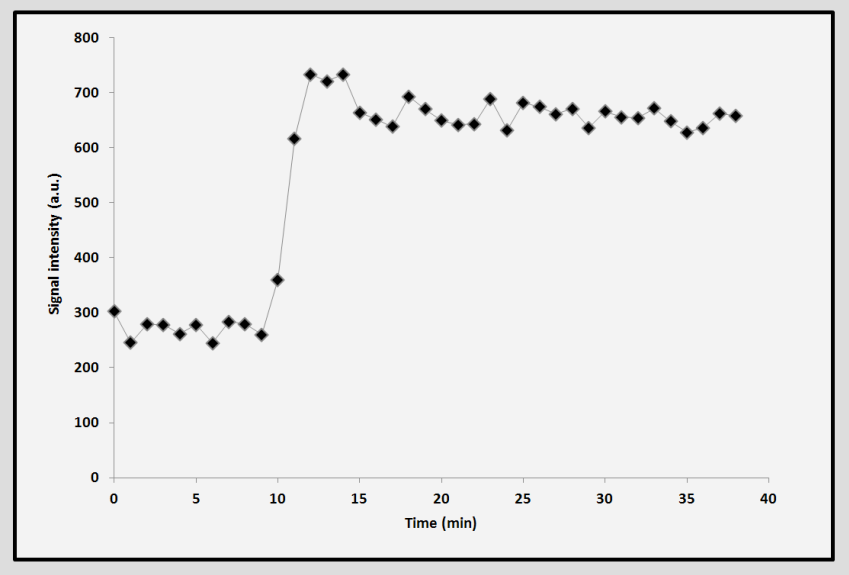

Fig. 8. Signal intensity over time curve extracted from the tumor of a BM patient following bolus injection of CA.

1.2.2. Quantitative PET/CT: Fluorine-18 Fludeoxyglucose

PET imaging technology has been in clinical use for more than 2 decades, with oncology a major focus of its application. This technique has the ability to provide unique information about the molecular and metabolic changes associated with tumors, using molecules labeled with radioactive nuclides such as ^{18}F-FDG (**Fig. 9**) (19). FDG follows the glucose pathway from plasma to tissue, remaining trapped in the tumor cell (19). The positron emitted by ^{18}F at this location annihilates with a nearby electron, creating two simultaneous gamma rays that travel in almost opposite directions through a ring of PET scanner detectors. Following the paths of these two gamma rays, we can determine the approximate location at which the annihilation occurred, thus obtaining a highly sensitive measurement of the distribution uptake of ^{18}F-FDG as illustrated in **Fig. 9** (47). This highly sensitive image generated by PET can lack adequate anatomical information. The use of a combined PET/CT with the precise co-registration of the functional (PET) and anatomical (CT) studies gives extra information to localize the tumor with greater precision, as shown in **Fig. 9** (48). The quantitaive imaging metric, Standard Uptake Value (SUV), is used in ^{18}F-FDG imaging to try to normalize the uptake for administered activity, radioactive decay from time of administration, and patient body mass. SUV is considered an approximate index of ^{18}F-FDG uptake, and can be affected by such factors as the physiological state of the patient, patient body composition, size of the lesion, motion (such as respiratory motion), and region of interest (ROI) selection (49).

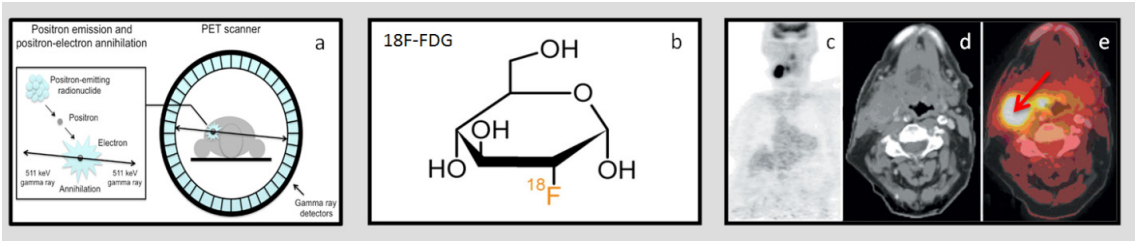

Fig. 9. a. Diagram showing the basic process of the positron emission and annihilation with the subsequent emission of two gamma rays detected by the PET scanner detectors (adapted from (50, 51)). **b.** Structure of ^{18}F-FDG. **c.** Coronal PET image showing the uptake (black spot) of a neck nodal metastasis in HNSCC patient. **d.** Axial CT image of the HNC region. **e.** PET/CT image of a neck nodal metastases (red arrow) showing the uptake of ^{18}F-FDG.

1.2.3. Clinical application of Quantitative Imaging Biomarkers in treatment response assessment and prognosis

DW-MRI, DCE-MRI and ^{18}F-FDG PET/CT have clinical applications ranging from characterization of tumor to prediction of treatment response (40, 49, 52). This thesis will focus on QIBs in treatment response assessment and prognosis estimated from multimodality imaging in HNSCC and BM.

1.2.3.1. **Head and Neck Squamous Cell Carcinoma**

HNC are usually treated with surgery or chemo-radiation therapy (CRT) depending on the extent of the disease (53). DW-MRI estimated ADC constitutes as a biomarker for CRT response in HNSCC. In most cases, high pre-treatment (Tx) ADC values for a tumor reflect a worse response to treatment in comparison to tumors with lower pre-Tx ADC values. The necrotic area inside the tumor could be one possible explanation of this biological behavior (54). Increasing ADC values during or after treatment when compared to pre-Tx values generally reflect that the treatment is successful (2, 11).

A study by Hauser et al. using IVIM DW-MRI indicates that higher f values may predict poor prognosis in HNSCC; additionally they demonstrate a significant increase of all IVIM parameters after CRT (55). Overall, an increase in diffusion related parameters such as ADC and D is correlated with good outcomes. Kim et al. have shown that a significant increase in ADC was observed within 1week of treatment in HNSCC patients who were complete responders (p-value < 0.01) (11). Vandecaveye et al. study further established the utility of ADC in differentiating responding from non-responding HNSCC by providing a threshold (25% and 20% for primary tumors and lymph node metastases, respectively) for the percent relative (Δ) ADC change between pre-Tx and 3 weeks post-Tx (56).

DCE-MRI has shown promise in prognosis of HNSCC. A study by Shukla-Dave et al. suggests that high skewness of K^{trans} was observed in HNSCC patients with poor

prognosis (10). Usually heterogeneous tumors in head and neck region are associated with hypoxia and necrotic areas (57). Chawla et al. found significantly lower K^{trans} in non-responders compared to responders in neck nodal metastases of HNSCC patients (54).

A high SUV value reflects increased glucose uptake in most primary tumors and neck nodal metastases (58). ^{18}F-FDG PET/CT has an established role in HNSCC management including staging and monitoring CRT response (59, 60). Schwartz et al. study showed that primary tumor SUV was a promising prognostic factor in HNSCC patients (61).

1.2.3.2. **Brain Metastases**

In radiation oncology, the use of stereotactic radiosurgery (SRS) for treatment of metastatic intracranial disease has grown in popularity due to its increasing ease of use, the avoidance of cognitive side effects related to whole-brain (WB) RT, and its inclusion as a treatment option in clinical trials (62, 63). The average reported survival of patients with SRS-treated BM is 6–8 months. Within this timeframe, studies have shown SRS to achieve a high radiographic lesional control rate, defined as lesions with stable or decreasing size (64, 65). Lesion control rates are reported to vary by time since treatment, pathology, and lesion size measurements (66, 67). However, no single study has looked at all of these factors during follow-up imaging. In clinical practice, increases in radiographic lesion size post-SRS raises the question of treatment failure versus radiation injury, resulting in difficulties with patient management. This clinical question is more relevant than ever as many patients with BM treated with SRS are living for much longer periods of time with recent advances in systemic therapy. Many studies have reported variable degrees of diagnostic sensitivity and specificity using various MRI sequences and PET imaging techniques, although they have not led to a consensus (68, 69). The existing literature on the assessment of BM with MRI after SRS is sparse and even scarcer for advanced quantitative imaging in this setting (64, 70-73). Furthermore, there are no studies that assess response after SRS within 72 hours or less.

1.3. Advanced Radiation therapy treatments in Cancer

1.3.1. Intensity-modulated radiation therapy

IMRT aims to sculpt radiation dose in such a way that prescribed dose is delivered to the tumor while healthy tissue is spared from unnecessary radiation exposure (74). The procedure manipulates the intensity of each part of a radiation beam for greater precision in tumor irradiation, and allows the use of multiple beams of differing sizes and intensities during treatment. By modulating the intensity of a radiation beam, one or many areas or high intensity radiation and low-intensity areas may exist within a particular field, providing improved control over dose distribution. Furthermore, a radiation beam can be broken up into "beamlets" whose intensity may be individually adjusted. With an expanded range of tools with which to control both the number of fields and the intensity of radiation within a field, dose distribution can be sculpted with increasing precision to conform closely to target volume; IMRT has thus proven capable of "painting" a dose around critical healthy tissues despite complex target and critical structure geometries.

1.3.1.1. **Head and Neck Squamous Cell Carcinoma in Spain**

The Spanish Cancer Registries reported that in 2014, 241,284 new cases of cancer were diagnosed in Spain (75). Out of these, 12,696 were HNC and approximately 90% were SCC (76). Oropharyngeal SCC was the main subgroup for these patients and 52-72% was caused by infection with human papillomavirus (HPV) (77). It has been previously reported that HPV negative (-) HNSCC have poor outcomes compared to HPV positive (HPV+) cancers (78). The mainstay of treatment worldwide for HNSCC remains concurrent CRT and/or surgery (53, 58), with IMRT as an ideal RT technique to minimize side effects and increase local tumor control

1.3.2. Stereotactic Radiosurgery

SRS is a non-invasive, highly precise form of RT that aims to destroy tumor through targeted, high-dose radiation and to achieve local control (62). Because dose delivery is accurate to within one to two millimeters in SRS, the procedure is capable of delivering maximum dose within a target while minimizing the exposure of healthy surrounding tissue to ionizing radiation. To achieve this level of precision, SRS relies on 3-D imaging techniques such as CT, MRI, and PET/CT to determine a tumor's exact size, shape, and location within the patient, immobilization systems to ensure proper patient positioning and fixation throughout the therapy, highly focused gamma-ray or x-ray beams, and IGRT to confirm a tumor's location before and sometimes during treatment. SRS is usually a one-day treatment, but multiple stereotactic treatments may be recommended in certain circumstances, as for tumors larger than 2.5cm in diameter. As a non-invasive procedure, SRS also has implications for patients who are unable to undergo surgery.

1.3.2.1. Brain Metastases in the United States of America

A common neurological complication of cancer, BM affect approximately 20-30% of all cancer patients in the United States (79, 80). These metastases are from primary tumors originating in lung (50 %), breast (15% to 20%) and melanoma (10% to 15%). In some cases (10% to 15%) the primary site of the tumor maybe unknown. Lung cancer and melanoma are frequently associated with multiple metastases while breast and renal cancers are mostly related with single metastasis (81).

The incidence of BM has been on the rise, a trend often attributed to improvements in imaging techniques that allow for earlier detection, as well as to improvements in treatment that have helped prolong the life of many cancer patients. In 2007, 1.5 million patients in USA received a primary diagnosis of cancer, with about 5% of these

primary diagnoses estimated to relapse in the brain (79, 82). BM are an important cause of mortality (83). In terms of treatment options, SRS has emerged as one of the most important for the management of these tumors. BM are also ideal targets for SRS due to characteristics conducive to accurate target delineation, planning, and dose delivery. These tumors are usually largely spherical with a maximum diameter of less than 4 cm, and located in the gray-white junction. Unlike primary gliomas, BM are non-infiltrative, making the highly precise techniques of SRS a viable and effective means of therapy with a high local control rate, defined as lesions with stable or decreasing size (64). Despite these factors, which point to the relevance of BM and its treatment in radiation oncology, prospective studies in RT treatment involving patients with BM are limited.

1.4. Challenges of intensity-modulated radiation therapy and stereotactic radiosurgery in adaptive radiotherapy based on functional imaging

Three major technical challenges in IMRT and SRS persist in the use of functional images for RT: identifying a reproducible, radiotherapy-compatible patient position that is consistent between functional techniques and RT; furthermore, issues related to spatial resolution, geometrical accuracy and standardization and reproducibility also constitute challenges. This thesis addresses the above challenges in RT based on functional imaging.

1.4.1. Patient positioning

In order to ensure precise dose delivery, it is essential for patient positioning to remain the same throughout the treatment simulation and delivery process, which can last several weeks. In Meixoeiro University Hospital of Vigo, Spain, the HNSCC patients were scanned using the same immobilization device as in RT and a flat table for multimodality imaging to reduce issues related to patient positioning.

While the reproducibility of patient position poses fewer inherent difficulties for CT, differences in the practice of patient positioning between MRI and RT presents additional challenges. In treatment planning and delivery that relies on the CT scan or PET/CT scan, for example, the linear accelerator of the treatment room is set up to copy the frame of reference established by laser systems in the CT or PET/CT room. Furthermore, wide-bore CT scanners have made it possible to scan patients in the treatment position, with patients lying on a flat bed design typical of a radiotherapy simulator or treatment couch, allowing for a consistently reproducible patient position from planning through delivery. When MRI is used in RT planning and delivery, however, additional considerations come into play. MRI scanners, which typically place body phased-array coils around the patient and tend to be designed to maximize patient comfort due to the duration of the study, must be adapted to mimic the flat bed design of the RT treatment table and suitable for RT positions. Any immobilization devices that will be used for other imaging devices or for treatment – such as a stereotactic head frame – must be assessed for magnetic safety as well as their ability to fit in the scanner without interfering or disrupting the placement of MR coils. Typical RT practice in patient positioning for different types of cancers must also be considered from the onset, from the use of stereotactic frames (HNC) or wedge-shaped supports (breast cancer) to the placement of the patient in prone or supine position. Solutions to these challenges often compromise image quality because they reduce signal-to-noise ratio (SNR) performance due to the way they interfere with the conductivity of the radiofrequency coils used in MR: for example, the flat bed design of RT is often reproduced in MRI by laying a thin insert on top of the coils, which creates a gap between the patient and the coils that can reduce SNR. Furthermore, the fixation mask used to guarantee reproducible orientation and neck flexion in the treatment of HNC does not fit in most coils used for HN MRI. While the attachment of flexible surface coils to the surface of the mask has been proposed as a possible solution, new methods to incorporate RT masks into systems using multichannel head coils for quality imaging need to be further identified (84, 85).

Given these constraints, it may not be feasible to undertake imaging in a reproducible RT position. Furthermore, anatomical changes often occur in a patient as a response to therapy: normal tissues may deform, and tumor volumes may shrink. With the growing emphasis on the personalization of treatment, a re-contouring of the region of interest (ROI) for re-planning or to measure dose accumulation is often necessary at varying time points, posing new challenges in image registration. In order to ensure the alignment of information obtained from different imaging modalities at the voxel level, it is necessary to use dedicated methods for deformable image registration (DIR) (86, 87). DIR is a relatively new method capable of aligning corresponding points derived from different imaging techniques and constitutes an important tool in image registration for multimodality functional imaging. Yet DIR algorithms have limited availability outside the research setting, and still lack clinical validation.

1.4.2. Spatial resolution and geometrical accuracy

Distortions are an issue in both PET/CT and MRI, and they range from susceptibility artifacts to geometric distortions. This thesis will focus only on evaluating and correcting the distortions related to diffusion acquisition sequences, in an experience at Meixoeiro University Hospital of Vigo, Spain.

Tumor delineation based on MRI relies on good spatial resolution and geometrical accuracy, without which tumors can remain undertreated or healthy tissue exposed to unnecessary radiation. While advances in technology and technique have led to improvements in both areas, fundamental challenges remain. With advances in IMRT, dose delivery has become precise to the order of a millimeter, making accurate tumor delineation an essential factor in treatment planning. The T2w spin echo sequences most often used by MRI for tumor delineation, however, result in slices that are much thicker, at 3 mm or more, which imposes an implicit limit; furthermore, PET/CT has a similar spatial

resolution. In addition, geometrical distortions caused by nonlinearities and eddy currents in gradient coils or inhomogeneities in the main magnetic field (B_0) provide inaccurate spatial information and hinder accurate image correlation. Because the homogeneity of the static magnetic field (B_0) decreases as distance from the center of the magnet bore increases, some of the distortion is a natural property of MR scanners; these system-related distortions can be corrected through lookup tables derived from phantoms. Object- and patient-induced distortions, however, cannot be readily corrected through the use of phantoms. Object-induced distortions include those arising from magnetic susceptibility and chemical shift effects. Distortion resulting from magnetic susceptibility is particularly pronounced at air and tissue transitions, i.e. at the boundaries of structures with different magnetic susceptibilities (88, 89). Chemical shift effects are caused by the differences in resonance frequencies between protons in fat and those in water. While increasingly sophisticated correction techniques continue to be developed for these distortions, the correction of realistic images can be difficult. These distortions can be visualized, however, by using gradient reversals, or by comparing images with opposite readout gradient directions; by mapping the two images acquired through such a procedure, the correction of images of human anatomy may be achieved (90). In DW-MRI, the standard practice of collecting imaged volume through echo planar imaging (EPI) is vulnerable to distortions associated with EPI sequences, which can make correction even more difficult. EPI exhibits strong distortions in the direction along which k-space is traversed slowly, i.e. the phase encode (PE) direction (91, 92). While the size of the PE gradient can be modified by using the bandwidth parameter (as maximizing bandwidth can reduce distortion, which is the case in parallel imaging), distortions can remain large in close proximity to air-tissue boundaries. In HNSCC an alternative to EPI could be half-fourier acquisition single-shot turbo spin-echo (HASTE) which has shown less geometric distortion than EPI (93). Although, a recent study by Schouten et al. suggests that HASTE seems to be inadequate in early response to treatment in HNSCC when is compared to EPI-DWI (94).

Due to the importance of spatial accuracy in radiation oncology treatment planning and delivery, the minimization of geometrical distortions remains a priority. One of the aims of this thesis is therefore dedicated to correcting these geometrical distortions in MRI for the purposes of adaptive RT based on functional imaging for HNSCC patients.

1.4.3. Standardization of imaging protocols and reproducibility of Quantitative Imaging Biomarkers

Standardization of organ-specific imaging protocols is important for DW-MRI, DCE-MRI and ^{18}F-FDG PET/CT. RSNA/QIBA is presently generating DW-MRI, DCE-MRI and ^{18}F-FDG PET/CT profiles which will help in the worldwide translation of these techniques and will be available for public viewing at RSNA website. However, experiments need to be performed to establish the repeatability and reproducibility of the imaging techniques. RSNA/QIBA has defined these terms as follows (36):

Repeatability: Repeatability represents the measurement precision under a set of repeatability conditions of measurement.

Repeatability condition of measurement: The repeatability condition of measurement is derived from a set of conditions that includes the same measurement procedure, same operators, same measuring system, same operating conditions and same physical location, and replicate measurements on the same or similar experimental units over a short period of time

Reproducibility: Reproducibility is measurement precision under reproducibility conditions of measurement.

Reproducibility condition of measurement: The reproducibility condition of measurement is derived from a set of conditions that includes different locations, operators, measuring systems, and replicate measurements on the same or similar objects.

In this thesis, the DW-MRI was used as a test model to perform repeatability and reproducibility experiments using the ice-water phantom constructed by Chenevert et al. (95). This part was initiated at Memorial Sloan-Kettering Cancer Center (MSKCC), USA.

The standardization of ^{18}F-FDG PET data acquisition and analysis continues to be a priority; while recommendations for standardization have been published by various bodies, they have yet to be adopted by or fully implemented in the clinical flow (49, 96).

There is a lack of standard approaches for data collection and analysis in DW-MRI and DCE-MRI to implement them as imaging biomarkers of treatment response in routine clinical practice. This needs to be addressed by performing prospective, large patient population validation studies between multi-centers and multi-vendors. The limits of technology and patient compliance are the main reasons for this lack. Standard methods of assessment should be established and validated against phantoms, with their measurements of reproducibility also being established in multi-center settings. For example, the absence of a standard, repeatable, and consistent methodology for QIBs, the ambiguities that remain in the interpretation of voxel-based data can lead to drastic differences in target volumes for irradiation.

As there is a lack of consensus in the approach to DW-MRI data collection and analysis, it has been difficult to implement the technique extensively worldwide. The lack of standardization, in turn, has made it more challenging for commercial MRI vendors to support DW-MRI, and has limited the use of DW-MRI to sites with sufficient experimental MRI expertise to tackle its complexities.

Technical challenges in acquiring DW-MRI data often make it impractical to perform "ideal" data acquisitions, necessitating compromises in acquisition and/or analysis. Reducing the number of *b*-values for modeling of data, limiting volume of imaging and reducing spatial resolution are some examples.

In addition to the standardization of methods of diffusion assessment, their measurement reproducibility should also be established. In fact, it is necessary to demonstrate the reproducibility of all clinical measurements undertaken at centers, both at the individual and intergroup levels, in order to facilitate study design and to assess the significance of change. By using this information in conjunction with the expected magnitude of therapeutic effect, studies will be able to assess dose-related change.

Reproducibility and repeatability assessments need to be done for organ-specific protocols and sources of error need to be determined and corrected before initiating a clinical trial. DW-MRI clinical trials that assess response to treatment need to include an assessment of measurement variability as a key part of their trial design. The measurement error estimate component needs to be performed on enough study patients or patients representative of those in the study to be statistically relevant. Similar statistical methods should be used across diverse anatomic sites and pathologies to allow for comparative analyses, with a common understanding of the meaning and limitations of statistical measures. There is a common interest in standarize the DW-MRI sequences and the methods to calculate the metrics. Malyarenko et al. reported that standardization of the data acquisition conditions improved the reproducibility of ADC measurements (97). Recently Kolff-Gart et al. in a prospective study with 7 healthy subjects assessed the reproducibility of ADC values with different MRI systems, sequences and anatomical sites in the head and neck region. The study concluded that a small variance in ADC values occurred if the subject is measured on the same MRI system and with the same sequence (98). Assessment of reproducibility and repeatability should be a performed as part of imaging protocols for integration of QIBs in adaptive RT (2).

Chapter II

Chapter II: Motivation, Hypothesis and Objectives

This Ph.D. thesis is divided into three parts; the order of the parts is in accordance with the chronology of the development of this thesis, with the three parts connected in terms of motivation and objectives. The studies in **Part I** and **Part II** were performed at Meixoeiro University Hospital of Vigo, Spain. The study in **Part III** was conducted at Memorial Sloan-Kettering Cancer Center, USA.

2.1. Part I: ARTFIBio project: A novel framework for adaptive radiotherapy based on functional images - *Experience at Meixoeiro University Hospital of Vigo, Spain*

Motivation: In the modern era of adaptive RT, it has become vital to understand how different functional imaging techniques interact and link together in tumors. DW-MRI and ^{18}F FDG PET/CT are two valuable imaging techniques that may help build the framework for future adaptive radiotherapy based on functional imaging. This was the motivation of Part I of the thesis.

Hypothesis: DW-MRI will aid in measuring tumor cellularity while ^{18}F FDG PET/CT will measure the glucose metabolic uptake for both the primary tumors and neck nodal metastases in HNSCC.

Objective: To noninvasively investigate tumor cellularity measured using DW-MRI and glucose metabolism measured by ^{18}F-FDG PET/CT during CRT for human papillomavirus negative (HPV-) head and neck squamous cell carcinoma (HNSCC).

2.2. Part II: Novel application of the reversed gradient Diffusion-Weighted MRI method for tumor response assessment in head and neck cancers (including the novel design of a Phantom Distortion Assessment) - *Experience at Meixoeiro University Hospital of Vigo, Spain*

Motivation: With the onset of precision medicine in oncology, there is an urgent need to assess tumor response during treatment using functional imaging. However, the implement of these functional techniques in routine clinical work flow is one of the most challenging issues in radiation therapy. One constant challenge is to improve image quality and reduce distortion to obtain quality images for radiation treatment planning and delivery. This part of the thesis applied the reversed gradient method in DW-MRI to obtain accurate ADC measurements and minimize geometric distortions in images.

Hypothesis: Reversed gradient method in DW-MRI will help reduce geometric distortions and improve measurement accuracy for quantitative imaging metric ADC.

Objective: This study investigates the use of the reversed gradient method in DW-MRI for reduction in geometric distortion and measurement of accurate ADC, a biomarker of treatment response. Geometric distortion correction will be assessed using mutual information metrics from registration processes used in radiation therapy treatment.

2.3. Part III: Intra Voxel Incoherent Motion Diffusion Weighted MRI and Dynamic Contrast Enhanced MRI methods for tumor response assessment in Brain Metastases – *Experience at Memorial Sloan-Kettering Cancer Center, USA*

Motivation: There are some cancer patients that do not go into remission after treatment. One of the clinical problems lies in the management of patients with BM. SRS is one of the options for these patients to either stabilize the disease or prevent further progression of disease. Hence, in clinical settings it is extremely essential to accurately assess, whether or not a brain metastasis has been successfully treated or whether the metastasis requires additional treatment. This was the motivation for Part III of the thesis. In order to ensure accurate assessments of BM in the clinical scenario, quantitative imaging biomarkers may play a crucial role in deciphering early on treatment efficacy. Hence, a basic prerequisite is having reliable and robust quantitative imaging biomarkers. In the present study, IVIM DW-MRI and DCE-MRI were performed both pre- and post- (1-72 hours) SRS.

Hypothesis: Early changes in perfusion and diffusion derived quantitative imaging metrics will inform the treating physicians at an early time point about which patients will benefit from SRS (or not). For example, metric D (true diffusion coefficient), will increase and metric K^{trans} (volume transfer constant) will decrease with effective SRS treatment.

Objective: To determine whether quantitative imaging metrics derived from IVIM DW- and DCE- MRI can assess early treatment response in patients with BM treated with SRS.

Chapter III

Chapter III: Material & Methods

3.1. Part I: ARTFIBio project: A novel framework for adaptive radiotherapy based on functional images - *Experience at Meixoeiro University Hospital of Vigo, Spain*

3.1.1. Patients

This prospective study was conducted in accordance with the Declaration of Helsinki (99) and the study protocol was approved by the local ethics committee; informed consent was obtained from all patients. All patients eligible for this study had biopsy-proven newly diagnosed HNSCC; and diagnostic biopsies were tested for HPV status. Six HPV- HNSCC patients underwent a total of 34 multimodality imaging (DW-MRI imaging studies at 1.5 T Philips MRI scanner (n=24) pre-, during (2-3 weeks) and post-CRT and ^{18}F-FDG PET/CT pre- and post-CRT (n=10)). All of the patients were treated with IMRT and the prescribed dose varied between 66 Gy and 70 Gy to the local planning target volume (PTV). Patient characteristics are given in **Table 1**.

All patients had a clinical follow-up as the standard of care and survival status was documented into groups at 1 year. The four groups for patients were as follows: no evidence of disease (NED), alive with disease (AWD), dead of disease (DOD) and dead of other causes (DOC). Additionally, locoregional and distant metastases status was noted for all patients (100).

Table 1. Characteristics of the HNSCC patients involved in this study.

Characteristics	Value
Total patients	6
Demographics	
Mean age (yr)	65
Age Range (yr)	52-79
Male/Female	5/1
Location of Primary tumor	
Oropharynx	6
Metastatic loco-regional Nodes	11
Radiation Therapy technique	IMRT
Dose (Gy)	66-70
Fractions	32
Outcome	
Alive with disease (AWD)	3
Dead of Disease (DOD)	2
No evidence of disease (NED)	1

3.1.2. Design of the study

All the patients recruited in this study underwent the workflow designed for the ARTFIBio project as we shown in **Fig. 10.**

A total of 34 multimodality imaging studies were performed (24 MRI and 10 ^{18}F-FDG PET/CT exams) were performed according to the following timeline:

- Pre treatment: MRI study (T1w, T2w, and DW-MRI) and ^{18}F-FDG PET/CT study.
- During treatment: MRI study (T1w, T2w, and DW-MRI) at 2 time points.
    - First time point :10 - 30 Gy [1-2 weeks during treatment]
    - Second time point: 30 Gy – 60 Gy [3-4 weeks during treatment]

- Post treatment: MRI study (T1w, T2w, and DW-MRI) and ^{18}F-FDG PET/CT study.

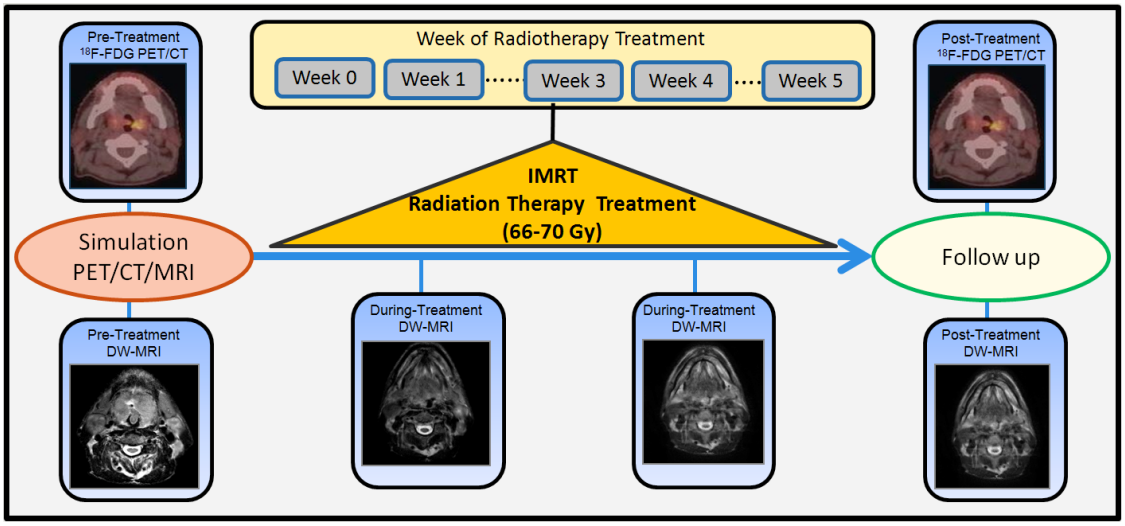

Fig. 10. Workflow representing the ARTFIBio project that was used for all the HNSCC patients at Meixoeiro University Hospital of Vigo, Spain.

3.1.3. Image acquisition protocols

3.1.3.1. Diffusion Weighted MRI

All MRI examinations were performed on a Philips 1.5-Tesla scanner (Achieva; Philips Healthcare, Netherlands) with a Philips Sense Flex coil over the neck at Meixoeiro University Hospital of Vigo, Spain. For MRI, all patients were in supine position and fixed with the immobilization system which was also used during the radiotherapy treatment delivery (**Fig. 11**). A thermoplastic mask, head support and flat table were used to try to minimize the distortion and to improve the registration process between the different imaging modalities. The head support and flat table were adapted to MRI/safety requirements. The MRI protocol consisted of the standard anatomic MRI scans (T1w/T2w images) and DW-MRI.

DW-MRI acquisition was performed using a SS-EPI with 3 b-values (b=0; 600 and 1000 s/mm^2). Other parameters included repetition time (TR) = 5000 ms; echo time (TE) = 77-100 ms, number of excitations (NEX) = 2, field of view (FOV): 25 cm; and slice thickness=6 mm. The total acquisition time for obtaining the DW-MRI data was approximately 5 minutes. The acquisition matrix of 120x97 was zero filled to 256x256 during image reconstruction.

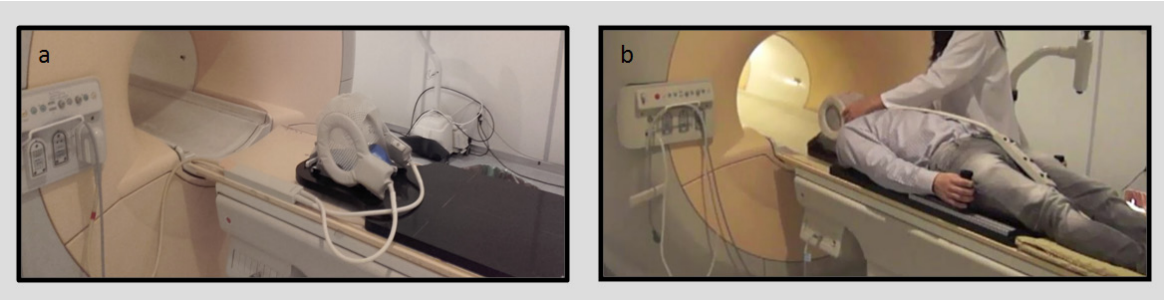

Fig 11. **a.** Flat table with head support adapted to MRI-safety requirements. **b.** Illustrates the patient positioning with the thermoplastic mask over the head support and flat table adapted to MRI-safety requirements.

3.1.3.2. Fluorine-18 Fludeoxyglucose PET/CT

A whole-body PET/CT scan was performed from head to thigh, 60 min after intravenous administration of approximately 370MBq (±10%) of ^{18}F-FDG on a PET/CT scanner (Discovery, GE Healthcare Bio-Sciences Corp, Milwaukee, WI) at Meixoeiro University Hospital of Vigo, Spain. The patient was placed in supine position, with the same immobilization system as in the radiotherapy treatment delivery (**Fig. 12**). Other parameters included a 70 cm axial FOV, a 218 × 218 matrix. Data was acquired in 3D mode. The pixel spacing was 5.47 mm with a slice thickness of 3.27 mm. The spatial resolution to 1 cm varies from 3.99 mm to 4.56 mm. PET images were corrected for attenuation, scatter, decay, dead time, random coincidences, and slice sensitivity.

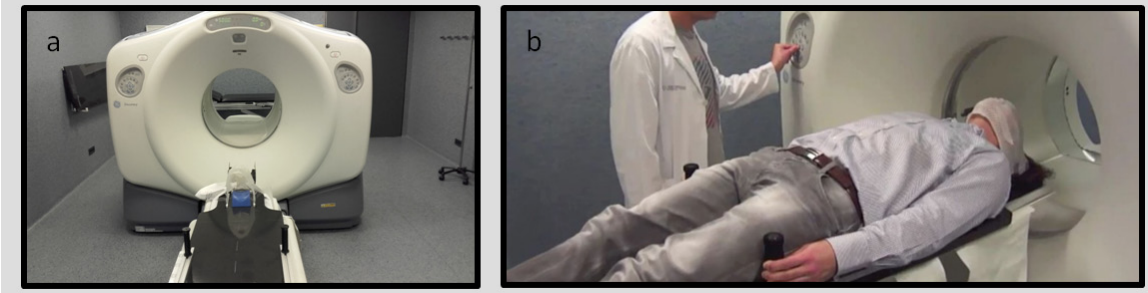

Fig. 12. a. Flat table with head support adapted to PET/CT requirements. **b.** Illustrates the patient positioning with the thermoplastic mask over the head support and flat table at the PET/CT.

Table 2. DW-MRI and Whole body PET/CT scan parameters.

MRI (Philips 1.5T)	DW-MRI	PET/CT (Discovery; GE)	Whole-body PET/CT
Sequence	SS-EPI	**Mode**	3D
TR (ms)	5000	**FOV (cm)**	70
TE (ms)	77-100	**Slice thickness (mm)**	3.27
NEX	2	**Pixel Spacing (mm)**	5.47
FOV (cm)	25 x 25	**^{18}F-FDG**	370 MBq
Slice thickness (mm)	6	**Corrections**	attenuation, scatter, decay, dead time, random coincidences and slice sensitivity
b-values (s/mm^2)	0, 600, 1000		
Acquisition Matrix	120RL x 97AP		

3.1.4. Image analysis

All images were registered and analyzed using in-house software (101). The registration process for DW-MRI and ^{18}F-FDG PET/CT datasets was a two-step process: 1) Manual registration: performing a manual alignment (translation and/or rotation) of the images (DW-MRI; CT-Scan; PET/CT) interactively on screen. 2) Automatic Rigid Registration: Once the images were approximately aligned, a more precise alignment (full rigid transformation) was performed based on an iterative process evaluated by statistical metrics (viola-wells mutual information (102)). Using the Artfibio-tool, the signal intensity values were extracted from the whole tumor volumes (101).

3.1.4.1. Diffusion Weighted MRI

According to Stejskal & Tanner's work (41) and considering the monoexponential approximation (103), the ADC value is calculated using **Eqn.1**:

$$ADC = \frac{\ln\left(\frac{S_0}{S_{b_i}}\right)}{(b_i - b_0)}; i = 1:n \quad \textbf{[1]}$$

Where S_0 is the signal intensity without diffusion weighting, represent the signal intensity with the diffusion weighting factor, b is the b-value (s/mm^2), subindex i represents the different b-values.

ROIs were delineated on the primary tumor and neck nodal metastases by an experienced neuro-radiologist on the DW-MRI image (b=0 s/mm^2). Before contouring the ROIs, the T2w/T1w images were used to determine localization and tumor extent.

Finally, a relative percentage change in estimated imaging metric ADC between pre- and ith intra-Tx week (Wk) was calculated as follows (**Eqn.[2]):**

$$\Delta ADC(\%) = \frac{(ADC_i - ADC_0)}{ADC_0} x\ 100 \quad \textbf{[2]}$$

Where subindex i represents intra-Tx week for ADC metric value and ADC_0 represents the pre-Tx metric value.

3.1.4.2. Fluorine-18 Fludeoxyglucose PET/CT

A radiation oncologist matched the ROIs from the MR images with those of the PET/CT images and analyzed them qualitatively and quantitatively using the attenuation corrected PET emission images. The ROIs were placed over the areas of focal ^{18}F-FDG uptake in both the primary tumor and neck nodal metastases. The intensity of the

^{18}F-FDG uptake in the ROIs was measured using the SUV normalized by the dilution volume (104) as shown in **Eqn.[3]:**

$$SUV = \frac{\text{activity concentration in a voxel or group of voxels}}{\text{activity administered/ body mass}} \qquad \textbf{[3]}$$

The imaging data available in units of μCi/mm per voxel were decay corrected to the time of injection and converted to SUV units (105).

3.1.5. Statistical analysis

In the present study, data was analyzed from a total of 34 multimodality imaging (DW-MRI imaging studies (n=24) pre-, during (2-3 weeks) and post-CRT and ^{18}F-FDG PET/CT pre and post treatment (n=10)) to capture treatment response. Values were presented as mean ± standard deviation. A Spearman correlation analysis was performed between SUV and ADC metric values in the pre-Tx time point, prior to any treatment, allowing analysis of the correlation between to imaging parameters without the potentially confounding effects of treatment. Correlations were reported as in standard guidelines with p-values and correlation, in which an absolute correlation of <0.3 was considered weak, 0.3-0.5 were considered moderate and 0.5-1.0 were considered strong (106). Significance level was set at $p \leq 0.05$. All data analysis was performed using the R software/environment. R is an open source project that is distributed under the GNU General Public License (Copyright 2007 Free Software Foundation, Inc) (107).

3.2. Part II: Novel application of the reversed gradient Diffusion Weighted MRI method for tumor response assessment in head and neck cancers (including the novel design of a Phantom Distortion Assessment). - *Experience at Meixoeiro University Hospital of Vigo, Spain*

3.2.1. Patients

All patients included in the ARTFIBio project have stages T3 or T4 HNSCC. They are treated with IMRT and the prescribed dose to the local planning target volume varies between 66 Gy and 70 Gy. Before and three months after treatment, these studies are performed on these patients: MRI study (T1w, T2w, and DW-MRI) and ^{18}F-FDG PET/CT study (101, 108). Two MRI examinations are conducted during the course of treatment:

- During treatment: MRI study (T1w, T2w, and DW-MRI) at 2 time points.
    - First time point :10 - 30 Gy [1-2 weeks during treatment]
    - Second time point: 30 Gy – 60 Gy [3-4 weeks during treatment]

Three patients from the ARTFIBio project were selected to verify the improvement in Mutual Information; data from one patient of the three were used to verify the improvement in the tumor assessment using the reversed gradient method.

3.2.2. Image acquisition protocols

All MRI examinations were performed on a Philips 1.5-T scanner (Achieva; Philips Healthcare; Netherlands) at Meixoeiro University Hospital of Vigo, Spain with the patient in supine position and with the same immobilization system as in treatment delivery (thermoplastic mask, head support), but adapted to MRI requirements. DW-MRI

with b=0, 600 and 1000 s/mm² were obtained with these parameters: TE/TR (ms) = 77-100/5000; FOV (cm): 25X25; Matrix Size: 120x97 and slice thickness of 6 mm. A Flex-L coil (Philips Sense Flex Medium) was placed over the neck and over the phantom-DA. A second set of DW-MRI data with the reversed direction of the phase was acquired by switching the 'fat-shift direction' in the Philips user interface. The radiotherapy immobilization system contributed to the reduction of moving artifacts. After image acquisition, an ADC map was calculated using the standard software on the imaging console (Achieva; Philips Healthcare).

Table 3. DW-MRI scan parameters.

MRI (Philips 1.5T)	DW-MRI
Sequence	SS-EPI
TR (ms)	5000
TE (ms)	77-100
NEX	2
FOV (cm)	25 x 25
Slice thickness (mm)	6
b-values (s/mm^2)	0, 600, 1000
Acquisition Matrix	120RL x 97AP

3.2.3. Reversed Gradient Diffusion Weighted MRI Method for tumor response assessment in head and neck cancers

It has been shown that in general the addition of a spatially-varying static magnetic field inhomogeneity [$B(x,y,z)$] causes spatial distortion along the r_{th} axis (109). The r_{th} axis is the direction in which the strength of the effective magnetic field gradient that allows phase encoding is applied, and r_{th} can be the x, y, or z axis. Spatial distortion in single slice EPI acquisitions may therefore be considered to occur only during the phase encoding direction. In this study, the x, y, and z axes are chosen to correspond to the frequency encoding, phase encoding, and slice-selective axes, respectively. The reversed

gradient correction method uses a second acquisition performed under exactly the same conditions, supposing that the spatial shifting of the signal will occur in the opposite direction along the *y*-axis (91). The spatially shifted signal from *y* appears in the first image at (the frequency encoding gradient is denoted by G_y):

$$y_1 = y + \frac{B(x,y,z)}{|G_y|} \qquad \textbf{[4]}$$

The spatially shifted signal from *y* appears in the second image at:

$$y_2 = y - \frac{B(x,y,z)}{|G_y|} \qquad \textbf{[5]}$$

Then the corrected coordinate can be calculated combining **Eqns.[4]** and **[5]**:

$$y = \frac{y_1 + y_2}{2} \qquad \textbf{[6]}$$

The corresponding pairs of *y*-values in the distorted MRI need to be located (92). Corresponding pairs can be found by performing line integrals of pixel intensity in distorted MR images, i_1 and i_2, along each frequency encoding line. Corresponding values of y_1 and y_2 are identified as those that equalize the two integrals. However, correcting the spatial distortion alone does not yield a correct image, *i*. The Jacobian of the coordinates transforms from distorted to undistorted space and is used to compensate for the effect of the transform on the pixel intensity. This method is extensively explained in Morgan et al. (92).

We corrected all distorted datasets (DW-MRI, b = 0, 600 and 1000 s /mm^2) with the SPM8 software selecting the HySCO options to apply the reversed gradient method. The software can be freely downloaded from a webpage, where extensive documentation is available (110, 111). The standard settings of the method were used: dimension of phase encoding *y (Antero-Posterior Direction)*, Maximal data resolution *full*; Smoothing of Spline-Interpolation *0.1*, Weight for "diffusion" regularizer *50*; Weight for "Jaco-

bian" regularizer *10*. (110, 112). The movement associated with the increase of the scan time was reduced by the use of the immobilization systems also used in RT, during the acquisition.

The software exported the images in the nii format, which were converted to the Digital Imaging and Communications in Medicine (DICOM) format with an in-house tool, based on the Insight Segmentation and Registration Toolkit (ITK) libraries.

3.2.4. Novel Design of Phantom-Distortion Assessment

A phantom called distortion assessment (DA) was developed for this study (**Fig. 13**), specifically designed to assess the distortion in DW-MRI. It consists of a 17 x 17 x 17 cm^3 polyethylene HD 500 (PE-HD500) cube, which contains 10 rows by 5 columns of empty cylindrical hollows (diameter: 14 mm) in two sides. The design was built by SIHO Ltd (Vigo, Spain). Different cylindrical hollows of the phantom-DA were filled with water and were kept in the MRI room for 24 hours in order to reach room temperature. Before the study, the water temperature was measured. An MRI (T2w Turbo Spin Echo and DW-MRI) was performed on this phantom-DA to evaluate distortion.

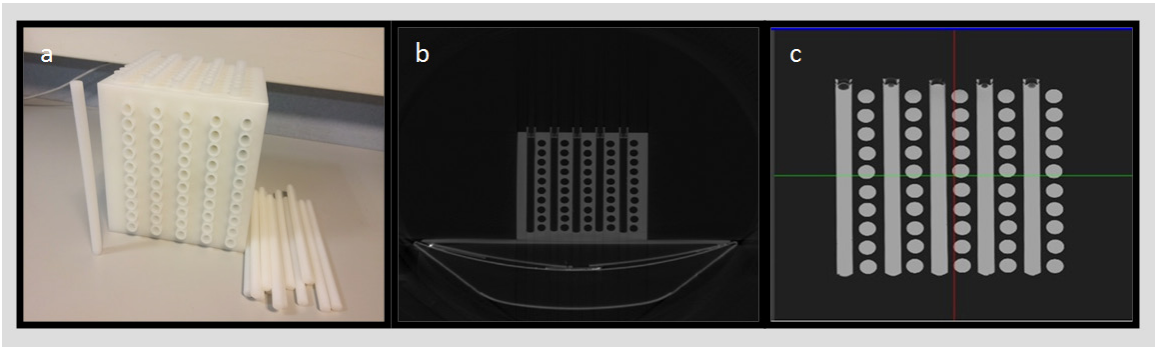

Fig. 13. a. Phantom-DA, specifically designed for distortion assessment. **b.** CT Axial image of empty Phantom-DA, **c**. T2w MRI Axial image of Phantom-DA, Cylindrical hollows are filled with water.

3.2.5. ARTFIBio software and calculations of mutual information

All datasets (CT-Scan, MRI studies, dose distribution) were registered using in-house software ARTFIBio 0.6.2, in order to extract each voxel 's information. This software includes a specific tool to calculate mutual information of two different sets of images. For the datasets from the same MRI study, no registration is needed, and only mutual information is calculated. The value of this metric was used to evaluate the grade of improvement in image distortion with and without the reversed gradient method; no additional non-rigid registration process was considered as the purpose of this study was primarily to evaluate the reversed gradient method.

The simulation CT study was registered with the DW-MRI to associate the dose to each voxel. The registration process of the two datasets consisted of a two-step process: 1) Manual registration: making a rough manual alignment (translation and/or rotation) of the images (DW-MRI; CT-Scan; PET/CT) interactively on screen; 2) Automatic Rigid Registration: Once the images were approximately aligned, a more precise alignment (full rigid transformation) was performed based on an iterative process evaluated by statistical metrics (Mattes mutual information cost metric (102).

3.2.6. ADC calculations and tumor response evaluation

ADC was recalculated from undistorted images corrected by the reversed gradient method, and then the ADC variation during treatment was compared with delivered dose for corrected and raw images. The ADC was also recalculated from raw images to avoid discrepancies due to different ADC calculation methods.

According to Stejskal & Tanner's work and considering the monoexponential approximation, the signal is attenuated according to (41, 103):

$$S_1 = S_0 \cdot e^{-b \cdot ADC} \qquad [7]$$

Where S_1 is the signal value of the images at b-value, b-value varies between 0, 600 and 1000 s / mm^2, and fitting the data to this equation, we can obtain the ADC values.

For the patient, the signal intensity (SI) values were extracted from DW-MRI of the whole tumor volume using ARTFIBio-tool (101). The registration process described above was done with diffusion MRI for three different b-values. For the phantom-DA, different ROIs were drawn in the water cylindrical hollows of the phantom-DA, using the tool ImageJ (113). The signal intensity (SI) values of the different ROI's were extracted. The monoexponential approximation was used to fit the SI of the three b-values in order to obtain the corresponding ADC metric (103). In addition, the ADC value of water from raw images and corrected images was compared.

3.3. Part III: Intra Voxel Incoherent Motion Diffusion Weighted MRI and Dynamic Contrast Enhanced MRI methods for tumor response assessment in Brain Metastases – *Experience at Memorial Sloan-Kettering Cancer Center, USA*

3.3.1. Diffusion Weighted MRI Ice-Water Phantom

The ice-water phantom designed by Chenevert et al. consists of a 50 ml polypropylene tube and 1000 ml polypropylene wide mouth jar (95). The 50 ml tube is filled with distilled water, capped and fixed to the bottom of the 1000 ml jar. In this DW-MRI study, a jar was filled with cubed ice and water and the phantom was cooled for approximately 30 min prior to the scanning. After the initial cool-down period, more cubed ice was added to replace the melted ice.

The MRI series was performed on a Philips 3-Tesla MRI scanner (Ingenia; Philips Healthcare, Netherlands) and on a General Electric 3-Tesla MRI scanner (General Electric, Milwaukee, WI) at MSKCC with the phantom positioned in the head array coil

with the measurement tube axis along superior-inferior direction. DW-MRI with b=0, 500, 800, 1000 and 2000 s/mm^2 were obtained with these parameters: TE/TR (ms) = 77/8000; FOV (cm): 24x24; Acquisition Matrix Size: 128x128 and slice thickness of 5 mm. A total of 4 DW-MRI were performed to study repeatability in immediate succession under controlled settings (**Table 4**).

Table 4. DWI Icewater Phantom scan parameters.

MRI (GE 3T; Philips 3T)	DW-MRI
Sequence	SS-EPI
TR (ms)	8000
TE (ms)	77
NEX	2
FOV (cm)	24 x 24
Slice thickness (mm)	5
b-values (s/mm^2)	0, 500, 800, 1000, 2000
Acquisition Matrix	128RL x 128AP
Reconstruction Matrix	256 x 256

3.3.2. Design of the study

All the patients involved in this study underwent the workflow shown in **Fig. 14.** MRI exams were performed with the following timeline. Pre-treatment: MRI study (T1w, T2w, IVIM DW-MRI and DCE-MRI). Early post-treatment (within 1-72 hours): MRI study (T1w, T2w, IVIM DW-MRI and DCE-MRI). In addition, follow up MRI (with DW-MRI) at 2, 6 and 12 months was performed as part of standard clinical care at MSKCC.

Fig. 14. Workflow representing the study design for all BM patients at MSKCC.

3.3.3. Patients

This prospective imaging study was approved by the Memorial Sloan-Kettering Cancer Center (MSKCC) institutional review board for patients with BM treated with SRS. The subject inclusion eligibility criteria required adults aged 18 and over, who are clinically stable and who do not require oxygen or cardiovascular monitoring, whose weight does not exceed 125 kg and who had metastatic brain tumors from any pathology greater than or equal to 1.0 cm that will be treated with SRS. After giving informed consent, 14 patients were enrolled in this prospective MRI study. Of these, 11 patients underwent SRS and 3 were not treated ultimately treated. Of these 11, 9 completed pre- and early post-Tx MRI and 2 did not get the early post-Tx MRI. Thus, the final study population included 9 patients (5 males and 4 females), with a mean age (mean ± SD) of 61 ± 12 years old. The locations of primary tumors in patients were lung (4 patients), melanoma (2 patients), prostate (1 patient), rectum (1 patient) and HNSCC (1 patient). Patient characteristics are given in **Table. 5**. For these 9 patients, the early post-Tx MRI was performed between 2 to 24 hours, keeping in accordance with the study design which needed early post-Tx to be within 1-72 hours.

The clinical follow-up was classified as NED, AWD, DOD and DOC (100). Loco-regional and distant metastases control was assessed at approximately 3 months after completion of treatment. All patients had a clinical follow-up between 3-12 months.

Table 5. Characteristics of the patients involved in this study.

Characteristics	Value
Total patients	9
Demographics	
Mean age (yr)	61
Age Range (yr)	47-80
Male/Female	5/4
Location of Primary tumor	
Lung	4
Melanoma	2
Prostate	1
Rectum	1
HNSCC	1
Radiation Therapy technique	SRS
Dose (Gy)	18-21
Fractions	1
Outcome	
Alive with disease (AWD)	7
Dead of Disease (DOD)	1
No evidence of disease (NED)	0
Dead due to Other Cause (DOC)	1

3.3.4. Image acquisition protocols

A total of 18 MRI exams were performed on 9 BM patients who were treated with SRS. MRI examinations were performed on a Philips 3T MRI scanner (Ingenia; Philips Healthcare, Netherlands) using a neurovascular phased-array coil at MSKCC. The standard MR acquisition parameters were as follows: multiplanar (axial, coronal, and sagittal) T2-weighted ($T2_W$), fat-suppressed, fast spin-echo images TR= 4000 ms; TE = 80 ms; number of averages (NEX) = 2; matrix = 256 × 256; slice thickness= 5 mm, FOV= 20-24 cm and multiplanar T1w images (TR=600 ms; TE= 8 ms; NEX= 2; slice thickness= 5.0 mm; matrix= 256 × 256, FOV = 20-24 cm. Standard T1w and T2w imaging was followed by DW-MRI.

3.3.4.1. Intra Voxel Incoherent Motion Diffusion Weighted MRI

The IVIM DW-MRI data was acquired using a SSEPI sequence with 10 b-values (i.e., b=0, 20, 50, 80, 200, 300, 500, 800, 1500, 2000 s/mm^2). Other MR parameters were as follows: TR = 4000 ms, TE = 98-104 ms, NEX = 2, matrix = 128 × 128, FOV = 24 cm, slices = 8-10, slice thickness = 5 mm.

3.3.4.2. Dynamic Contrast Enhanced MRI

A 3D-SPGR pulse sequence with 3 flip angles (FA=30°, 15°, 5°) was used for native T1 mapping, followed by dynamic imaging with contrast agent administration (FA=30°, TR = 4.6 ms, TE = 2.4 ms, phases = 40-60, NEX = 1, FOV: 24 cm, slice thickness =5 mm. The contrast agent Gd-DTPA was delivered by antecubital vein catheters at a bolus of 0.1mmol/kg and 2 cc/s, followed by saline flush.

Table 6. IVIM DW-MRI and DCE-MRI scan parameters.

MRI (Philips 3T)	IVIM DW-MRI	DW-MRI	DCE-MRI*
Sequence	SS-EPI	SS-EPI	3D-SPGR
TR (ms)	4000		4.6
TE (ms)	98-104		2.4
NEX	2		1
FOV (cm)	24		24
Slice thickness (mm)	5		5
b-values (s/mm^2)	0, 20, 50, 80, 200, 300, 500, 800, 1500, 2000	0, 1000	
Phases			40-60
Flip Angle (deg)			30
*Pulse sequence 3D-SPGR with 3 flip angles (FA=30°, 15°, 5°) was used for native T1 mapping. The contrast agent Gd-DTPA was delivered by antecubital vein catheters at a bolus of 0.1 mmol/kg and 2 cc/s.			

3.3.5. Image Analysis

3.3.5.1. Multi b-value Diffusion Weighted MRI Image Analysis

ROIs were delineated on the BM by an experienced neuro-radiologists on the DW-MRI image (b=0 s/mm^2). Before contouring the ROIs, the T2w/T1w images were used to determine localization and tumor extent.

The multi b-values DW-MR data were fitted to the models detailed below:

Monoexponential model was used to calculate composite ADC with all the b-values using **Eqn. [7]** (39),

The bi-exponential IVIM model (42) (**Eqn. [8]**) is:

$$S = S_0[fe^{(-bD^*)} + (1 - f)e^{(-bD)}] \quad \textbf{[8]}$$

where S_0 is the signal intensity without diffusion weighting, S represent the signal intensity with the diffusion weighting factor, b is the gradient factor (s/mm^2), f is the microvascular perfusion volume fraction, D is the true diffusion coefficient (mm^2/s), and D^* is the pseudo-diffusion coefficient (mm^2/s).

The metrics derived from IVIM DW-MRI were estimated using a nonlinear least-square curve fitting method as detailed by Lu et al. (114, 115). A noise floor rectification scheme was optimized to generate IVIM metrics on a voxel-by-voxel basis (115). **Fig. 15** shows the IVIM fitting for the IVIM DW-MRI data acquired with multi b-value. All post-processing analyses were performed using in-house scripts written in MATLAB (Mathworks, Natick, USA).

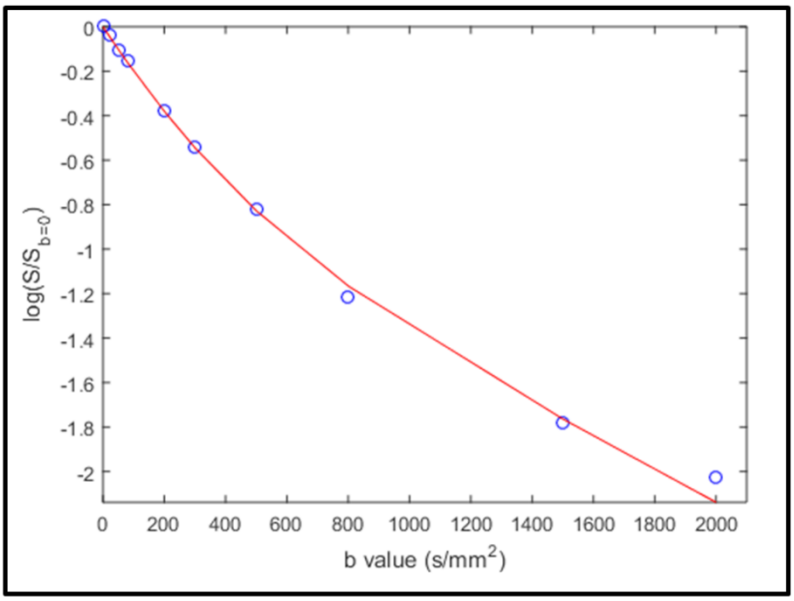

Fig. 15. Logarithm of the MR signal intensity decay averaged over all voxels within the brain metastasis of a patient as a function of the b-value. The blue circles represent the experimental data, and the solid red line is the IVIM model fit.

Finally, a relative percentage change (Δ) in IVIM estimated imaging metrics (ADC, D, f) between pre- and early post-Tx was calculated as follows:

$$\Delta X(\%) = \frac{(X_p - X_0)}{X_0} x\ 100 \quad \textbf{[9]}$$

Where X_0 represents the pre-Tx metric value and X_p represents early post-Tx metric value.

3.3.5.2. Dynamic Contrast Enhanced MRI image analysis

Quantitative DCE-MRI analysis of the tumor tissue time course data was performed using the two-compartment Tofts model. The observable spoiled gradient echo signal with CR bolus injection is given by:

$$S(t) = S_0 \frac{\left(1-e^{-R_1(t)}\right)}{\left(1-\cos(\theta)\, e^{-R_1(t)}\right)} e^{-R_2^* TE} \sin(\theta) \qquad \textbf{[10]}$$

where $S(t)$ is the signal intensity at time t, θ is the flip angle, R_1 (t) ($R_1=1/T_1$) is the time course of longitudinal relaxation rate in the voxel, R_2^* ($R_2^*=1/T^*_2$) is the transverse relaxation rate, TR is the repetition time, TE is the echo time, S_0 is a constant associated with the scanner gain and proton density.

The observable R_1 derived from **Eqn. [10]** is given by:

$$R_1(t) = -\frac{1}{TR}\left(\frac{1-\frac{S(t)}{S_0 \sin(\theta)\, e^{-R_2^* TE}}}{1-\frac{S(t)\cos(\theta)}{S_0 \sin(\theta)\, e^{-R_2^* TE}}}\right) \qquad \textbf{[11]}$$

The water protons relaxation rate R_1 ($=1/T_1$) in intravascular space can be expressed as (116):

$$R_{1p} = R_{10p} + \mathcal{R}_p\,(1 - Hct)\, C_p \qquad \textbf{[12]}$$

where R_{10p} is the precontrast blood plasmal relaxation rate constant, C_p is the blood plasma CA concentration (i.e., called AIF) , is the blood plasma CA longitudinal relaxivity and is the mean value of Hematocrit of the microvasculature which is about 0.45 in large vessels (117).

The tissue water protons relaxation rate constant R_1 and tissue concentration, C_t, are related as (45);

$$R_1 = R_{10} + \mathcal{R}\, C_t \qquad \textbf{[13]}$$

Where R_{10} is the precontrast tissue water protons relaxation rate constant and $\Re$ is the CA longitudinal relaxivity, C_t is the total tissue concentration which is the amount of CA distributed in the intravascular space and extracellular space:

$$C_t = K^{trans} \int_0^t e^{-k_{ep}} C_p(\tau)\, d\tau + C_p\, v_p \qquad \textbf{[14]}$$

The **Eqn. [13]** can be re-written as:

$$R_1(t) = R_{10} + \mathcal{R} \times K^{trans} \int_0^t C_p(\tau)\, e^{-k_{ep}} d\tau + C_p\, v_p \qquad \textbf{[15]}$$

where K^{trans} - volume transfer constant, kep ($=K^{trans}/v_e$): rate constant from extracellular to intravascular space (extra- to blood), C_p - plasma concentration of CA, v_p - plasma volume fraction and v_e is the extracellular volume fraction.

ROIs were delineated on the BM by an experienced neuro-radiologist on the pre- uptake DCE-MRI image. Before contouring the ROIs, the T2w/T1w images were used to determine localization and tumor extent. A simplified two compartment standard model (SM) was used to estimate the following metrics: K^{trans} (volume transfer constant), v_e (extracellular volume fraction), v_p (plasma volume fraction). Using in-house scripts written in MATLAB (Mathworks, Natick, USA) we fitted the DCE-MRI data extracted from ROIs to the **Eqn. [15]. Fig. 16.** represents a typical DCE-MRI data fitted as explained above. A population-based AIF extracted, as reported previously, was used (118). **Fig. 17** shows the population-based AIF.

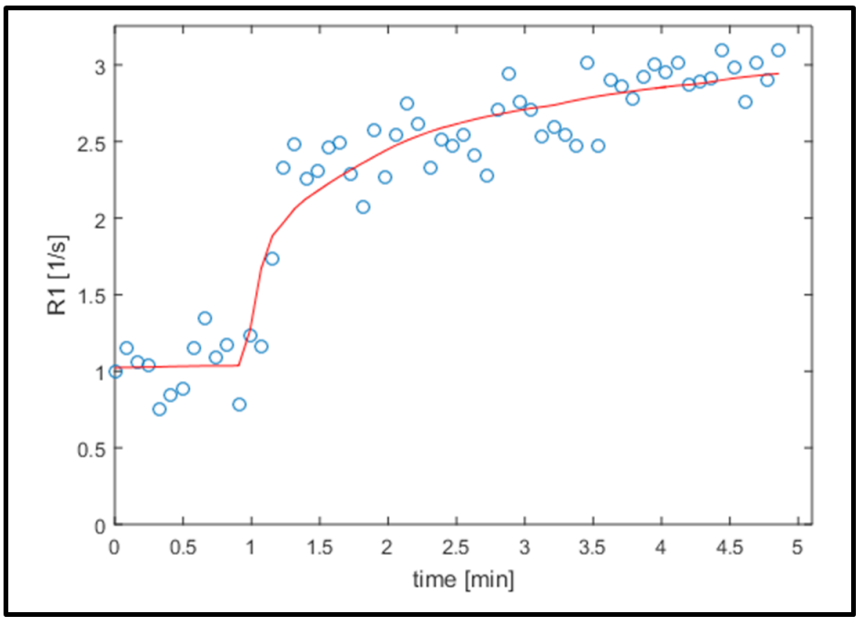

Fig. 16. R1 time course including SM fit following a bolus injection of contrast agent. The SM shows a good fit to the dynamic data.

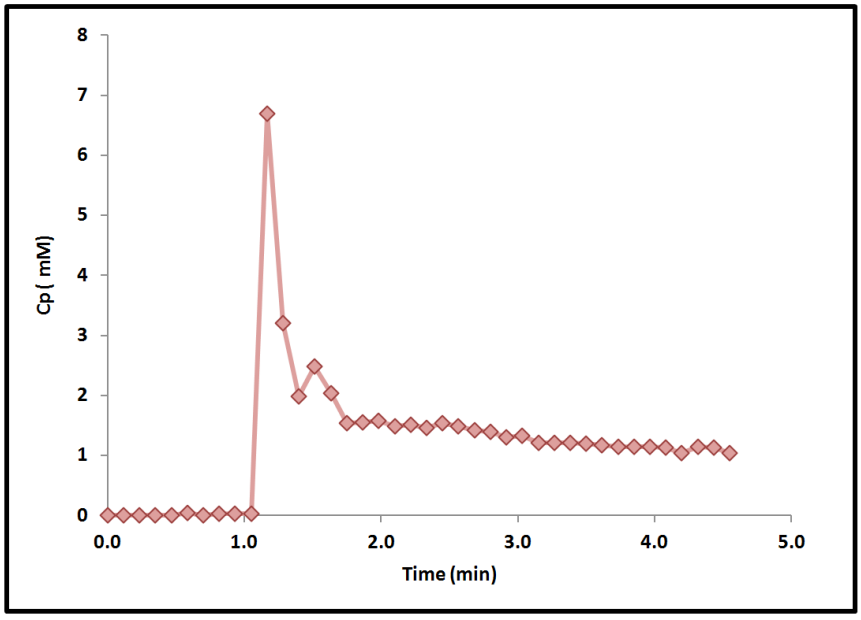

Fig. 17. Contrast concentration over time in the middle cerebral artery following bolus injection of contrast agent.

Finally, a relative percentage change in DCE-MRI estimated imaging metrics (K^{trans}, v_e, v_p) between pre- and early post-Tx was calculated as follows:

$$\Delta Y(\%) = \frac{(Y_p - Y_0)}{Y_0} x\ 100 \quad \textbf{[16]}$$

Where Y_0 represents the pre-Tx metric value and Y_p represents early post-Tx metric value.

3.3.5.3. Tumor volume calculation

For each patient, the total tumor volume was calculated as the product of the area of the ROI and the slice thickness based on T2w images using image-J software (113).

$$V\ (cm^3) = ROI_{AREA}(cm^2)\, x\ Slice\ Thickness(cm) \quad \textbf{[17]}$$

3.3.6. Statistical analysis

3.3.6.1. Diffusion Weighted MRI Ice-Water Phantom Study

Two MR scanners from different vendors but with the same field strength (3T) were analyzed. To assess the differences in ADC values between the 4 measurements (passes) performed within, across vendors and between different ROIs drawn, a Student's t-test was used. Significance level was set at $p \leq 0.05$. The within-subject coefficient of variation was calculated for the repeatability measurements as recommended by Raunig et al. (119). A one-sample t-test was performed to determine differences of ADC values from the literature value of 1.1 x 10^{-3} mm^2/s at 0°C (120).

3.3.6.2. Brain Metastases Patients Study

In the present study, the pre-Tx and early post-Tx ADC, D, D*, f, K^{trans}, v_e, v_p and total tumor volumes were used for data analysis estimated from 18 MRI examinations performed on 9 BM patients to capture early treatment related changes. A Student's t-test was used to compare the parametric differences related to early treatment changes and a Pearson correlation analysis was performed to report the correlation and p-value of all the metrics mentioned above in the pre-Tx time point, prior to any treatment, allowing analysis of the correlation between to imaging parameters without the potential confounding effects of treatment (121). Correlations were reported, under the same standard guidelines of Chapter I. Absolute correlation of <0.3 was considered weak, 0.3-0.5 were considered moderate and 0.5-1.0 were considered strong. Significance level was set at $p \leq 0.05$ (106). All data analysis was performed using the R software/environment. R is an open source project that is distributed under the GNU General Public License (Copyright 2007 Free Software Foundation, Inc) (107).

Chapter IV

Chapter IV: Results

4.1. Part I: ARTFIBio project: A novel framework for adaptive radiotherapy based on functional images - *Experience at Meixoeiro University Hospital of Vigo, Spain*

All 6 patients were untreated at the first time point of multimodality imaging and had biopsy-proven SCC, and were HPV-. Among the 6 patients, a total of 11 neck nodal metastases and 5 primary tumors were analyzed (3 patients had more than one node and 1 patient had an unknown primary tumor site). Patients were grouped as follows based on clinical outcome: NED=1, AWD=3, and DOD=2 (**Table 1**). A total of 34 multimodality imaging data (DW-MRI imaging studies (n=24) and ^{18}F-FDG PET/CT (n=10)) were analyzed to capture CRT response. There was a significant strong negative correlation (ρ=-0.67, p=0.01) between pre-Tx mean SUV and pre-Tx mean ADC for the 11 lymph nodes and 5 primary tumors (**Fig. 18**).

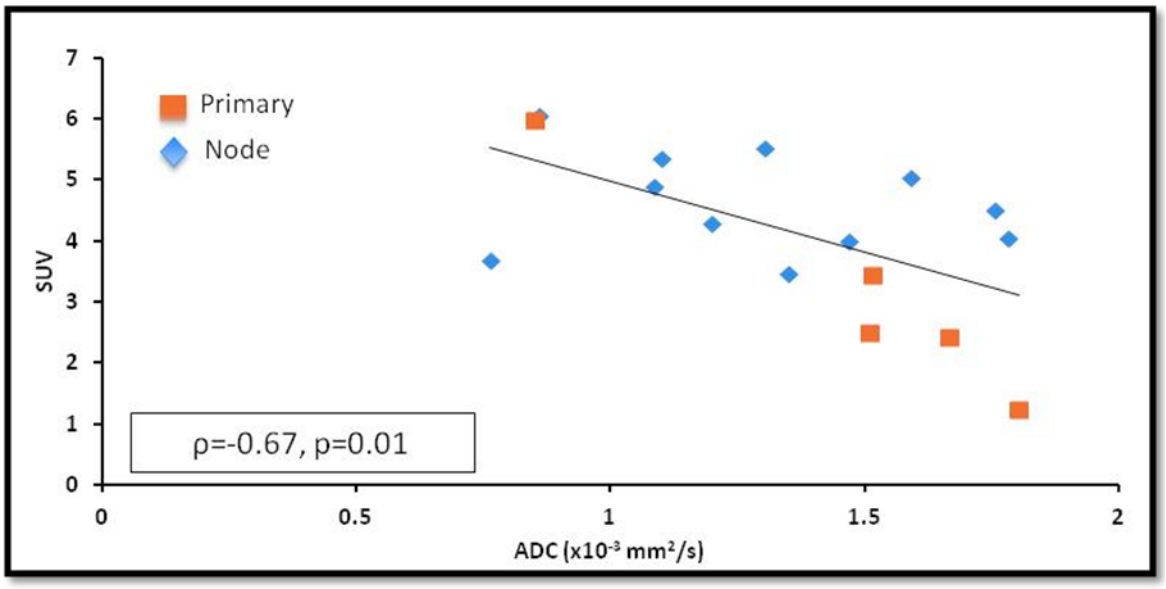

Fig. 18. Relationship between pre-treatment mean SUV and pre-treatment mean ADC showing a significant strong negative inverse correlation.

For a single patient who was NED at last clinical follow-up, both MRI and ^{18}F-FDG PET/CT post treatment showed no evidence of disease at primary tumor site and neck nodal metastases. **Fig. 19** shows the DW-MRI and ^{18}F-FDG PET/CT images from a patient who was NED. The ADC values (mean ± SD) for the ROIs drawn on primary tumor were 0.85 ± 0.27 x 10^{-3} mm^2/s, 1.49 ± 0.13 x 10^{-3} mm^2/s for pre-Tx, Wk2-3 Tx respectively. The ADC values for the ROI in neck nodal metastases showed similar trends in the metric values and were as follows 0.86 ± 0.20 x 10^{-3} mm^2/s, 1.39 ± 0.08 x 10^{-3} mm^2/s for pre-Tx, Wk2-3 Tx. pre-Tx SUV (mean ± SD) values for primary tumor and neck nodal metastases were 5.99 ± 0.61 and 6.06 ± 0.49 respectively.

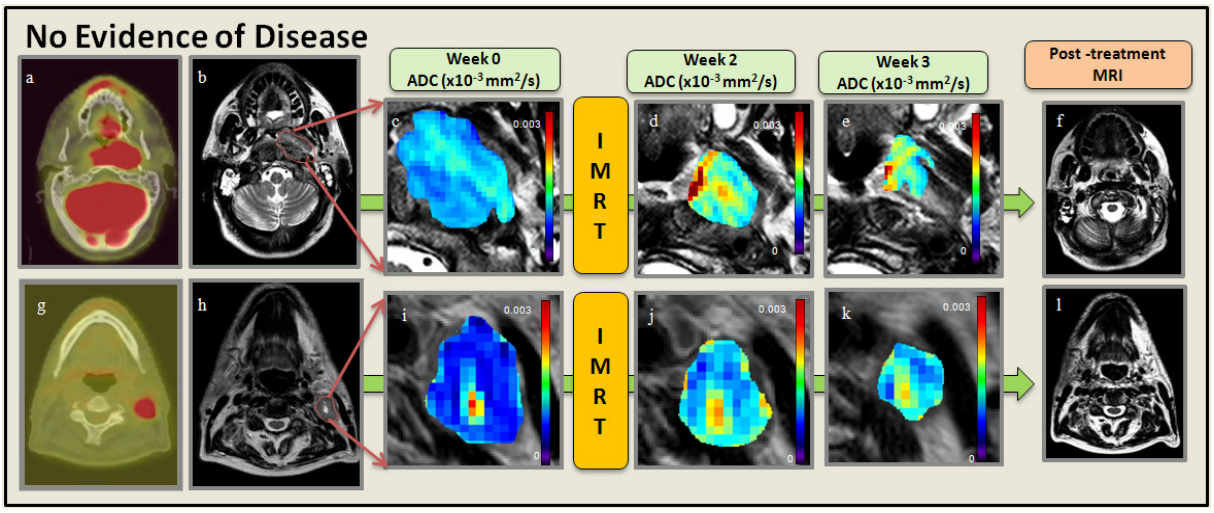

Fig. 19. Representative NED patient. **a.** and **g.** pre-Tx PET/CT of the primary tumor and a neck nodal metastasis. **b.** and **h.** Primary tumor and representative neck nodal metastasis contoured over a T2W MRI. **c.** and **i.** pre-Tx ADC map overlaid on T2W MRI. **d.** and **j.** Wk2-Tx ADC map overlaid on T2W. **e.** and **k.** Wk3-Tx ADC map overlaid on T2W. **f.** and **l.** T2W MRI post-Tx with no evidence of primary tumor and neck nodal metastases.

Three patients were AWD on last clinical follow-up, and 1 patient had an unknown primary tumor site. Both, MRI and ^{18}F-FDG PET/CT post treatment showed no evidence of disease at primary tumor site but the neck nodal metastases were still present. **Fig. 20** shows the DW-MRI and ^{18}F-FDG PET/CT images from a patient who was AWD. The ADC (mean ± SD) for the primary tumors were 1.73 ± 0.09 x 10^{-3} mm^2/s, 2.01 ± 0.36 x 10^{-3} mm^2/s for pre-Tx,

Wk2-3 Tx respectively. The ADC values for the neck nodal metastases were 1.34 ± 0.22 x 10^{-3} mm^2/s, 1.47 ± 0.35 x 10^{-3} mm^2/s, 1.93 ± 0.22 x 10^{-3} mm^2/s for pre-Tx, Wk2-3 Tx, and post-Tx respectively. SUV mean pre-Tx value for Primary tumor and neck nodal metastases were 1.84 ± 0.83 and 4.85 ± 0.75 respectively.

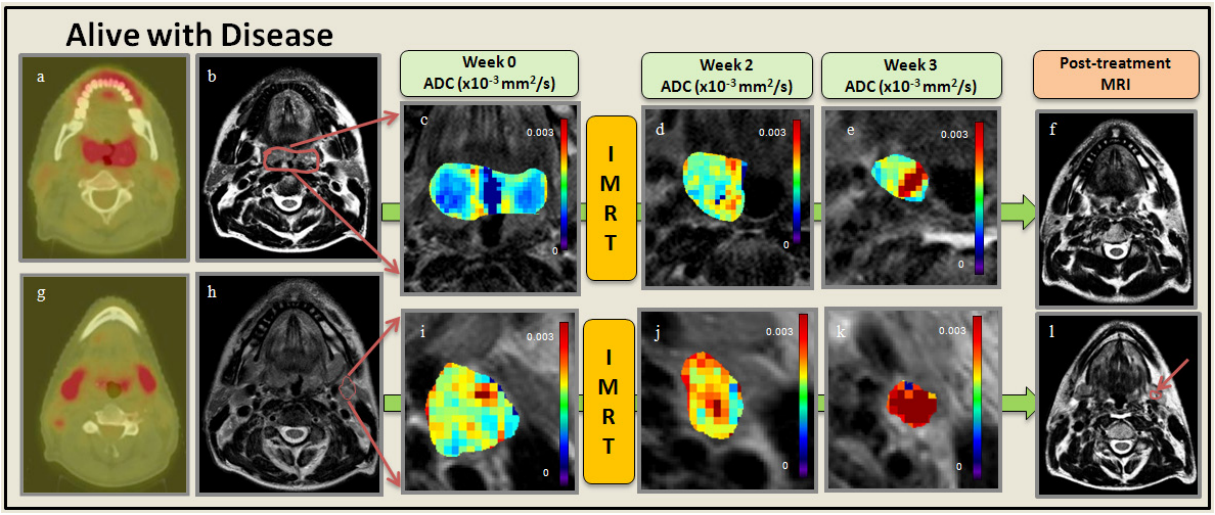

Fig. 20. Representative AWD patient. **a.** and **g.** pre-Tx PET/CT of the primary tumor and two neck nodal metastases. **b.** and **h.** Primary tumor and representative neck nodal metastasis contoured over a T2W MRI. **c.** and **i.** pre-Tx ADC map overlaid on T2W MRI. **d.** and **j.** Wk2-Tx ADC map overlaid on T2W. **e.** and **k.** Wk3-Tx ADC map overlaid on T2W. **f.** and **l.** T2W MRI post-Tx with no evidence of primary tumor but with presence of neck nodal metastasis.

The two patients who were DOD died, 2 months and 6 months after treatment. **Fig. 21** shows the DW-MRI and ^{18}F-FDG PET/CT images from a patient who was DOD. The ADC values (mean ± SD) for the primary tumor were 1.51 ± 0.01 x 10^{-3} mm^2/s, 1.83 ± 0.18 x 10^{-3} mm^2/s for pre-Tx, and Wk2-3 Tx, respectively. The ADC values for the neck nodal metastases were 1.39 ± 0.06 x 10^{-3} mm^2/s, 1.61 ± 0.28 x 10^{-3} mm^2/s, 0.98 ± 0.29 x 10^{-3} mm^2/s for pre-Tx, Wk2-3 Tx, and post-Tx respectively. SUV mean pre-Tx value for primary tumor and neck nodal metastases were 2.98 ± 0.66 and 3.93 ± 0.45 respectively. A summary of data from the three different survival groups as DOD, AWD and NED is shown in **Table 2.**

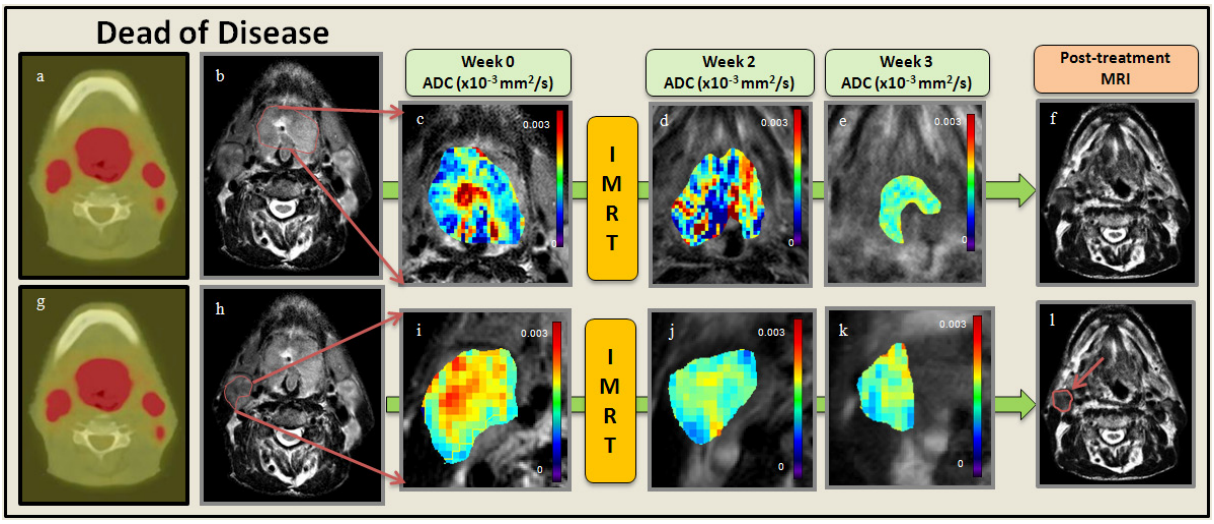

Fig. 21. Representative DOD patient. **a.** and **g.** pre-Tx PET/CT of the primary tumor and three neck nodal metastases. **b.** and **h.** Primary tumor and representative neck nodal metastasis contoured over a T2W MRI. **c.** and **i.** pre-Tx ADC map overlaid on T2W MRI. **d.** and **j.** Wk2-Tx ADC map overlaid on T2W. **e.** and **k.** Wk3-Tx ADC map overlaid on T2W. **f.** and **l.** T2W MRI post-Tx with no evidence of primary tumor but with presence of neck nodal metastasis.

Fig. 22 and **23** show different trends for the three survival groups DOD, AWD and NED by representative patients. The results depicted in individual patients are the relative percentage (%) change in ΔADC for primary tumors and neck nodal metastases. The results between Pre- and Wk2 Tx for primary tumor and neck nodal metastases in a patient with NED were 86.55% and 68.60% while for AWD and DOD they were 18.51%, 11.88% and 29.76%, 25.77%, respectively. The percentage (%) change in ΔADC for primary tumors and neck nodal metastases between Pre- and Wk3 Tx for patients with NED was 64.26%, 54.65% while for AWD and DOD it was 36.48% , 53.58%, and 24.13%, -11.14%, respectively. A summary of data from the three different survival groups as DOD, AWD and NED is shown in **Table 2**.

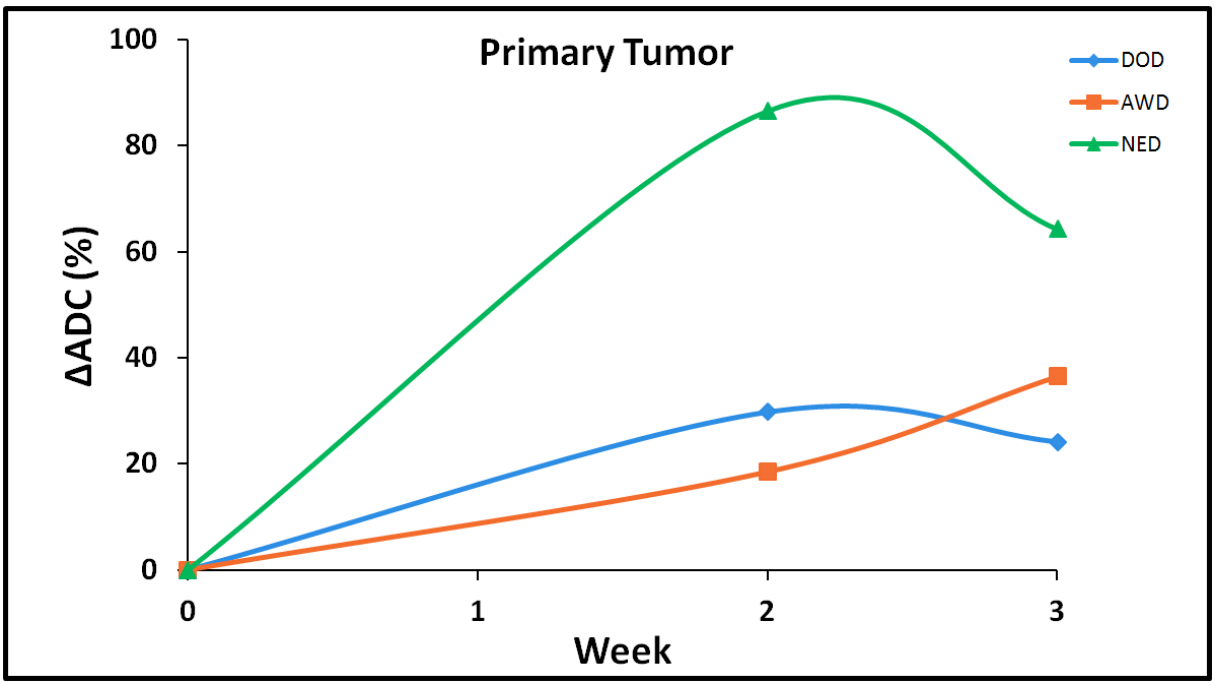

Fig. 22. ADC Pre- and intra-Tx (2nd and 3rd week) versus week of treatment in primary tumors of HPV – HNSCC patients who were classified based on survival as DOD, AWD and NED.

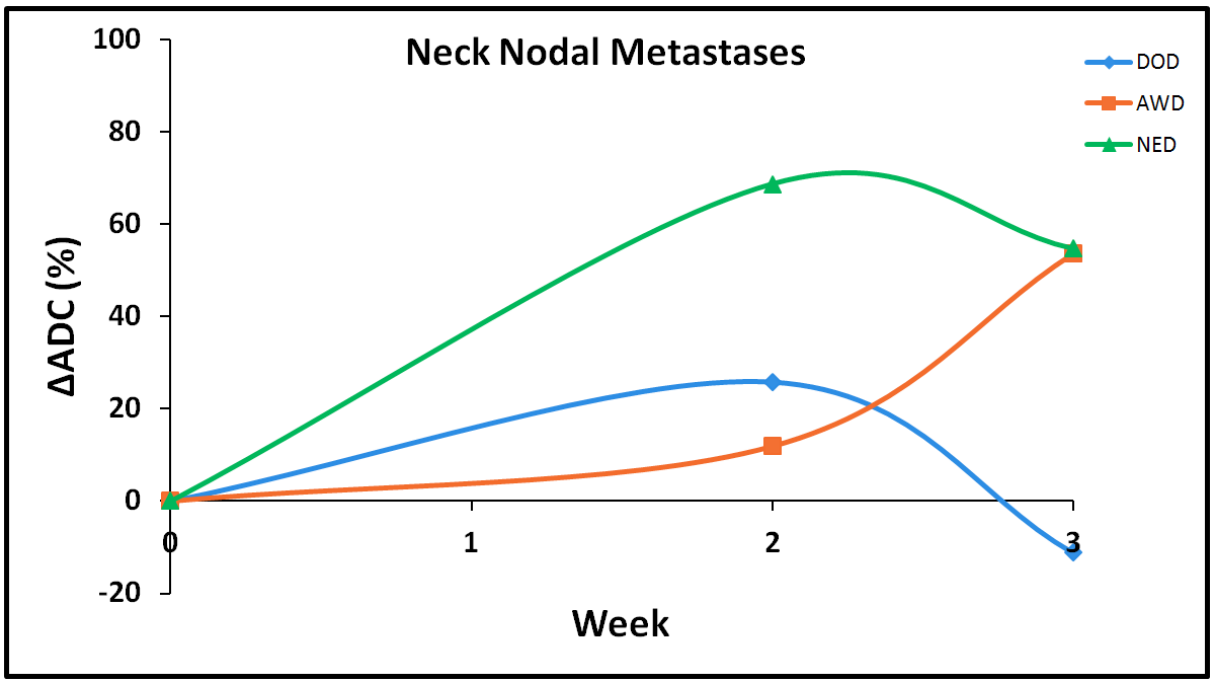

Fig. 23. ADC pre- and intra-Tx (2nd and 3rd week) versus week of treatment in neck nodal metastases HPV – HN-SCC patients who were classified based on survival as DOD, AWD and NED.

Table.7 ADC metric values for HPV– HNSCC patients who were classified based on survival as DOD, AWD and NED before and during and post CRT.

MRI	DOD $ADC_{mean}(10^{-3}\ mm^2/s)$		AWD $ADC_{mean}(10^{-3}\ mm^2/s)$		NED $ADC_{mean}(10^{-3}\ mm^2/s)$	
	Primary	**Node**	**Primary**	**Node**	**Primary**	**Node**
pre-Tx	1.51±0.36	1.43±0.58	1.66±0.41	1.26±0.19	0.86±0.20	0.85±0.27
During-Tx (2-3 weeks)	1.92±0.33	1.54±0.11	2.12±0.38	1..41±0.38	1.39±0.47	1.50±0.44
Post-Tx	*No Primary*	0.98±0.29	*No Primary*	1.93±0.22	*No Primary*	*No Node*

Fig. 24 and **25** show Pre- and Wk3-Tx ADC in representative patients from three clinical follow-up groups DOD, NED and AWD. The histograms display the changes in diffusion for primary tumor and neck nodal metastases.

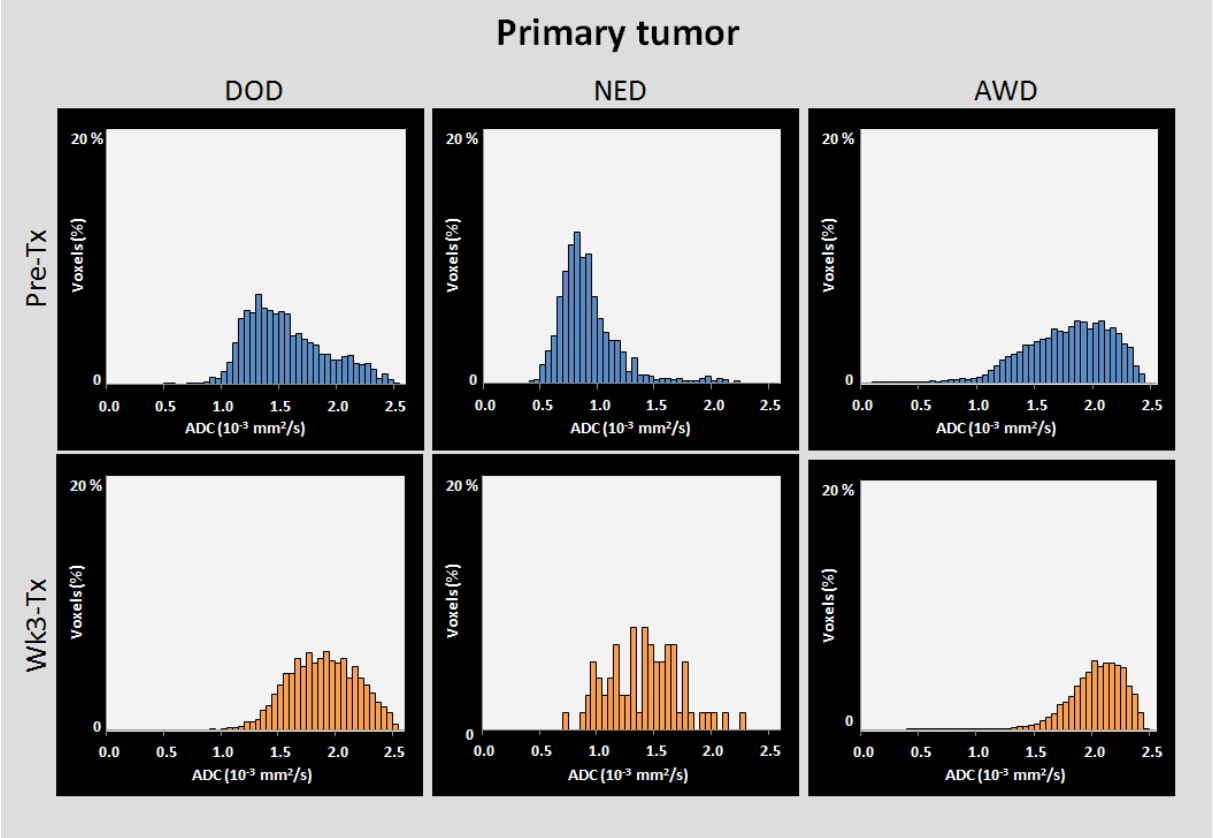

Fig. 24. Histogram plots depicting changes in the distribution from Pre- to Wk-3 during Tx for ADC (x 10^{-3} mm^2/s) in primary tumors of HNSCC patients. Three clinical follow-up groups represented are DOD, NED and AWD.

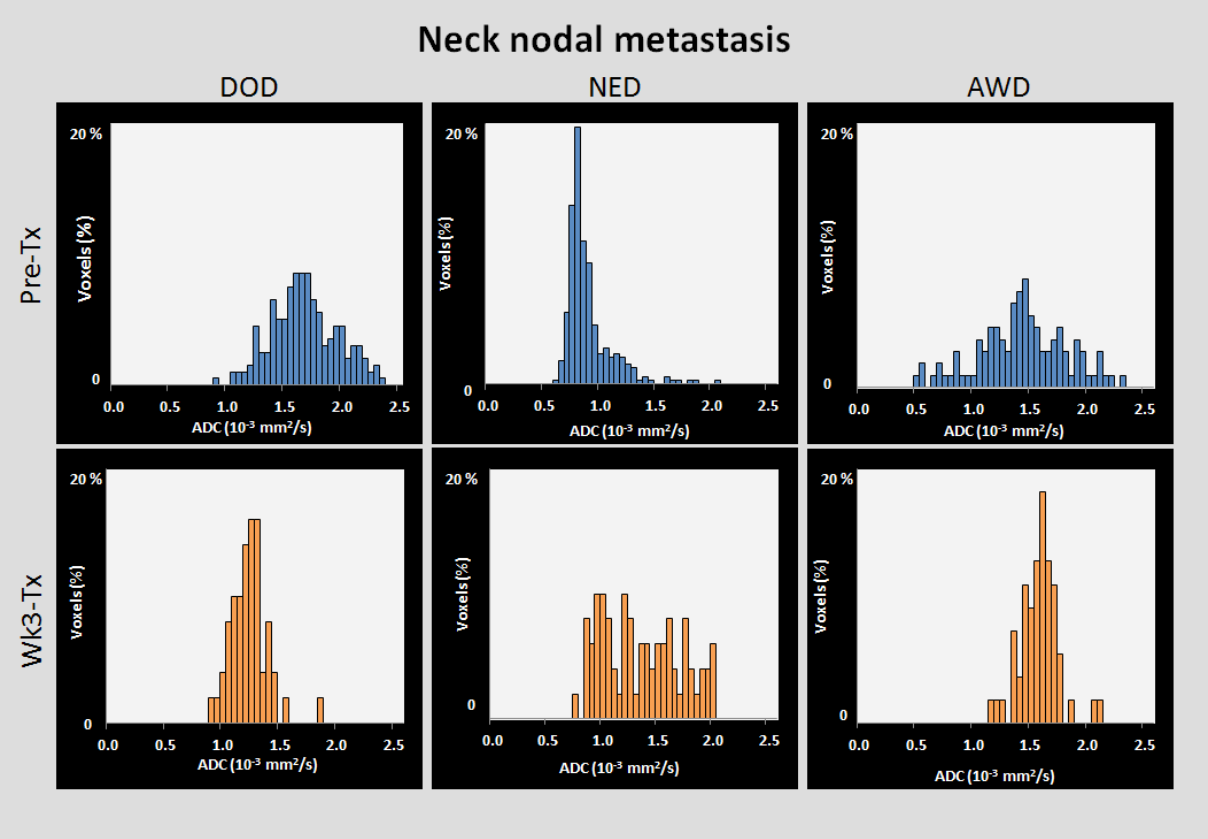

Fig. 25. Histogram plots depicting changes in the distribution from Pre- to Wk-3 during treatment for ADC (x 10^{-3} mm^2/s) in neck nodal metastases of HNSCC patients. Three clinical follow-up groups represented are DOD, NED and AWD.

4.2. Part II: Novel application of the reversed gradient Diffusion Weighted MRI method for tumor response assessment in head and neck cancers (including the novel design of a Phantom Distortion Assessment - *Experience at Meixoeiro University Hospital of Vigo, Spain*

Fig. 26 shows original images of the phantom-DA and one of the patients. In addition, two distorted images with opposite phase encoding directions and its corresponding corrected image are represented. The visual improvement in the registration was notable, and in patient's sagittal slices we see that the registration of the cord and the brain of the corrected images fit much better to the real anatomic position on the CT.

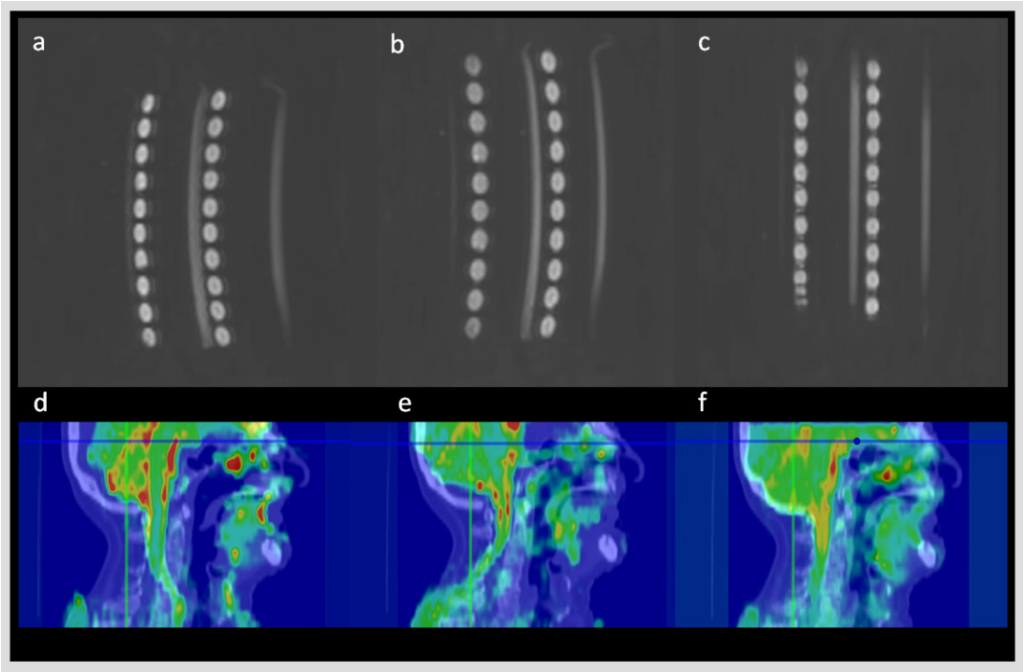

Fig. 26. The upper figure shows the DW-MRI with b=0 for the Phantom-DA: a. Phase encoding direction: Antero-Posterior, fat shift anterior (AP); b. Phase encoding direction: Antero-Posterior, fat shift posterior (PA); c. Corrected by the reversed gradient method. The lower figure shows the registration of CT and DW-MRI with b=0 for a patient: d. Phase encoding direction: Antero-Posterior, fat shift anterior (AP); e. Phase encoding direction: Antero-Posterior, fat shift posterior (PA); f. Corrected by the reversed gradient method.

As distortion is the main disadvantage of using DW-MRI for tumor response assessing, correction will be validated by the reversed gradient method in order to show the improvement in image registration and accurate ADC measurements. Mutual information will be used for the numerical quantification of distortion. The DW-MRI images with different b-values were used, considering distorted and undistorted images corrected by the reversed gradient method. They were registered with the T2w study. As perfect registration, two identical T2w images of the phantom-DA were chosen, and the mutual information value obtained was 1.33426.

Table 8 displays the different mutual information values and difference for the registration of the images with T2w, with and without correction. An average improvement of 23% in mutual information was obtained.

Table 8. Mutual Information values for the registration of T2w MRI and DW-MRI with different b-values of the phantom-DA. % difference is calculated with respect to averaged mutual information of raw studies, considering both gradients. Raw AP and raw PA correspond to the reversed gradients applied for phase encoding direction in the AP dimension and different fat shifts.

Phantom-DA	Raw AP	Raw PA	Corrected	% Difference
b=0 s/mm²	0.420	0.461	0.499	13.21%
b=600 s/mm²	0.482	0.403	0.543	22.73%
b=1000 s/mm²	0.453	0.377	0.563	35.59%

The patient's datasets were processed by calculating the upper value of mutual information in the registration of the T2w MRI of the patient with itself and obtained a value of 1.853.

Table 9 shows different mutual information values for the registration of the MRI images, with and without distortion correction, with T2w for each dose point. An average registration improvement of 21% was obtained.

Table 9. - Mutual information values for different DW-MRI of the three patients with different b-values and T2w MRI. % difference is calculated with respect to averaged mutual information of raw studies, considering both gradients. Raw AP and raw PA correspond to reversed gradients applied for phase encoding direction in the AP dimension and different fat shifts.

Patient	b-value (s/mm^2)	Raw AP	Raw PA	Corrected	% Difference
#1	**0**	0.563	0.656	0.872	43.1 %
#2	**0**	0.308	0.454	0.775	103 %
#3	**0**	0.439	0.548	0.548	11.0 %
#1	**600**	0.655	0.325	0.900	83.7 %
#2	**600**	0.381	0.445	0.730	76.8 %
#3	**600**	0.545	0.522	0.567	6.28 %

The ADC value of water in the phantom-DA was calculated. The ADC value obtained for water at 22º C is $(2.13 \pm 0.19) \times 10^{-3}$ mm^2 / s for distorted images and $(2.19 \pm 0.05) \times 10^{-3}$ mm^2 / s for undistorted images. Differences in both values were not significant and they correspond to published data (122): 2.13×10^{-3} mm^2 / s.

Tumor response was evaluated by measuring the difference in ADC values during treatment for raw and corrected datasets in one of the three patients (84, 123). **Fig. 28** shows the ADC change voxel by voxel for both datasets. A closer cluster in ADC can be seen, as expected of the corrected dataset, and observations of the average data (**Fig. 28**) indicate that the ADC increment in the 16th fraction is only noticed for corrected data, probably because distortion adds noise to the original signal and the correlation of the ADC increment with dose is lost. Accurate ADC measurements can be made using the corrected method, which is critical for an imaging biomarker of response.

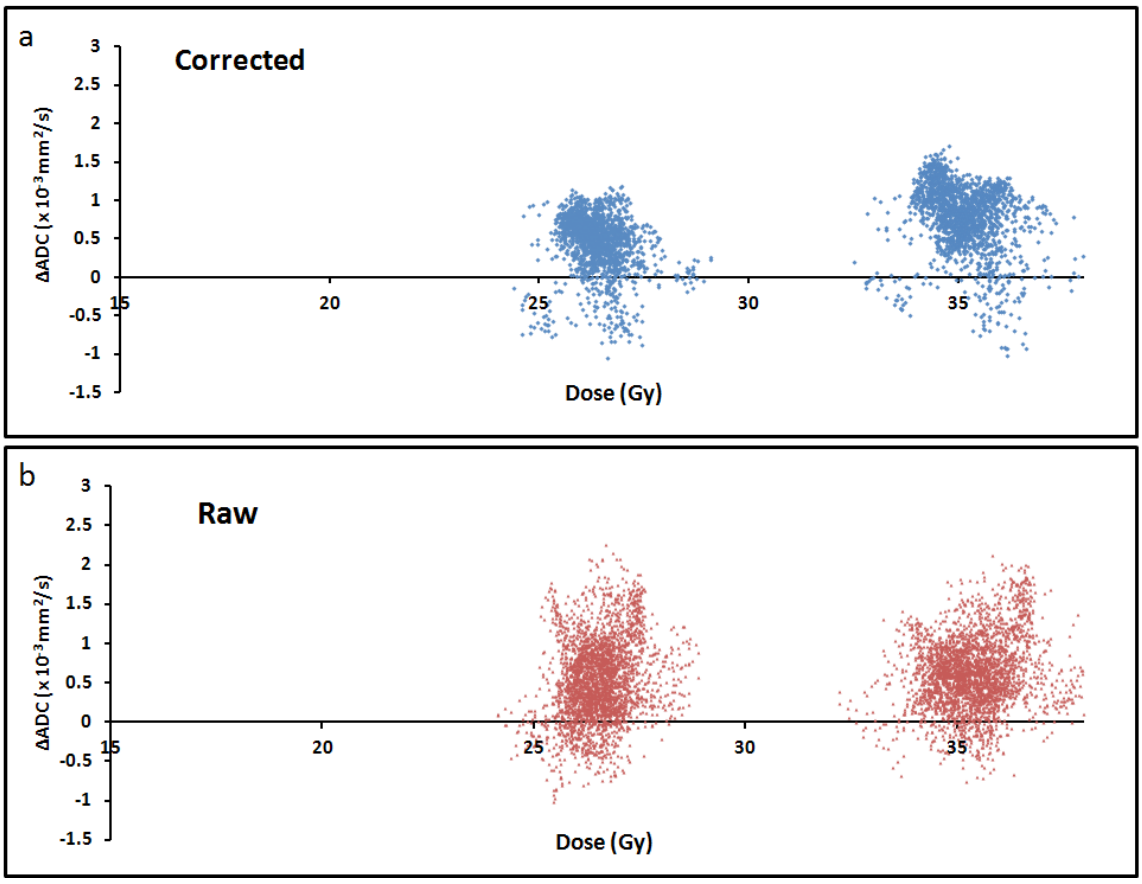

Fig. 27. ΔADC (10^{-3} mm^2/s) vs Dose (Gy) in the tumor. Each point represents the voxel ΔADC values extracted from **a.** DW-MRI RAW, **b.** DW-MRI corrected at the 12th and 16th fractions of Treatment.

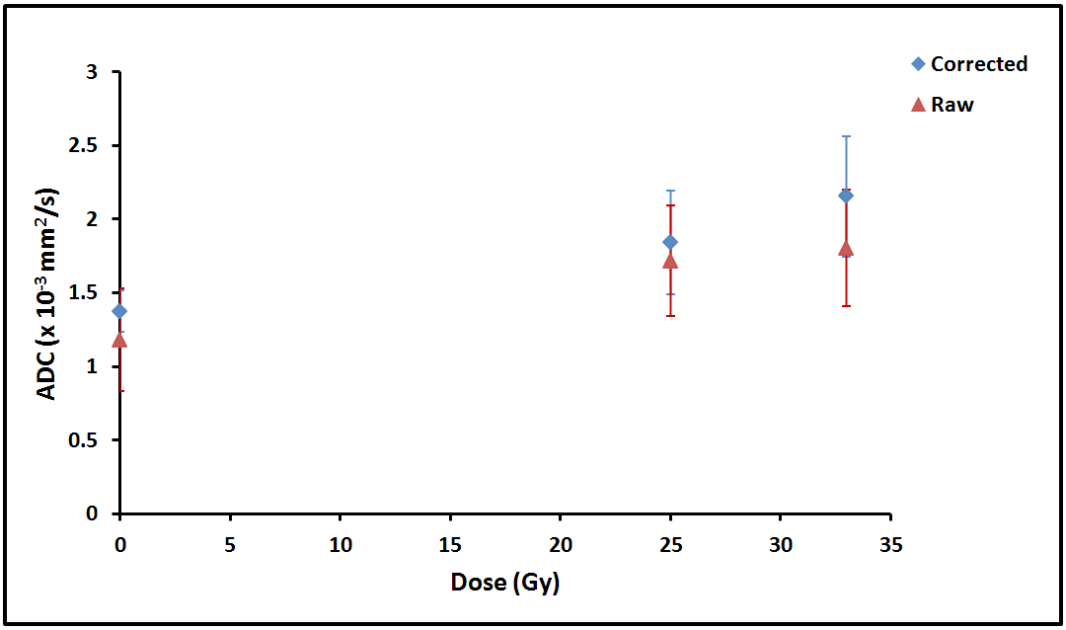

Fig. 28. Dose course of ADC (10^{-3} mm^2/s) in the tumor of a patient at the 12th and 16th fractions of Treatment.

4.3. Part III Intra Voxel Incoherent Motion Diffusion Weighted MRI and Dynamic Contrast Enhanced MRI methods for tumor response assessment in Brain Metastases

– Experience at Memorial Sloan-Kettering Cancer Center, USA

4.3.1. Repeatability and reproducibility of Quantitative Imaging Biomarkers: Diffusion Weighted MRI as a test model

ADC metric value for distilled water at 0°C is 1.1 x 10^{-3} mm^2/s (124). The phantom required 30 minutes to reach an equilibrium temperature of 0°C (**Fig. 29**). The diffusion metric values of water show a high sensitivity to temperature (2.4% change in value per degree Celsius) (120). Hence, it is a prerequisite to have a stable temperature over the scan time.

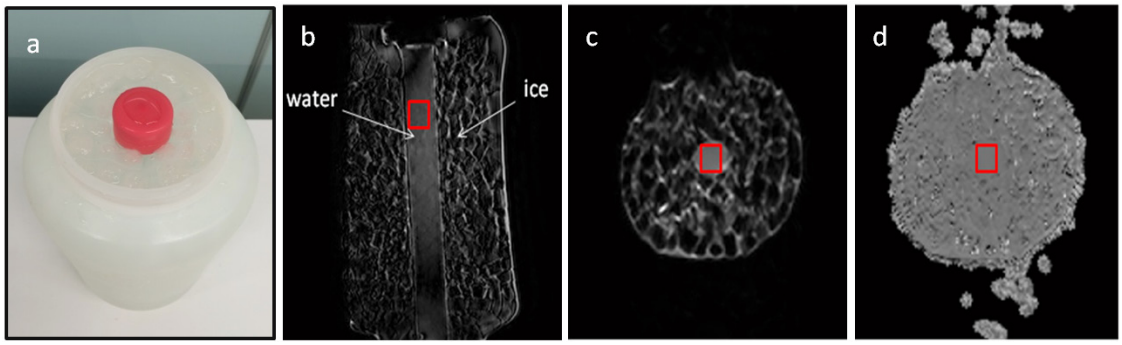

Fig. 29. a. Illustrates the phantom filled with ice. **b.** Sagittal representative T2w image of the phantom. **c.** Axial representative b=0 s/mm^2 image of the phantom. **d.** Axial ADC map of the phantom. Note: Red box denoted the ROI used for ADC measurement.

This study showed that ADC measurements of the ice-water phantom at the ROI (**d.**) were consistent with the literature value of 1.1 x 10^{-3} mm^2/s at 0°C (120). In **Fig.30** are the grouped ADC values, acquired at b-values of 0, 500, 800, 1000 and 2000 s/mm^2, from the ice-water phantom for each scanner, Philips-3T and GE-3T. A total of 24 measurements were obtained within a 5% (blue field in **Fig. 30**) of the literature value of 1.1 x 10^{-3} mm^2/s (orange line in **Fig. 30**). The mean value of ADC for the GE-3T was (mean ± SD) 1.09 ± 0.01 x 10^{-3} mm^2/s and for GE-1.5T was (mean ± SD) 1.11 ± 0.02 x 10^{-3} mm^2/s.

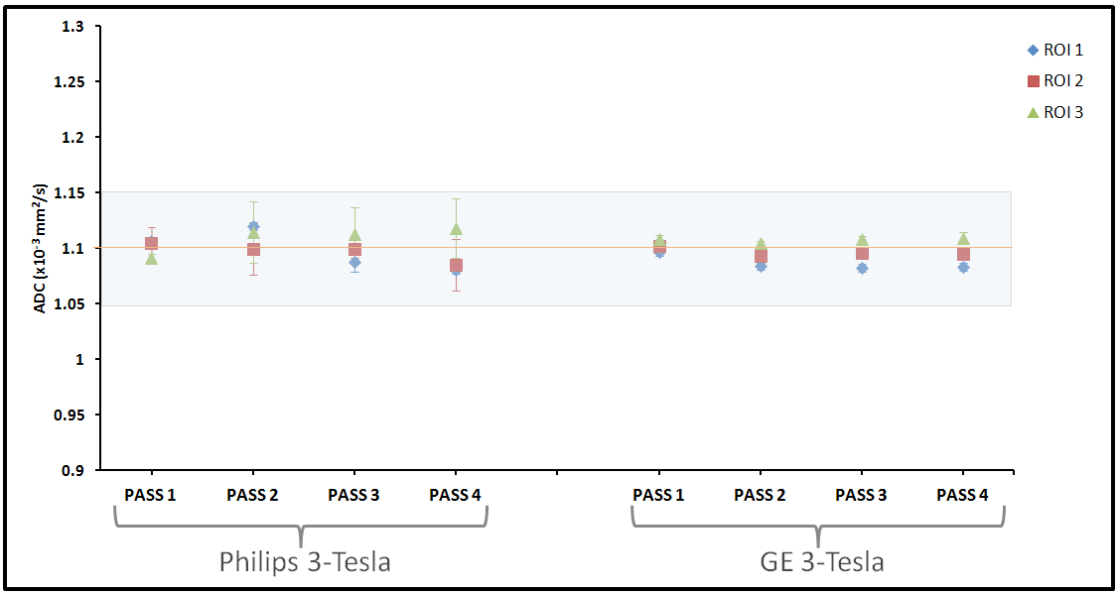

Fig. 30. Measurements of ADC in the ice-water phantom for 4 passes and three different ROIs, separated by vendor.

ADC values acquired at Philips-3T and GE-3T showed no statistical difference between the 4 measurements (passes) performed within and across vendors and between different ROIs drawn. The coefficient of variation of the repeatability measurements for GE-1.5T was 1.2%. Meanwhile, the coefficient of variation of the repeatability measurements for GE-3T was 0.9%. Therefore, they indicate that the ADC measured for the phantom is repeatable and reproducible.

4.3.2. Intra Voxel Incoherent Motion Diffusion Weighted MRI and Dynamic Contrast Enhanced MRI methods for tumor response assessment in Brain Metastases

The final analysis was performed on the 9 BM patients. Patients were grouped as follows based on clinical outcome: NED=0, AWD=7, DOD=1 and DOC = 1 (**Table 6**). A total of 39 DW-MRI (pre-, early post-Tx and follow up) and 18 DCE-MRI (pre- and early post-Tx) imaging studies were analyzed to capture early SRS treatment response.

There is a significance strong positive correlation between mean ADC and mean D (ρ=0.987). There is a moderate negative correlation between mean D and mean f and K^{trans} values (ρ=-0.320, ρ=-0.330, respectively). A significance strong positive correlation is also shown between mean f and mean v_p and K^{trans} values (ρ=0.742, ρ=725, respectively). In addition, a significance strong positive correlation between mean K^{trans} and mean v_e value was found (ρ=0.547) and a moderate positive correlation between mean Ktrans and mean v_p (ρ=0.380) for BM patients with AWD. All Pearson correlation coefficients are listed in **Table 10** for BM patients who were AWD. Statistical analysis for correlations was not performed for patients who were DOD and DOC to avoid patient bias due to low sample size.

Table 10. Summary statistics of Pearson correlation between all imaging metrics derived from IVIM DW-MRI and DCE-MRI for BM patients who were AWD. *Note: Asterisks (*) showing sig nificance between all imaging metrics.*

	Pearson Correlation AWD (*p-value ≤ 0.05)				
Metrics	**D**	**f**	**K^{trans}**	**v_e**	**v_p**
ADC	ϱ=0.987*	ϱ=-0.200	ϱ=-0.260	ϱ=-0.001	ϱ=-0.106
D		ϱ=-0.320	ϱ=-0.330	ϱ=-0.036	ϱ=-0.015
f			ϱ=0.725*	ϱ=0.209	ϱ=0.724*
K^{trans}				ϱ=0.547*	ϱ=0.380
v_e					ϱ=-0.005
Absolute correlation considered					
Strong 0.5<ϱ≤1, Moderate 0.3≤ϱ≤0.5, Weak ϱ<0.3					

The relative percentage change in the IVIM metrics (ΔADC, ΔD and Δf) and DCE-MRI SM metrics (ΔK^{trans}, Δv_e, Δv_p) between pre- and early post-Tx (2-24 hours) for the BM patient who DOD was -8.00%, -9.28%, -4.26%, -25%, -21.65%, 196%. The relative percentage change in the IVIM metrics (ΔADC, ΔD and Δf) and DCE-MRI SM metrics (ΔK^{trans}, Δv_e, Δv_p) between pre- and early post-Tx (2-24 hours) for the BM patient who DOC was 12.32%, 19.5%, 3.99%, -29.59%, -29.42%, 128%.

Fig. 31 and **32** show the pre- and early post-Tx IVIM and DCE-MRI SM metric maps from a representative BM patient.

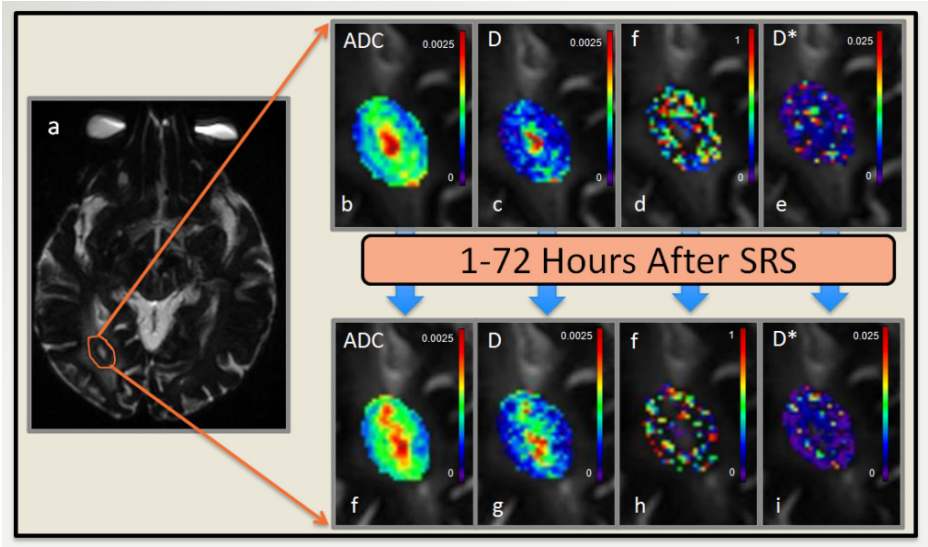

Fig. 31. Brain Metastasis patient depicting the early changes in IVIM metrics pre- and early post-Tx. **a.** A brain metastasis contoured on a T2w MRI. **b.-e.** pre-Tx ADC, D, f, D* maps**. f.-i.** Early post-Tx ADC, D, f, D* maps. All maps are overlaid on T2w MRI.

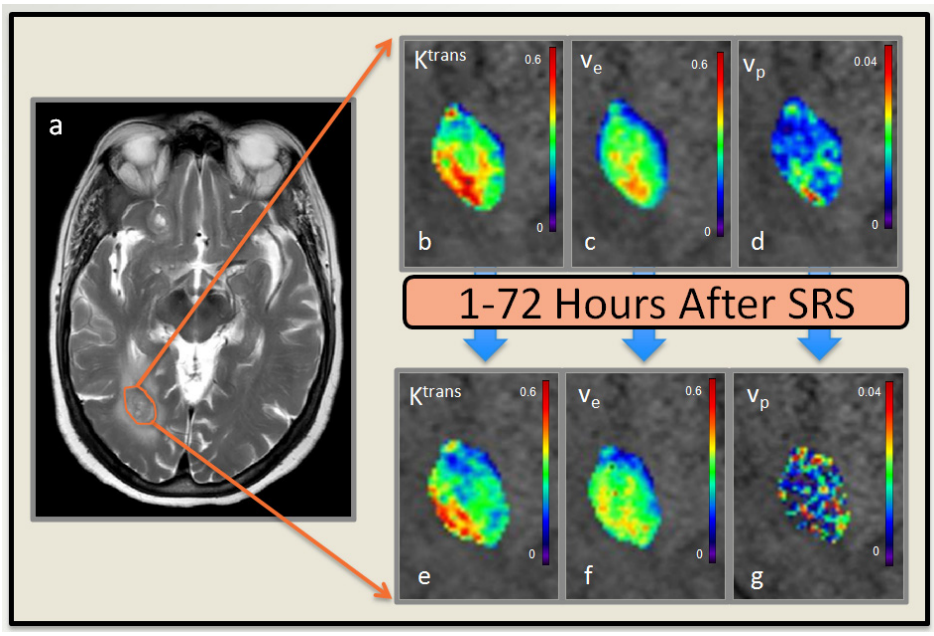

Fig. 32. Representative Brain Metastasis patient depicting the early changes in DCE metrics pre- and early post-Tx. **a.** Brain metastasis contoured on a T1w MRI. **b.-e.** pre-Tx K^{trans}, ve, vp maps. **f.-i.** Early post-Tx K^{trans}, v_e, v_p maps. All maps overlaid on T1w MRI.

Seven patients were AWD on last clinical follow-up. The pre-Tx ADC, D and f (mean ± SD) were 0.89 ± 0.33 x 10^{-3} mm^2/s, 0.69 ± 0.33 x 10^{-3} mm^2/s, and 0.27 ± 0.09 respectively. The pre-Tx K^{trans}, v_e and v_p (mean ± SD) values were 0.19 ± 0.09 min^{-1}, 0.20 ± 0.09, and 0.01 ± 0.01, respectively. The early post-Tx ADC, D and f (mean ± SD) were 1.03 ± 0.48 x 10^{-3} mm^2/s, 0.85 ± 0.54 x 10^{-3} mm^2/s, and 0.25 ± 0.10 respectively. The early post-Tx K^{trans}, v_e and v_p (mean ± SD) values were 0.17 ± 0.06 min^{-1}, 0.28 ± 0.23, and 0.01 ± 0.01, respectively.

The relative percentage changes in the IVIM metrics (ΔADC, ΔD and Δf) and DCE-MRI SM metrics (ΔK^{trans}, Δv_e, Δv_p) between pre- and early post-Tx (2-24 hours) for the AWD group of patients were 15.43%, 23.64%, -8.05%, -10.95%, 41.35%, -44.39%. A summary of data from the group of AWD is shown in **Table 11.** In **Fig. 33** are pre- and early post-Tx values for ADC, D and K^{trans} in a representative patient. The histograms display the changes in diffusion and vascular permeability in BM patients who were AWD.

Table 11: Relative percentage change ΔADC, ΔD, Δf, ΔK^{trans}, Δv_e, Δv_p, pre- and post-SRS (2-24 hours), values for BM patients who were classified based on survival as AWD.

ΔADC (2-24 hours)	ΔD (2-24 hours)	Δf (2-24 hours)	ΔK^{trans} (2-24 hours)	Δv_e (2-24 hours)	Δv_p (2-24 hours)
15.43 %	23.64 %	- 8.05 %	- 10.95 %	41.35 %	- 44.39 %

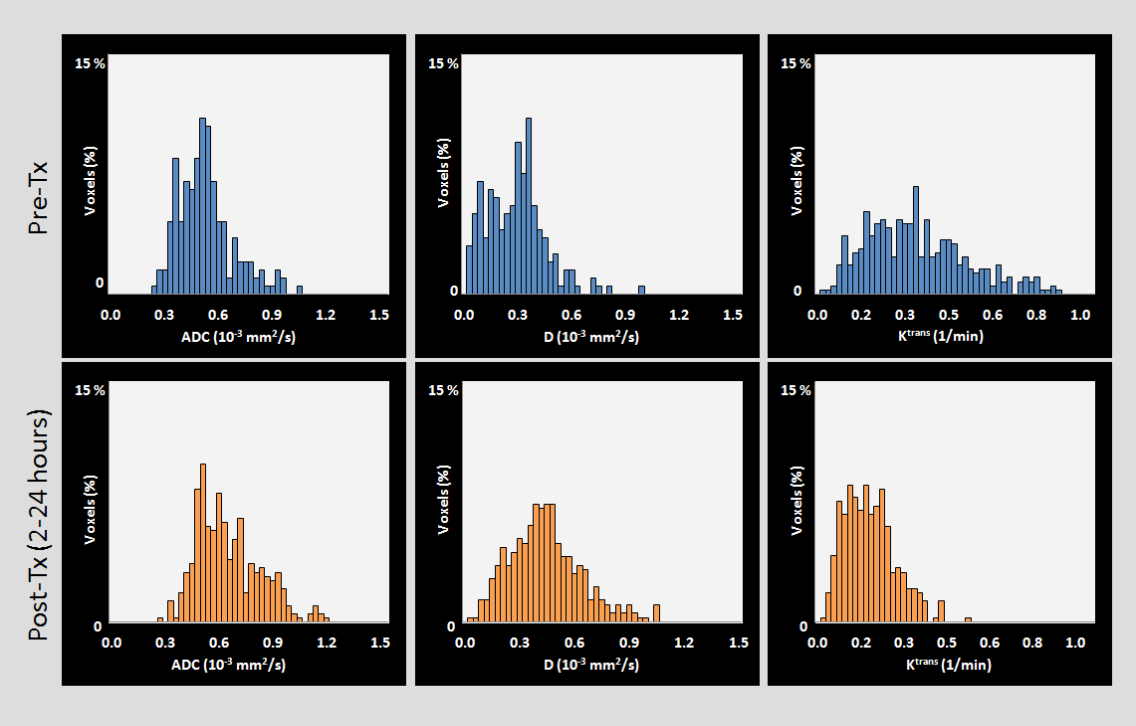

Fig. 33. Corresponding distribution histograms plots for the metrics, ADC (x 10^{-3} mm^2/s), D (x 10^{-3} mm^2/s) and K^{trans} (min^{-1}) of a representative BM patient.

Fig. 34 and **35** illustrate ADC and tumor volume changes during long term follow up for three representative patients.

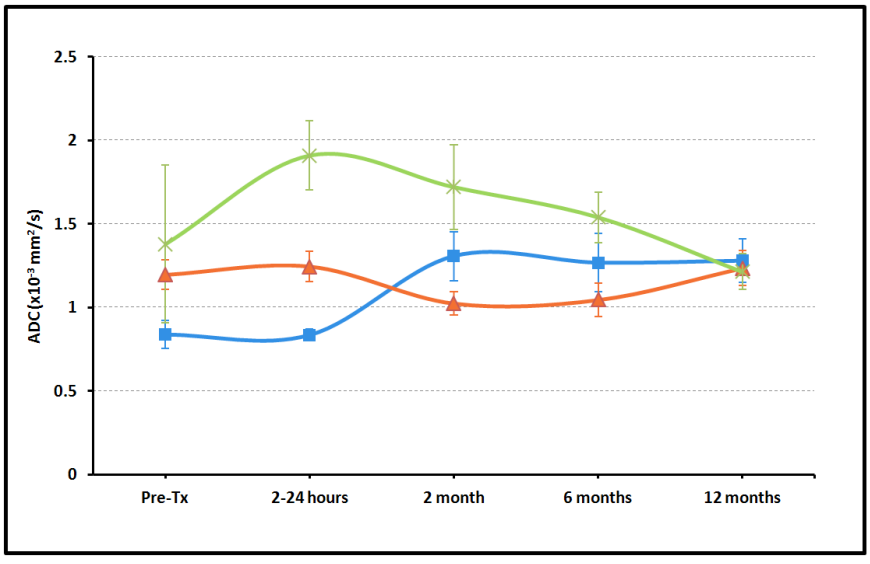

Fig. 34. Time course trend of ADC at differ time points (pre-, post (2-24 hours, 2 month, 6 month, 12 months) for three representative BM patients.

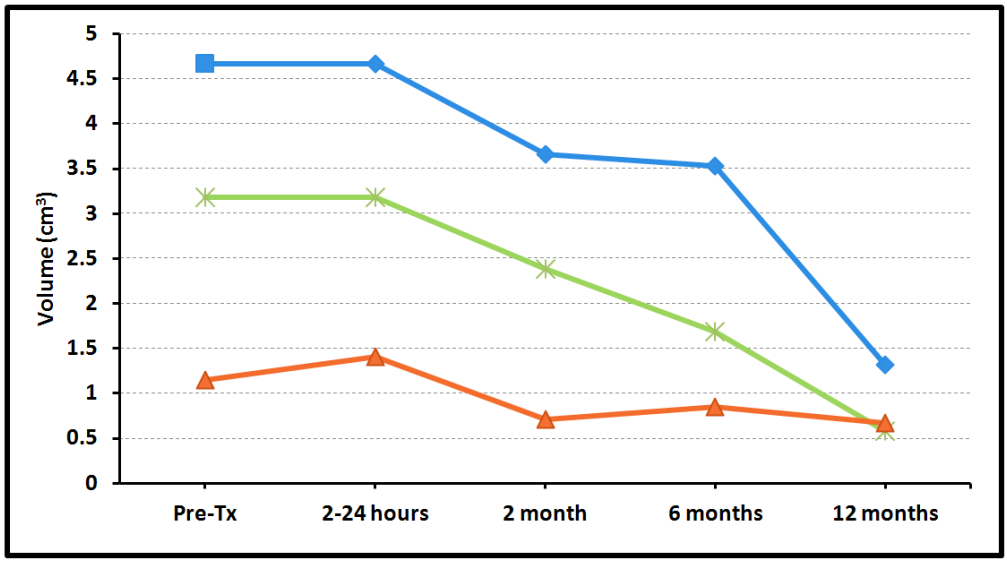

Fig. 35. Time course trend of tumor volume at differ time points (pre-, post (2-24 hours, 2 month, 6 month, 12 months) for three representative BM patients.

Statistical tests were not performed to compare the 3 group (AWD, DOD and DOC) in order to avoid patient bias due to low sample size in the study [see **Table 5**]. This study is showing for the first time that relative percentage changes occur in the imaging metrics in BM patients early within 2-24 hours post SRS. In BM patients who were AWD, there is a substantial change in imaging metric values for both DCE-MRI and IVIM DW-MRI pre- and early post-Tx. A preliminary, initial Student t-test showed that when the patients in the AWD were compared based on the primary tumor site (for example 4 patients with lung primary tumor versus 2 patients with melanoma primary tumor [see **Table 5**]) the mean value of metric v_p was significantly different ($p<0.03$) for early post-Tx. Once again, it is important to clarify that in-depth statistical analysis was not in the scope of this study. This is a feasibility study showing trends observed in these BM patients being treated with SRS. It therefore constitutes a building block for future studies in clinical settings that will use functional imaging in adaptive RT settings.

Chapter V

Chapter V: Discussion

Chapter V of this thesis discusses in depth the three studies which have in common the central theme and motivation of using functional imaging in RT settings for future application in adaptive RT.

The first part of the discussion is focused on a prospective study of HPV- HNSCC patients analyzing ^{18}F-FDG, pre- and post-Tx, and DW-MRI pre- during and post-Tx in primary tumors and neck nodal metastases, integrating them into the RT setting.

The second part of the discussion is focused on the accurate measurement of ADC derived from DW-MRI, through the correction of geometrical distortion in DW-MRI using the reversed gradient method in HPV- HNSCC patients who underwent RT.

The last part of the discussion is divided into two subparts. The first focuses on repeatability and reproducibility of ADC measurements derived from DW-MRI using a temperature-controlled fluid phantom constructed by Chenevert et al. (95). The second focuses on a prospective study of BM treated with SRS assessing early (1-72 hours post-Tx) treatment response evaluating imaging metrics derived from IVIM DW- and DCE- MRI.

5.1. Part I: ARTFIBio project: A novel framework for adaptive radiotherapy based on functional images - *Experience at Meixoeiro University Hospital of Vigo, Spain*

HNSCC is one of the major types of cancer that can be linked to alcohol consumption and tobacco smoking; it typically originates from the mucosal epithelia of the oral cavity, pharynx and larynx (125). Locoregional control can be achieved through treatment with radiation or surgery at the early stages, but only 40% of patients with advanced stages will survive more than 5 years (125). Regardless of recent advances in surgical and oncologic treatments, the overall survival rate of patients with HNSCC has unfortunately not improved much in recent years. Delays in diagnosis (followed by locoregional failure) and a late salvage treatment at the recurrence of the disease are important causes of unfavorable outcomes in this type of cancer. A priori predictors of outcome and predictive biomarkers of treatment response are desperately needed to advance patient care and individualized treatment.

In recent years, studies have shown the use of multimodality imaging (^{18}F-FDG PET/CT, DW-MRI, DCE-MRI) in HNSCC assessing both the association between the QIBs obtained from each imaging technique and their combined or respective roles in prognosis and/or prediction of outcome (10, 126-128). In this study for HPV- HNSCC patients, ADC as an established biomarker of treatment response was calculated by using DW-MRI. Non-linear mono-exponential fitting with three b-values was performed to estimate this metric. ^{18}F-FDG PET/CT also has a growing evidence base supporting its importance in therapy assessment; the well established SUV, which measures the glucose metabolic uptake, was obtained in HPV- HNSCC patients.

As mentioned in the introduction of this thesis, major technical challenges in IMRT persist in the use of functional images for RT, one of which includes the identification of a reproducible, radiotherapy-compatible patient position that is consistent between functional techniques and RT. All patients in the present study were in a supine position and fixed in place with the same immobilization system which was also used during the RT treatment planning and delivery. A thermoplastic mask, head support and flat table were used to try to minimize the distortion and to improve the registration process between the different imaging modalities.

The head support and flat table were adapted to MRI and PET/CT. This reproducible positioning addressed one of the big hurdles in the acquisition of multimodality images that may in the future be used for adaptive RT (85, 129).

Dirix et al. designed a prospective multimodality imaging study with this prerequisite in mind, recruiting 17 patients with primary HNSCC and performing ^{18}F-FDG, ^{18}F-FMISO, DW-MRI and DCE-MRI pre-, during, and post-Tx while taking into account the importance of patient positioning under which RT would take place for adaptive RT purposes. This study concluded that ^{18}F-FDG and ^{18}F-FMISO are valuable additions for treatment planning purposes and suggests the potential of DW-MRI and DCE-MRI for dose painting and response assessment (130). The INSIGHT study conducted by Welsh et al. and a study by Subesinghe et al. emphasized the importance of reproducing the positioning of patients using the same neck rest, shoulder rest and thermoplastic mask under which RT treatment planning and delivery would take place (131, 132).

This prospective study is the first in Spain, conducted from the point of view of advocating for the integration of functional imaging in RT treatment, which recruits a specific population of patients, HPV- HNSCC, analyzing ^{18}F-FDG, pre- and post-Tx, and DW-MRI pre- during and post-Tx in primary tumors and neck nodal metastases.

Previous studies have established that in HNSCC patients glucose metabolic uptake from ^{18}F-FDG is an effective tool for staging and therapy response assessment (58), and plays a fundamental role in adaptive RT (58, 133, 134). It is well known that ADC derived from DW-MRI is negatively correlated with tumor cell density (135), and furthermore is a useful biomarker to assess treatment response (11, 56). These two imaging techniques have been the focus of numerous studies in HNSCC to determine correlation, if any, between SUV and ADC values, with variable results. A study by Varoquax et al. involving 24 primary and 10 recurrent HNSCC tumors showed no significant correlation between SUV values (SUV_{max}, SUV_{mean} or SUV_{min}) and ADC values (ADC_{max}, ADC_{mean} or ADC_{min}), nor did Choi et al. find significance correlation between SUV_{mean} and ADC_{mean} in 47 primary HNSCC tumors (136, 137). Rather,

Nakajo et al. found significant negative correlation between SUV_{max} and ADC_{mean} in a study of 28 primary HNSCC tumors, and Nakamatsu et al. demonstrated significant negative correlation in 41 neck nodal metastases between SUV values (SUV_{max}, SUV_{mean}) and ADC values (ADC_{mean}, ADC_{min}) (138, 139). In the present study, a total of 11 neck nodal metastases and 5 primary HPV- HNSCC tumors showed a significant strong negative correlation, ADC_{mean} and SUV_{mean} pre-Tx (ρ=-0.67, p=0.01).

These discrepancies between studies can be related to non-standardized acquisition parameters. Another reason for this variability could be the variations among cohorts of patients. Preda et al. conclude in a study with 57 HNSCC primary tumors that "the combination of SUV_{max} and ADC_{min} improves the prognostic role of the two separate parameters" (140). The multimodal use of SUV and ADC have allowed this study to depict complex interactions between glucose metabolism and cellular density, making these biomarkers essential tools for adaptive RT purposes

IMRT has the ability to deliver a high dose to the tumor while minimizing side effects to surrounding healthy tissues (74). The high radiation dose delivered to the tumor induces a decrease in tumor cells, thus reducing restrictions on the mobility of water molecules at a microscopic level. Several studies have confirmed this "increased diffusion effect" as a marker of response to RT in HNSCC.

Vandecaveye et al. reported that ΔADC (3 weeks after CRT) for primary tumors with complete remission were significantly higher than for recurrent lesions (56). Again, Vandecaveye et al. showed in neck nodal metastases and primary tumors that ΔADC (2 Week and 4 Week during CRT) was significantly lower in lesions with recurrence than in lesions with a complete response (141).

The present study showed an increase in ΔADC_{2Week} for the patient with NED in comparison to the DOD and AWD patients in both primary tumor and neck nodal metastases, in agreement with above-mentioned studies. Also, the pre-Tx ADC value of the primary tumor

and neck nodal metastases for NED is lower than in the group of AWD and DOD, showing that lower pre-Tx ADC values are related to a good response to treatment and consistent with the literature (11, 142). ADC histograms showed microstructural heterogeneity in primary tumor and neck nodal metastases in the three groups (NED, AWD and DOD), as described in previous reports (143). The post-Tx ADC distribution curve illustrates the movement of water molecules in the extracellular space compared to pre-Tx. In the NED patient, a shift to higher ADC values for both primary tumor and neck nodal metastases reflects the improved pathologic response to RT. Furthermore, a wider range and higher pre-Tx ADC distribution can be seen in both primary tumor and neck nodal metastases for DOD and AWD patients, in comparison with the NED patient.

The ADC relative percent change trends shown for primary tumor and neck nodal metastases depict the different responses to treatment, suggesting the possibility of identifying at an early stage patients with a good or bad prognosis to individualize and adapt RT treatment (i.e. through dose-escalation or dose de-escalation).

Recent studies suggest that Wk-2 and Wk-3 of treatment are promising time points to identify different outcomes, although the appropriateness of using these time points to establish an accurate measurement of outcome needs to be validated in larger populations (144). This individualization of treatment is especially important in the subgroup of HPV- patients that was studied as a part of this thesis. Given that the outcomes for HPV tumors differ, HPV- patients have worse outcomes compared to HPV+ counterparts (145).

5.2. Part II: Novel application of the reversed gradient Diffusion Weighted MRI method for tumor response assessment in head and neck cancers (including the novel design of a Phantom Distortion Assessment) - *Experience at Meixoeiro University Hospital of Vigo, Spain*

In recent years, several approaches based on functional imaging have been proposed to predict tumor response, and many have been adapted for RT treatment. The main imaging techniques used so far are PET/CT (25, 146, 147), MRI (15, 148) or a combination of both (108, 149). In MRI, DW-MRI has shown promise in monitoring response to CRT in HNC (9, 123, 150).

For accurate measurement of ADC derived from DW-MRI, distortion must be minimized. In clinical practice, DW-MRI images often have lower image quality compared to other conventional MR images like T1w/T2w due to image quality issues such as distortion, noise, low resolution and the presence of artifacts, most of which arise due to the usage of faster image acquisition techniques such as EPI, essential for capturing the diffusion signal before it becomes null (16, 151). Because of its inherently low bandwidth per point in the phase encoding direction, EPI techniques exhibit more geometric distortion than spin warp MRI techniques. This problem must be addressed before assessing tumor response with DW-MRI and trying a voxel-wise analysis, because of the need to register the MRI images obtained during the treatment with planning CT scans, dose distributions, or PET/CT scans. Fortunately, the geometric distortion can be reduced by using the reversed gradient method (91, 92) and other artifacts (like eddy currents) can be corrected by a serial of different b-values and simultaneous image segmentation and iterative registration (152). There is also an interesting alternative to the reversed gradient method called the "phase labeling for additional coordinate encoding" (PLACE) technique (153). This method consists of a slightly modified additional EPI acquisition; they sample the k-t space with a shift in k_y by adding a small area to the phase-encoding gradient. As distortion is the main disadvantage of using DW-MRI for tumor response assessment, the reversed gradient method was used for the purposes of this thesis to reduce geometric distortion and improve accuracy of ADC derived from DW-MRI.

The reversed gradient method has not been used in previous studies that show ADC variation with radiation dose (15, 108, 148). Geometric accuracy is crucial when using functional imaging in RT. The DW-MRI images corrected by the reversed gradient method also point out the feasibility of the voxel-wise approach to tumor response assessment using ADC and establish its clinical utility as an imaging biomarker of response.

Several phantoms have been developed for DW-MRI assessment but they are more focused on verifying ADC values than on evaluating distortion (154, 155). In the present study, a new phantom was specifically designed to evaluate geometrical distortion. The reversed gradient method was applied to both phantom images and DW-MRI images obtained from a patient included in the ARTFIBio project (108). The DW-MRI images were registered to T2w images of the phantom and the patient. The evaluation for mutual information on DW-MRI images was done with and without the reversed gradient method. The mutual information was used as a measure of goodness for the distortion correction. This is a widely used metric to evaluate a registration method for images obtained from different modalities (102). The reversed gradient method does not modify the calculated ADC value in the phantom while it helps to provide accurate ADC measurement in tumors as a result of better registration during RT.

This study is the first in Spain to be conducted from the point of view of advocating for an accurate measurement of ADC derived from DW-MRI in HPV- HNSCC patients, relying on the correction of geometrical distortion in DW-MRI using the reversed gradient method.

The visual improvement in the registration with the reversed gradient method applied was observed to show a better fit to the real anatomic position indicated in the CT. The numerical quantification of distortion calculated through the mutual information metric in undistorted DW-MRI images for both phantom and patients with different b-values, showed an improvement in the mutual information metric with respect to distorted images.

The values of ADC obtained after the correction agreed with the original values for the same volume. Considering this and the visual improvement in the registration process, the

reduced distortion obtained through mutual metric information, and the accurate measure of ADC, correcting the distortion with the reversed gradient method is suggested before implementing an imaging method of treatment response that uses ADC maps for assessing tumor response or tumor cell density variation.

5.3. Part III: Intra Voxel Incoherent Motion Diffusion Weighted MRI and Dynamic Contrast Enhanced MRI methods for tumor response assessment in Brain Metastases

- Experience at Memorial Sloan-Kettering Cancer Center, USA

This part of the discussion is divided into two sections framed as an experience at Memorial Sloan-Kettering Cancer Center (MSKCC) in the USA. The first section is related to the role of the Phantom study as a key part in the use of QIB. The second section is related to the evaluation of whether quantitative imaging metrics derived from IVIM DW- and DCE- MRI can assess early (1-72 hours post-Tx) treatment response in patients with BM treated with SRS.

5.3.1. Repeatability and Reproducibility of Quantitative Imaging Biomarkers: Diffusion Weighted MRI as a test model

For QIBs to be used in adaptative RT, it is a prerequisite to perform exhaustive phantom studies detailing the repeatability and reproducibility of the functional imaging technique. This study plays a key part in the use of QIB at MSKCC from the point of view of advocating for standardizing data acquisition conditions across vendors and using a temperature-controlled fluid phantom with a specific procedure to minimize the bias in ADC measurements in DWI studies, assessing repeatability and reproducibility.

The RT process is complex and involves many areas of knowledge. Among them, radiation treatment planning and dosimetry needs quality control and quality assurance (QA) to avoid errors and to give high confidence that patients will receive the prescribed treatment correctly. In addition, clinical trial QA plays a significant role in enhancing the quality of care.

To implement functional imaging in adaptive RT, the measurements obtained from the clinical situation being investigated must be in the range of the fluctuations of repeatability tests. The coefficient of variation is often used in repeatability studies to assess these fluctuations. In addition, maximization of tumor visualization and char-

acterization is required. Both DW-MRI and the ADC maps should be evaluated with corresponding morphologic images. The suppression of background normal tissue signals, however, is desirable. This suppression of background signals can be achieved by performing DW-MRI with sufficient degrees of diffusion weighted. The signal intensity in b-value DW-MRI images generally obtained from tumor yields low ADC. In contrast, cystic or necrotic tissues show greater signal attenuation on high b-value images and have high ADC values, exhibiting the same behavior as some normal and pathologic tissues. The customization of DW-MRI protocols specific to different tumor types, tumor locations, anatomic region, tissue composition, and pathologic processes need to be established for multimodality imaging studies which will use functional imaging for adaptive RT.

ADC values acquired for the phantom from different vendors showed no statistical difference between the 4 measurements performed within and across vendors and between different ROIs drawn. In addition a low coefficient of variation of the repeatability measurements for each vendor was shown in the study.

This study assessed the repeatability, reproducibility and quantitative quality control of ADC measurements across vendors of the same field strength using a standardized acquisition protocol. Using a temperature-controlled fluid phantom constructed by Chenevert et al., a specific procedure, and standardized data acquisition conditions across vendors, this study explores the need for systematic reproducibility for DW-MRI studies (95).

5.3.2. Intra Voxel Incoherent Motion Diffusion Weighted MRI and Dynamic Contrast Enhanced MRI methods for tumor response assessment in Brain Metastases - *Experience at Memorial Sloan-Kettering Cancer Center, USA*

BM are the most common intracranial tumors in adults. Furthermore, they represent an important cause of mortality (83). Measurements of annual BM incidence point towards an increase in incidence over the past several years, which has been attributed to several factors such as the improved ability of imaging modalities, an aging population, and better treatment of systemic disease.

Both in the clinical and research settings it is essential to accurately assess whether or not a BM has been successfully treated and whether the metastasis requires additional treatment. The accurate assessment of treatment response by RT in BM is challenging because in some cases treated metastases can increase in size soon after therapy (156). Moreover, this increase in size happens in successfully treated metastases even in long term follow up assessment; in fact, Patel et al. found that one third of treated metastases have transient increases in size (156). Radiation necrosis or pseudo-progression due to radiation can be challenging to differentiate from tumor recurrence by standard MRI (68). Obviously, in order to make the appropriate clinical decisions regarding further therapy, which may include additional RT, it is essential to differentiate between these two eventualities. Clearly, a method that can accurately predict response soon after the completion of therapy would be advantageous over a method that requires long term clinical follow up. Hence, it is essential to develop noninvasive methods that will be able to determine if a metastasis has been successfully treated.

In terms of treatment options, SRS has emerged as one of the most important for the management of these tumors (157). Because dose delivery is accurate to within one to two millimeters in SRS, the procedure is capable of delivering maximum dose within a target while minimizing the exposure of healthy surrounding tissue to ionizing radiation. To achieve this level of precision, SRS relies on 3-D imaging techniques such

as CT, MRI, and PET/CT to determine a tumor's exact size, shape, and location within the patient, immobilization systems to ensure proper patient positioning and fixation throughout the therapy, highly focused gamma-ray or x-ray beams, and IGRT to confirm a tumor's location before and sometimes during treatment. Despite these factors, which point to the relevance of BM and its treatment by SRS in radiation oncology, prospective studies in SRS treatment involving patients with BM are limited.

The scarcity of studies conducted in this area attest to a general dearth of information and the need for further research. Jakubovic et al. studied, in 42 patients treated either WBRT or SRS, the potential of ADC as a treatment response biomarker, performing DW-MRI pre-, 1 week and 1 month post-treatment (158). They found that lower relative ADC values at 1 week and 1 month following radiation distinguished responders from non-responders. Earlier, Jakubovic et al. had also conducted a study of 70 BM treated either with WBRT or SRS, to investigate the predictive ability of perfusion biomarkers from Dynamic susceptibility (DSC) to treatment response, performing DSC pre-, 1 week and 1 month post-treatment. They demonstrated that lower perfusion values can indentify responders and progressive disease patients (159). Huber et al. studied local control and local failure by assessing contrast-enhancing volumes on T1w images in 87 BM at 3 weeks and every 3 months post- SRS (70). The results suggested that volume on T1w images after SRS is a sensitive predictor of local failure.

The literature for the assessment of BM with MRI after SRS is sparse and even scarcer for advanced quantitative imaging (64, 70-73). Furthermore, there are no studies that assess response after SRS within 1-72 hours.

This study calculated the diffusion related parameters as follows: ADC by using DW-MRI; and the true diffusion coefficient (D) and the perfusion factor (f) in BM by using IVIM DW-MRI, which was estimated by a bi-exponential fitting with multiple b-values. Meanwhile, DCE-MRI was analyzed by using the standard model approach. The perfusion biomarkers estimated provided information of the leakage rate of CA to

the extracellular space through K^{trans}, vascularity information through v_p and extracellular space information through v_e. The QIBs derived from DCE-MRI are complicated to estimate, and are still a challenge. Their sensitivity can be influenced by different acquisition methods, processing techniques, and AIF estimation methods, all of which can affect reproducibility. When using standardized imaging protocols, changes in these DCE-MRI biomarkers are able to predict response or monitor the effects of RT treatments.

This prospective study is the first of its kind to evaluate whether quantitative imaging metrics derived from IVIM DW- and DCE- MRI can assess early (1-72 hours post-Tx) treatment response in patients with BM treated with SRS. The results generated from this initial study are a building block for future studies with larger patient populations and have an application in adaptive RT in cancer.

The present study showed a significant strong positive correlation between mean ADC and mean D, mean f and mean v_p and K^{trans}, mean K^{trans} and mean v_e. ADC's inverse correlation with cellularity is well-known, as tumors that grow at a high proliferation rate and have high cell density present lower ADC values (135). This characteristic of ADC, taken together with the increase in immature tumoral vessels that tends to be associated with the high proliferation of microvasculature, suggests a possible justification for these correlations (160, 161).

The concept of assessing early response within 1-72 hours in BM patients treated with SRS is novel and showed substantial changes in the relative percent changes of the imaging metrics. As much remains unexplained in the clinical realm in this setting, some studies attempt to understand tumor response to RT in preclinical settings. Garcia-Barros et al. investigated the hypothesis that tumor response to radiation is determined not only by tumor cell phenotype but also by microvascular sensitivity in a preclinical study. MCA/129 fibrosarcomas and B16F1 melanomas grown in apoptosis-resistant acid sphingomyelinase (asmase)-deficient or Bax-deficient mice displayed markedly reduced

baseline microvascular endothelial apoptosis and grew 200 to 400% faster than tumors on wild-type microvasculature, indicating that endothelial apoptosis was a homeostatic factor regulating angiogenesis-dependent tumor growth. Moreover, these tumors exhibited reduced endothelial apoptosis upon irradiation. This study showed that microvascular damage regulates tumor cell response to radiation at the clinically relevant dose range (162). In a study that implanted human brain tumors in rats, Brown et al. showed that K^{trans} decreases 24 hours post-SRS due to a reduce in blood flow supply (163). In addition, Song et al. showed that high-dose radiation causes prolonged ischemia that leads to additional cell killing (164). In a pre-clinical study conducted by Horsman et al. in mammary carcinoma, they showed a decrease in the Gd-uptake after 48 hours of a single dose radiation of 20 Gy (165).

In the present study, ADC, D and K^{trans} histograms display microstructural and microvasculature heterogeneity in tumor tissue and are consistent with previous reports (143). The early post-Tx ADC and K^{trans} distribution curves illustrate the distribution of water molecules and contrast agent in the extracellular space compared to pre-Tx. A shift towards a higher ADC and lower K^{trans} values reflect the improved pathologic response to SRS. The results in terms of response to treatment in a long term follow up of 12 months show the same behavior of the tumor in terms of both the ADC values and tumor volumes for three representative patients.

In this thesis it is shown that early changes in diffusion and perfusion imaging metrics to SRS can be detected in a manner similar to the changes seen by radiation effects in other studies. These exploratory results need in-depth study at both the preclinical and clinical levels to decipher the actual biology that triggers the changes seen in the quantitative imaging metrics in RT setting.

Chapter VI

Chapter VI: Conclusions and future work

This Ph.D. thesis is framed in the context of the modern advancement of RT towards individualized medicine. The use of imaging techniques such as CT, MRI and PET/CT have been established in the clinical flow to adapt RT treatment to the patient based on the anatomical information of the tumor provided by these techniques. The anatomical localization of the tumor plays a fundamental role in the application of RT treatment; this localization must be precise and reproducible for purposes of treatment planning and RT delivery. Among other methods that can ensure a high level of precision and reproducibility, the use of immobilization systems and flat tables has been routinely standardized. Functional information obtained from PET/CT is helping to complement this anatomical localization through even greater enhancements to precision, demonstrating the relevance of the need for new tools in RT. The metabolism, diffusion and perfusion of the tumor measured through PET/CT and MRI, and the derived QIBs show different behaviors based on the specific type of tumor. In addition, these biomarkers show promise as predictors of prognosis and tumor response assessment, giving also microstructural and microvasculature information of tumors. This potential has been explored and examined in the studies below, with implications for the application and further study of functional imaging and QIBs in adaptive RT.

Part I of this thesis focuses on a population of HPV- HNSCC patients. The analysis of derived biomarkers (ADC and SUV) pre-, during and post-Tx, using the same immobilization devices in the acquisition of MRI and PET/CT data as in RT, showed that tumor cell density is inversely proportional to glucose metabolism of tumor. Furthermore, the survival status and functional biomarkers showed different trends for NED, AWD and DOD patients. A possibility to explore in the future is the optimization of the acquisition time to minimize the time in which the patient is fitted with a fixation mask. In addition, the specific disease type selected made recruitment highly selective; however, this selectivity is justified given that these subtypes of HPV- patients are the ones who have poor prognoses in HNSCC.

The results represent patterns in just three clinical outcome categories (NED, AWD and DOD) to show what features and what conditions are necessary to assess tumor response in this subtype of patients. In addition, this study offers insight into how to manage and understand valuable biomarkers, such as SUV and ADC, with the objective of integrating them into the development of adaptive RT in the future.

The need for the accurate localization of tumor for treatment planning and RT delivery was the focus of Part II of this thesis. Distortion in DW-MRI must therefore be minimized, an issue that this study attempted to resolve through the application of the reversed gradient method to DW-MRI to obtain a more accurate measurement of ADC. A clear improvement in mutual information for registration processes was observed when the reversed gradient method was applied. Thus, this method improves both registration and provides accurate ADC measurement in tumors. The correction of distortion with the reversed gradient method should form part of an imaging method for treatment response using ADC metrics to assess tumor response or cell density variation with treatment in cancer patients.

Part III of the thesis focused on BM patients treated with SRS, analyzing diffusion and perfusion from DW-MRI and DCE-MRI pre- and early post-Tx to show early changes in diffusion and perfusion imaging metrics due to SRS treatment. These changes can be detected in a manner similar to those associated with radiation effect in other studies. BM patient studies are still lacking, and the method proposed in this thesis is the first of its kind used to predict response at the early stages. This method is advantageous to others requiring long term clinical follow up, and will help to individualize and adapt RT treatment.

These results should be validated in larger populations and through multicenter studies in order to apply these biomarkers in the clinical setting of adaptive RT for HPV- HNSCC and BM. For this application to occur, ensuring reproducibility and repeatability is crucial. A particular procedure and standard data acquisition conditions for the systematic reproducibility of QIBs was tested in DW-MRI. A possibility to explore in the future is to further extend the specific procedure studied to DCE-MRI and IVIM DW-MRI. The new development of phantoms,

in collaboration with QIBA, presents an opportunity to do so. In addition, the development of new guidelines will provide a useful basis for the reproducibility and repeatability of selected QIBs.

The three studies that constitute this thesis are an attempt to deepen our understanding of how to manage and use valuable information derived from the above mentioned functional imaging modalities in RT setting for cancer patients. After all, multimodality functional imaging offers much more information about tumor biology and metabolism than the individual datasets on their own and can be used as good predictors of treatment response with the possibility of implementing them in future adaptive RT.

Bibliography

Bibliography

1. Beyzadeoglu M, Ozyigit G, Ebruli C. Basic radiation oncology. Heidelberg: Springer; 2010. xxiii, 575 p. p.

2. Padhani AR, Liu G, Koh DM, Chenevert TL, Thoeny HC, Takahara T, et al. Diffusion-weighted magnetic resonance imaging as a cancer biomarker: consensus and recommendations. Neoplasia. 2009;11(2):102-25.

3. Ell PJ. The contribution of PET/CT to improved patient management. The British journal of radiology. 2006;79(937):32-6.

4. Grau C, Hoyer M, Alber M, Overgaard J, Lindegaard JC, Muren LP. Biology-guided adaptive radiotherapy (BiGART)--more than a vision? Acta oncologica. 2013;52(7):1243-7.

5. Ling CC, Humm J, Larson S, Amols H, Fuks Z, Leibel S, et al. Towards multidimensional radiotherapy (MD-CRT): Biological imaging and biological conformality. Int J Radiat Oncol. 2000;47(3):551-60.

6. Nishimura Y, Komaki R. Intensity-modulated radiation therapy : clinical evidence and techniques2015. 473 p.

7. Mac Manus MP, Everitt S, Bayne M, Ball D, Plumridge N, Binns D, et al. The use of fused PET/CT images for patient selection and radical radiotherapy target volume definition in patients with non-small cell lung cancer: Results of a prospective study with mature survival data. Radiother Oncol. 2013;106(3):292-8.

8. Lagendijk JJW, Raaymakers BW, Van den Berg CAT, Moerland MA, Philippens ME, van Vulpen M. MR guidance in radiotherapy. Phys Med Biol. 2014;59(21):R349-R69.

9. Vandecaveye V, De Keyzer F, Nuyts S, Deraedt K, Dirix P, Hamaekers P, et al. Detection of head and neck squamous cell carcinoma with diffusion weighted MRI after (chemo) radiotherapy: Correlation between radiologic and histopathologic findings. Int J Radiat Oncol. 2007;67(4):960-71.

10. Shukla-Dave A, Lee NY, Jansen JF, Thaler HT, Stambuk HE, Fury MG, et al. Dynamic contrast-enhanced magnetic resonance imaging as a predictor of outcome in head-and-neck squamous cell carcinoma patients with nodal metastases. International journal of radiation oncology, biology, physics. 2012;82(5):1837-44.

11. Kim S, Loevner L, Quon H, Sherman E, Weinstein G, Kilger A, et al. Diffusion-weighted magnetic resonance imaging for predicting and detecting early response to chemoradiation therapy of squamous cell carcinomas of the head and neck. Clinical cancer research : an official journal of the American Association for Cancer Research. 2009;15(3):986-94.

12. Driessen JP, Caldas-Magalhaes J, Janssen LM, Pameijer FA, Kooij N, Terhaard CH, et al. Diffusion-weighted MR imaging in laryngeal and hypopharyngeal carcinoma: association between apparent diffusion coefficient and histologic findings. Radiology. 2014;272(2):456-63.

13. Hamstra DA, Chenevert TL, Moffat BA, Johnson TD, Meyer CR, Mukherji SK, et al. Evaluation of the functional diffusion map as an early biomarker of time-to-progression and overall survival in high-grade glioma. P Natl Acad Sci USA. 2005;102(46):16759-64.

14. Galban CJ, Mukherji SK, Chenevert TL, Meyer CR, Hamstra DA, Bland PH, et al. A Feasibility Study of Parametric Response Map Analysis of Diffusion-Weighted Magnetic Resonance Imaging Scans of Head and Neck Cancer Patients for Providing Early Detection of Therapeutic Efficacy. Transl Oncol. 2009;2(3):184-90.

15. Atuegwu NC, Gore JC, Yankeelov TE. The integration of quantitative multi-modality imaging data into mathematical models of tumors. Phys Med Biol. 2010;55(9):2429-49.

16. Perez Romasanta LA, Garcia Velloso MJ, Lopez Medina A. Functional imaging in radiation therapy planning for head and neck cancer. Reports of practical oncology and radiotherapy : journal of Greatpoland Cancer Center in Poznan and Polish Society of Radiation Oncology. 2013;18(6):376-82.

17. Farjam R, Tsien CI, Lawrence TS, Cao Y. DCE-MRI defined subvolumes of a brain metastatic lesion by principle component analysis and fuzzy-c-means clustering for response assessment of radiation therapy. Medical physics. 2014;41(1):011708.

18. Intven M, Reerink O, Philippens ME. Dynamic contrast enhanced MR imaging for rectal cancer response assessment after neo-adjuvant chemoradiation. Journal of magnetic resonance imaging : JMRI. 2015;41(6):1646-53.

19. Ido T, Wan CN, Casella V, Fowler JS, Wolf AP, Reivich M, et al. Labeled 2-Deoxy-D-Glucose Analogs - F-18-Labeled 2-Deoxy-2-Fluoro-D-Glucose, 2-Deoxy-2-Fluoro-D-Mannose and C-14-2-Deoxy-2-Fluoro-D-Glucose. J Labelled Compd Rad. 1978;14(2):175-83.

20. Roe K, Aleksandersen TB, Kristian A, Nilsen LB, Seierstad T, Qu H, et al. Preclinical dynamic 18F-FDG PET - tumor characterization and radiotherapy response assessment by kinetic compartment analysis. Acta oncologica. 2010;49(7):914-21.

21. Gregoire V, Haustermans K, Geets X, Roels S, Lonneux M. PET-based treatment planning in radiotherapy: A new standard? J Nucl Med. 2007;48:68s-77s.

22. Mak D, Corry J, Lau E, Rischin D, Hicks RJ. Role of FDG-PET/CT in staging and follow-up of head and neck squamous cell carcinoma. Q J Nucl Med Mol Im. 2011;55(5):487-99.

23. van Elmpt W, De Ruysscher D, van der Salm A, Lakeman A, van der Stoep J, Emans D, et al. The PET-boost randomised phase II dose-escalation trial in non-small cell lung cancer. Radiother Oncol. 2012;104(1):67-71.

24. Heukelom J, Hamming O, Bartelink H, Hoebers F, Giralt J, Herlestam T, et al. Adaptive and innovative Radiation Treatment FOR improving Cancer treatment outcomE (ART-FORCE); a randomized controlled phase II trial for individualized treatment of head and neck cancer. BMC cancer. 2013;13:84.

25. Toma-Dasu I, Uhrdin J, Antonovic L, Dasu A, Nuyts S, Dirix P, et al. Dose prescription and treatment planning based on FMISO-PET hypoxia. Acta oncologica. 2012;51(2):222-30.

26. Tatum JL, Kelloff GJ, Gillies RJ, Arbeit JM, Brown JM, Chao KS, et al. Hypoxia: importance in tumor biology, noninvasive measurement by imaging, and value of its measurement in the management of cancer therapy. International journal of radiation biology. 2006;82(10):699-757.

27. Padhani AR, Krohn KA, Lewis JS, Alber M. Imaging oxygenation of human tumours. European radiology. 2007;17(4):861-72.

28. Troost EG, Laverman P, Kaanders JH, Philippens M, Lok J, Oyen WJ, et al. Imaging hypoxia after oxygenation-modification: comparing [18F]FMISO autoradiography with pimonidazole immunohistochemistry in human xenograft tumors. Radiother Oncol. 2006;80(2):157-64.

29. Peeters SG, Zegers CM, Lieuwes NG, van Elmpt W, Eriksson J, van Dongen GA, et al. A comparative study of the hypoxia PET tracers [(1)(8)F]HX4, [(1)(8)F]FAZA, and [(1)(8)F]FMISO in a preclinical tumor model. International journal of radiation oncology, biology, physics. 2015;91(2):351-9.

30. Piert M, Machulla HJ, Picchio M, Reischl G, Ziegler S, Kumar P, et al. Hypoxia-specific tumor imaging with 18F-fluoroazomycin arabinoside. J Nucl Med. 2005;46(1):106-13.

31. Duprez F, De Neve W, De Gersem W, Coghe M, Madani I. Adaptive dose painting by numbers for head-and-neck cancer. International journal of radiation oncology, biology, physics. 2011;80(4):1045-55.

32. Madani I, Duprez F, Boterberg T, Van de Wiele C, Bonte K, Deron P, et al. Maximum tolerated dose in a phase I trial on adaptive dose painting by numbers for head and neck cancer. Radiother Oncol. 2011;101(3):351-5.

33. Smit K, van Asselen B, Kok JG, Aalbers AH, Lagendijk JJ, Raaymakers BW. Towards reference dosimetry for the MR-linac: magnetic field correction of the ionization chamber reading. Phys Med Biol. 2013;58(17):5945-57.

34. Saenz DL, Paliwal BR, Bayouth JE. A dose homogeneity and conformity evaluation between ViewRay and pinnacle-based linear accelerator IMRT treatment plans. Journal of medical physics / Association of Medical Physicists of India. 2014;39(2):64-70.

35. Sullivan DC, Obuchowski NA, Kessler LG, Raunig DL, Gatsonis C, Huang EP, et al. Metrology Standards for Quantitative Imaging Biomarkers. Radiology. 2015;277(3):813-25.

36. Kessler LG, Barnhart HX, Buckler AJ, Choudhury KR, Kondratovich MV, Toledano A, et al. The emerging science of quantitative imaging biomarkers terminology and definitions for scientific studies and regulatory submissions. Statistical methods in medical research. 2015;24(1):9-26.

37. Biomarkers Definitions Working G. Biomarkers and surrogate endpoints: preferred definitions and conceptual framework. Clinical pharmacology and therapeutics. 2001;69(3):89-95.

38. Tofts P. Quantitative MRI of the Brain Measuring Changes Caused by Disease Introduction. Quantitative Mri of the Brain: Measuring Changes Caused by Disease. 2003:Xv-Xvi.

39. Chenevert TL, Ross BD. Diffusion imaging for therapy response assessment of brain tumor. Neuroimaging clinics of North America. 2009;19(4):559-71.

40. Padhani AR, Khan AA. Diffusion-weighted (DW) and dynamic contrast-enhanced (DCE) magnetic resonance imaging (MRI) for monitoring anticancer therapy. Targeted oncology. 2010;5(1):39-52.

41. Stejskal EO, Tanner JE. Spin Diffusion Measurements: Spin Echoes in the Presence of a Time-Dependent Field Gradient. J Chem Phys. 1965;42(1):288-+.

42. Le Bihan D, Breton E, Lallemand D, Grenier P, Cabanis E, Laval-Jeantet M. MR imaging of intravoxel incoherent motions: application to diffusion and perfusion in neurologic disorders. Radiology. 1986;161(2):401-7.

43. Bammer R. Basic principles of diffusion-weighted imaging. European journal of radiology. 2003;45(3):169-84.

44. Filippi M, Horsfield MA, Tofts PS, Barkhof F, Thompson AJ, Miller DH. Quantitative assessment of MRI lesion load in monitoring the evolution of multiple sclerosis. Brain. 1995;118:1601-12.

45. Tofts PS, Brix G, Buckley DL, Evelhoch JL, Henderson E, Knopp M, et al. Estimating kinetic parameters from dynamic contrast-enhanced T(1)-weighted MRI of a diffusable tracer: Standardized quantities and symbols. Journal of Magnetic Resonance Imaging. 1999;10(3):223-32.

46. Crone C. The Permeability of Capillaries in Various Organs as Determined by Use of the 'Indicator Diffusion' Method. Acta physiologica Scandinavica. 1963;58:292-305.

47. Kim EE. Clinical PET and PET/CT : principles and applications. 2nd ed. New York: Springer; 2013. xix, 398 p. p.

48. Kapoor V, McCook BM, Torok FS. An introduction to PET-CT imaging. Radiographics : a review publication of the Radiological Society of North America, Inc. 2004;24(2):523-43.

49. Fletcher JW, Djulbegovic B, Soares HP, Siegel BA, Lowe VJ, Lyman GH, et al. Recommendations on the use of 18F-FDG PET in oncology. J Nucl Med. 2008;49(3):480-508.

50. positronpharma. Available from: http://positronpharma.com/dt_portfolio/18ffdg/.

51. . Available from: http://journal.frontiersin.org/article/10.3389/fonc.2013.00208/full

52. Ben-Haim S, Ell P. 18F-FDG PET and PET/CT in the evaluation of cancer treatment response. J Nucl Med. 2009;50(1):88-99.

53. Forastiere AA, Goepfert H, Maor M, Pajak TF, Weber R, Morrison W, et al. Concurrent chemotherapy and radiotherapy for organ preservation in advanced laryngeal cancer. The New England journal of medicine. 2003;349(22):2091-8.

54. Chawla S, Kim S, Dougherty L, Wang S, Loevner LA, Quon H, et al. Pretreatment diffusion-weighted and dynamic contrast-enhanced MRI for prediction of local treatment response in squamous cell carcinomas of the head and neck. AJR American journal of roentgenology. 2013;200(1):35-43.

55. Hauser T, Essig M, Jensen A, Laun FB, Munter M, Maier-Hein KH, et al. Prediction of treatment response in head and neck carcinomas using IVIM-DWI: Evaluation of lymph node metastasis. European journal of radiology. 2014;83(5):783-7.

56. Vandecaveye V, Dirix P, De Keyzer F, Op de Beeck K, Vander Poorten V, Hauben E, et al. Diffusion-weighted magnetic resonance imaging early after chemoradiotherapy to monitor treatment response in head-and-neck squamous cell carcinoma. International journal of radiation oncology, biology, physics. 2012;82(3):1098-107.

57. Brizel DM, Sibley GS, Prosnitz LR, Scher RL, Dewhirst MW. Tumor hypoxia adversely affects the prognosis of carcinoma of the head and neck. International journal of radiation oncology, biology, physics. 1997;38(2):285-9.

58. Schoder H, Fury M, Lee N, Kraus D. PET monitoring of therapy response in head and neck squamous cell carcinoma. J Nucl Med. 2009;50 Suppl 1:74S-88S.

59. Ong SC, Schoder H, Lee NY, Patel SG, Carlson D, Fury M, et al. Clinical utility of 18F-FDG PET/CT in assessing the neck after concurrent chemoradiotherapy for Locoregional advanced head and neck cancer. J Nucl Med. 2008;49(4):532-40.

60. Wong RJ, Lin DT, Schoder H, Patel SG, Gonen M, Wolden S, et al. Diagnostic and prognostic value of [(18)F]fluorodeoxyglucose positron emission tomography for recurrent head and neck squamous cell carcinoma. Journal of clinical oncology : official journal of the American Society of Clinical Oncology. 2002;20(20):4199-208.

61. Schwartz DL, Rajendran J, Yueh B, Coltrera MD, Leblanc M, Eary J, et al. FDG-PET prediction of head and neck squamous cell cancer outcomes. Archives of otolaryngology--head & neck surgery. 2004;130(12):1361-7.

62. Muller-Riemenschneider F, Bockelbrink A, Ernst I, Schwarzbach C, Vauth C, von der Schulenburg JM, et al. Stereotactic radiosurgery for the treatment of brain metastases. Radiother Oncol. 2009;91(1):67-74.

63. Soffietti R, Ruda R, Trevisan E. Brain metastases: current management and new developments. Current opinion in oncology. 2008;20(6):676-84.

64. Hawighorst H, Essig M, Debus J, Knopp MV, Engenhart-Cabilic R, Schonberg SO, et al. Serial MR imaging of intracranial metastases after radiosurgery. Magnetic resonance imaging. 1997;15(10):1121-32.

65. Pan HC, Sheehan J, Stroila M, Steiner M, Steiner L. Gamma knife surgery for brain metastases from lung cancer. J Neurosurg. 2005;102 Suppl:128-33.

66. Kondziolka D, Martin JJ, Flickinger JC, Friedland DM, Brufsky AM, Baar J, et al. Long-term survivors after gamma knife radiosurgery for brain metastases. Cancer. 2005;104(12):2784-91.

67. Sheehan JP, Sun MH, Kondziolka D, Flickinger J, Lunsford LD. Radiosurgery in patients with renal cell carcinoma metastasis to the brain: long-term outcomes and prognostic factors influencing survival and local tumor control. J Neurosurg. 2003;98(2):342-9.

68. Dequesada IM, Quisling RG, Yachnis A, Friedman WA. Can Standard Magnetic Resonance Imaging Reliably Distinguish Recurrent Tumor from Radiation Necrosis after

Radiosurgery for Brain Metastases? A Radiographic-Pathological Study. Neurosurgery. 2008;63(5):898-903.

69. Kimura T, Sako K, Tanaka K, Gotoh T, Yoshida H, Aburano T, et al. Evaluation of the response of metastatic brain tumors to stereotactic radiosurgery by proton magnetic resonance spectroscopy, (TICI)-T-201 single-photon emission computerized tomography, and gadolinium-enhanced magnetic resonance imaging. J Neurosurg. 2004;100(5):835-41.

70. Huber PE, Hawighorst H, Fuss M, van Kaick G, Wannenmacher MF, Debus J. Transient enlargement of contrast uptake on MRI after linear accelerator (linac) stereotactic radiosurgery for brain metastases. International journal of radiation oncology, biology, physics. 2001;49(5):1339-49.

71. Peterson AM, Meltzer CC, Evanson EJ, Flickinger JC, Kondziolka D. MR imaging response of brain metastases after gamma knife stereotactic radiosurgery. Radiology. 1999;211(3):807-14.

72. Almeida-Freitas DB, Pinho MC, Otaduy MCG, Braga HF, Meira-Freitas D, Leite CD. Assessment of irradiated brain metastases using dynamic contrast-enhanced magnetic resonance imaging. Neuroradiology. 2014;56(6):437-43.

73. Farjam R, Tsien CI, Feng FY, Gomez-Hassan D, Hayman JA, Lawrence TS, et al. Investigation of the diffusion abnormality index as a new imaging biomarker for early assessment of brain tumor response to radiation therapy. Neuro-oncology. 2014;16(1):131-9.

74. Nishimura Y, Komaki R. Intensity-modulated radiation therapy : clinical evidence and techniques. viii, 473 pages p.

75. Galceran. Estimaciones de la incidencia y la supervivencia del cáncer en España y su situación en Europa 2014.

76. Sanderson RJ, Ironside JAD. Squamous cell carcinomas of the head and neck. Brit Med J. 2002;325(7368):822-7.

77. Seijas-Tamayo R, Fernandez-Mateos J, Adansa Klain JC, Mesia R, Pastor Borgonon M, Perez-Ruiz E, et al. Epidemiological characteristics of a Spanish cohort of patients diagnosed with squamous cell carcinoma of head and neck: distribution of risk factors by tumor location. Clinical & translational oncology : official publication of the Federation of Spanish Oncology Societies and of the National Cancer Institute of Mexico. 2016.

78. Fakhry C, Westra WH, Li S, Cmelak A, Ridge JA, Pinto H, et al. Improved survival of patients with human papillomavirus-positive head and neck squamous cell carcinoma in a prospective clinical trial. Journal of the National Cancer Institute. 2008;100(4):261-9.

79. Davis FG, Dolecek TA, McCarthy BJ, Villano JL. Toward determining the lifetime occurrence of metastatic brain tumors estimated from 2007 United States cancer incidence data. Neuro-oncology. 2012;14(9):1171-7.

80. Wen PY, Loeffler JS. Management of brain metastases. Oncology. 1999;13(7):941-54, 57-61; discussion 61-2, 9.

81. Delattre JY, Krol G, Thaler HT, Posner JB. Distribution of brain metastases. Archives of neurology. 1988;45(7):741-4.

82. Society AC. American Cancer Society. Cancer Facts & Figures. Atlanta, GA: 2007.

83. Khuntia D, Brown P, Li J, Mehta MP. Whole-brain radiotherapy in the management of brain metastasis. Journal of clinical oncology : official journal of the American Society of Clinical Oncology. 2006;24(8):1295-304.

84. Mera Iglesias M, Aramburu Nunez D, Del Olmo Claudio JL, Lopez Medina A, Landesa-Vazquez I, Salvador Gomez F, et al. Multimodality functional imaging in radiation therapy planning: relationships between dynamic contrast-enhanced MRI, diffusion-weighted MRI, and 18F-FDG PET. Comput Math Methods Med. 2015;2015:103843.

85. van der Heide UA, Houweling AC, Groenendaal G, Beets-Tan RG, Lambin P. Functional MRI for radiotherapy dose painting. Magnetic resonance imaging. 2012;30(9):1216-23.

86. Leibfarth S, Monnich D, Welz S, Siegel C, Schwenzer N, Schmidt H, et al. A strategy for multimodal deformable image registration to integrate PET/MR into radiotherapy treatment planning. Acta oncologica. 2013;52(7):1353-9.

87. Fortunati V, Verhaart RF, Angeloni F, van der Lugt A, Niessen WJ, Veenland JF, et al. Feasibility of Multimodal Deformable Registration for Head and Neck Tumor Treatment Planning. Int J Radiat Oncol. 2014;90(1):85-93.

88. Jezzard P, Clare S. Sources of distortion in functional MRI data. Human brain mapping. 1999;8(2-3):80-5.

89. Holland D, Kuperman JM, Dale AM. Efficient correction of inhomogeneous static magnetic field-induced distortion in Echo Planar Imaging. Neuroimage. 2010;50(1):175-83.

90. Reinsberg SA, Doran SJ, Charles-Edwards EM, Leach MO. A complete distortion correction for MR images: II. Rectification of static-field inhomogeneities by similarity-based profile mapping. Phys Med Biol. 2005;50(11):2651-61.

91. Chang H, Fitzpatrick JM. A technique for accurate magnetic resonance imaging in the presence of field inhomogeneities. IEEE transactions on medical imaging. 1992;11(3):319-29.

92. Morgan PS, Bowtell RW, McIntyre DJO, Worthington BS. Correction of spatial distortion in EPI due to inhomogeneous static magnetic fields using the reversed gradient method. Journal of Magnetic Resonance Imaging. 2004;19(4):499-507.

93. Verhappen MH, Pouwels PJW, Ljumanovic R, van der Putten L, Knol DL, De Bree R, et al. Diffusion-Weighted MR Imaging in Head and Neck Cancer: Comparison between Half-Fourier Acquired Single-Shot Turbo Spin-Echo and EPI Techniques. Am J Neuroradiol. 2012;33(7):1239-46.

94. Schouten CS, de Bree R, van der Putten L, Noij DP, Hoekstra OS, Comans EF, et al. Diffusion-weighted EPI- and HASTE-MRI and 18F-FDG-PET-CT early during chemo-

radiotherapy in advanced head and neck cancer. Quantitative imaging in medicine and surgery. 2014;4(4):239-50.

95. Chenevert TL, Galban CJ, Ivancevic MK, Rohrer SE, Londy FJ, Kwee TC, et al. Diffusion Coefficient Measurement Using a Temperature-Controlled Fluid for Quality Control in Multicenter Studies. Journal of Magnetic Resonance Imaging. 2011;34(4):983-7.

96. Shankar LK, Hoffman JM, Bacharach S, Graham MM, Karp J, Lammertsma AA, et al. Consensus recommendations for the use of 18F-FDG PET as an indicator of therapeutic response in patients in National Cancer Institute Trials. J Nucl Med. 2006;47(6):1059-66.

97. Malyarenko D, Galban CJ, Londy FJ, Meyer CR, Johnson TD, Rehemtulla A, et al. Multi-system repeatability and reproducibility of apparent diffusion coefficient measurement using an ice-water phantom. Journal of Magnetic Resonance Imaging. 2013;37(5):1238-46.

98. Kolff-Gart AS, Pouwels PJ, Noij DP, Ljumanovic R, Vandecaveye V, de Keyzer F, et al. Diffusion-weighted imaging of the head and neck in healthy subjects: reproducibility of ADC values in different MRI systems and repeat sessions. AJNR American journal of neuroradiology. 2015;36(2):384-90.

99. Declaration of Helsinki (1964). Brit Med J. 1996;313(7070):1448-9.

100. Bockmuhl U, Ishwad CS, Ferrell RE, Gollin SM. Association of 8p23 deletions with poor survival in head and neck cancer. Otolaryngology--head and neck surgery : official journal of American Academy of Otolaryngology-Head and Neck Surgery. 2001;124(4):451-5.

101. Landesa-Vazquez I, Alba-Castro JL, Mera-Iglesias M, Aramburu-Nunez D, Lopez-Medina A, Munoz-Garzon V. ARTFIBio: A Cross-Platform Image Registration Tool for Tumor Response Quantification in Head and Neck Cancer. 2014 Ieee-Embs International Conference on Biomedical and Health Informatics (Bhi). 2014:149-52.

102. Mattes D, Haynor DR, Vesselle H, Lewellen TK, Eubank W. Nonrigid multimodality image registration. P Soc Photo-Opt Ins. 2001;2(27):1609-20.

103. Chenevert TL, Stegman LD, Taylor JM, Robertson PL, Greenberg HS, Rehemtulla A, et al. Diffusion magnetic resonance imaging: an early surrogate marker of therapeutic efficacy in brain tumors. Journal of the National Cancer Institute. 2000;92(24):2029-36.

104. IAEA. Quantitative Nuclear Medicine Imaging: Concepts,Requirements and Methods. IAEA Library. 2014.

105. MacManus M, Nestle U, Rosenzweig KE, Carrio I, Messa C, Belohlavek O, et al. Use of PET and PET/CT for radiation therapy planning: IAEA expert report 2006-2007. Radiother Oncol. 2009;91(1):85-94.

106. Cohen J. The statistical power of abnormal-social psychological research: a review. Journal of abnormal and social psychology. 1962;65:145-53.

107. R project Available from: http://www.gnu.org/licenses/gpl.html.

108. Iglesias MM, Nunez DA, Claudio JLD, Medina AL, Landesa-Vazquez I, Gomez FS, et al. Multimodality Functional Imaging in Radiation Therapy Planning: Relationships between Dynamic Contrast-Enhanced MRI, Diffusion-Weighted MRI, and 18F-FDG PET. Comput Math Method M. 2015.

109. Ludeke KM, Roschmann P, Tischler R. Susceptibility artefacts in NMR imaging. Magnetic resonance imaging. 1985;3(4):329-43.

110. Ruthotto L, Kugel H, Olesch J, Fischer B, Modersitzki J, Burger M, et al. Diffeomorphic susceptibility artifact correction of diffusion-weighted magnetic resonance images. Phys Med Biol. 2012;57(18):5715-31.

111. ACID. ACID-Artefact correction in diffusion MRI 2013. Available from: http://www.diffusiontools.com/. .

112. ACID. ACID-Artefact correction in diffusion MRI. 2013.

113. Schneider CA, Rasband WS, Eliceiri KW. NIH Image to ImageJ: 25 years of image analysis. Nat Methods. 2012;9(7):671-5.

114. Lu Y, Jansen JF, Stambuk HE, Gupta G, Lee N, Gonen M, et al. Comparing primary tumors and metastatic nodes in head and neck cancer using intravoxel incoherent motion imaging: a preliminary experience. Journal of computer assisted tomography. 2013;37(3):346-52.

115. Lu YG, Jansen JFA, Mazaheri Y, Stambuk HE, Koutcher JA, Shukla-Dave A. Extension of the intravoxel incoherent motion model to non-gaussian diffusion in head and neck cancer. Journal of Magnetic Resonance Imaging. 2012;36(5):1088-96.

116. Landis CS, Li X, Telang FW, Molina PE, Palyka I, Vetek G, et al. Equilibrium transcytolemmal water-exchange kinetics in skeletal muscle in vivo. Magnetic resonance in medicine. 1999;42(3):467-78.

117. Altman PL, Katz DD. Blood and other body fluids. Washington,: Federation of American Societies for Experimental Biology; 1961. xvii, 540 p. p.

118. Bagher-Ebadian H, Jain R, Nejad-Davarani SP, Mikkelsen T, Lu M, Jiang Q, et al. Model selection for DCE-T1 studies in glioblastoma. Magnetic resonance in medicine. 2012;68(1):241-51.

119. Raunig DL, McShane LM, Pennello G, Gatsonis C, Carson PL, Voyvodic JT, et al. Quantitative imaging biomarkers: a review of statistical methods for technical performance assessment. Statistical methods in medical research. 2015;24(1):27-67.

120. Krynicki K, Green CD, Sawyer DW. Pressure and Temperature-Dependence of Self-Diffusion in Water. Faraday Discuss. 1978;66:199-208.

121. Pang Y, Turkbey B, Bernardo M, Kruecker J, Kadoury S, Merino MJ, et al. Intravoxel incoherent motion MR imaging for prostate cancer: an evaluation of perfusion fraction

and diffusion coefficient derived from different b-value combinations. Magnetic resonance in medicine. 2013;69(2):553-62.

122. Tofts PS, Lloyd D, Clark CA, Barker GJ, Parker GJ, McConville P, et al. Test liquids for quantitative MRI measurements of self-diffusion coefficient in vivo. Magnetic resonance in medicine. 2000;43(3):368-74.

123. Vandecaveye V, Dirix P, De Keyzer F, de Beeck KO, Vander Poorten V, Hauben E, et al. Diffusion-Weighted Magnetic Resonance Imaging Early after Chemoradiotherapy to Monitor Treatment Response in Head-and-Neck Squamous Cell Carcinoma. Int J Radiat Oncol. 2012;82(3):1098-107.

124. Mills R. Self-Diffusion in Normal and Heavy-Water in Range 1-45 Degrees. J Phys Chem-Us. 1973;77(5):685-8.

125. Jemal A, Siegel R, Xu J, Ward E. Cancer statistics, 2010. CA: a cancer journal for clinicians. 2010;60(5):277-300.

126. Gawlitza M, Purz S, Kubiessa K, Boehm A, Barthel H, Kluge R, et al. In Vivo Correlation of Glucose Metabolism, Cell Density and Microcirculatory Parameters in Patients with Head and Neck Cancer: Initial Results Using Simultaneous PET/MRI. PloS one. 2015;10(8):e0134749.

127. Han M, Kim SY, Lee SJ, Choi JW. The Correlations Between MRI Perfusion, Diffusion Parameters, and 18F-FDG PET Metabolic Parameters in Primary Head-and-Neck Cancer: A Cross-Sectional Analysis in Single Institute. Medicine. 2015;94(47):e2141.

128. Ng SH, Liao CT, Lin CY, Chan SC, Lin YC, Yen TC, et al. Dynamic contrast-enhanced MRI, diffusion-weighted MRI and F-FDG PET/CT for the prediction of survival in oropharyngeal or hypopharyngeal squamous cell carcinoma treated with chemoradiation. European radiology. 2016.

129. Thorwarth D, Beyer T, Boellaard R, de Ruysscher D, Grgic A, Lee JA, et al. Integration of FDG-PET/CT into external beam radiation therapy planning: technical aspects and recommendations on methodological approaches. Nuklearmedizin Nuclear medicine. 2012;51(4):140-53.

130. Dirix P, Vandecaveye V, De Keyzer F, Stroobants S, Hermans R, Nuyts S. Dose painting in radiotherapy for head and neck squamous cell carcinoma: value of repeated functional imaging with (18)F-FDG PET, (18)F-fluoromisonidazole PET, diffusion-weighted MRI, and dynamic contrast-enhanced MRI. J Nucl Med. 2009;50(7):1020-7.

131. Welsh L, Panek R, McQuaid D, Dunlop A, Schmidt M, Riddell A, et al. Prospective, longitudinal, multi-modal functional imaging for radical chemo-IMRT treatment of locally advanced head and neck cancer: the INSIGHT study. Radiation oncology. 2015;10:112.

132. Subesinghe M, Scarsbrook AF, Sourbron S, Wilson DJ, McDermott G, Speight R, et al. Alterations in anatomic and functional imaging parameters with repeated FDG PET-CT and MRI during radiotherapy for head and neck cancer: a pilot study. BMC cancer. 2015;15:137.

133. Paidpally V, Chirindel A, Lam S, Agrawal N, Quon H, Subramaniam RM. FDG-PET/CT imaging biomarkers in head and neck squamous cell carcinoma. Imaging in medicine. 2012;4(6):633-47.

134. Berwouts D, Olteanu LA, Duprez F, Vercauteren T, De Gersem W, De Neve W, et al. Three-phase adaptive dose-painting-by-numbers for head-and-neck cancer: initial results of the phase I clinical trial. Radiother Oncol. 2013;107(3):310-6.

135. Chen LH, Liu M, Bao J, Xia YB, Zhang JQ, Zhang L, et al. The Correlation between Apparent Diffusion Coefficient and Tumor Cellularity in Patients: A Meta-Analysis. PloS one. 2013;8(11).

136. Varoquaux A, Rager O, Lovblad KO, Masterson K, Dulguerov P, Ratib O, et al. Functional imaging of head and neck squamous cell carcinoma with diffusion-weighted MRI

and FDG PET/CT: quantitative analysis of ADC and SUV. European journal of nuclear medicine and molecular imaging. 2013;40(6):842-52.

137. Choi SH, Paeng JC, Sohn CH, Pagsisihan JR, Kim YJ, Kim KG, et al. Correlation of 18F-FDG uptake with apparent diffusion coefficient ratio measured on standard and high b value diffusion MRI in head and neck cancer. J Nucl Med. 2011;52(7):1056-62.

138. Nakajo M, Nakajo M, Kajiya Y, Tani A, Kamiyama T, Yonekura R, et al. FDG PET/CT and Diffusion-Weighted Imaging of Head and Neck Squamous Cell Carcinoma Comparison of Prognostic Significance Between Primary Tumor Standardized Uptake Value and Apparent Diffusion Coefficient. Clin Nucl Med. 2012;37(5):475-80.

139. Nakamatsu S, Matsusue E, Miyoshi H, Kakite S, Kaminou T, Ogawa T. Correlation of apparent diffusion coefficients measured by diffusion-weighted MR imaging and standardized uptake values from FDG PET/CT in metastatic neck lymph nodes of head and neck squamous cell carcinomas. Clinical imaging. 2012;36(2):90-7.

140. Preda L, Conte G, Bonello L, Giannitto C, Travaini LL, Raimondi S, et al. Combining standardized uptake value of FDG-PET and apparent diffusion coefficient of DW-MRI improves risk stratification in head and neck squamous cell carcinoma. European radiology. 2016.

141. Vandecaveye V, Dirix P, De Keyzer F, de Beeck KO, Vander Poorten V, Roebben I, et al. Predictive value of diffusion-weighted magnetic resonance imaging during chemoradiotherapy for head and neck squamous cell carcinoma. European radiology. 2010;20(7):1703-14.

142. Hatakenaka M, Nakamura K, Yabuuchi H, Shioyama Y, Matsuo Y, Kamitani T, et al. Apparent diffusion coefficient is a prognostic factor of head and neck squamous cell carcinoma treated with radiotherapy. Japanese journal of radiology. 2014;32(2):80-9.

143. Srinivasan A, Chenevert TL, Dwamena BA, Eisbruch A, Watcharotone K, Myles JD, et al. Utility of pretreatment mean apparent diffusion coefficient and apparent diffusion

coefficient histograms in prediction of outcome to chemoradiation in head and neck squamous cell carcinoma. Journal of computer assisted tomography. 2012;36(1):131-7.

144. Min M, Lee MT, Lin P, Holloway L, Wijesekera D, Gooneratne D, et al. Assessment of serial multi-parametric functional MRI (diffusion-weighted imaging and R2*) with (18) F-FDG-PET in patients with head and neck cancer treated with radiation therapy. The British journal of radiology. 2016;89(1058):20150530.

145. Ang KK, Harris J, Wheeler R, Weber R, Rosenthal DI, Nguyen-Tan PF, et al. Human papillomavirus and survival of patients with oropharyngeal cancer. The New England journal of medicine. 2010;363(1):24-35.

146. Titz B, Jeraj R. An imaging-based tumour growth and treatment response model: investigating the effect of tumour oxygenation on radiation therapy response. Phys Med Biol. 2008;53(17):4471-88.

147. Thorwarth D, Alber M. Implementation of hypoxia imaging into treatment planning and delivery. Radiother Oncol. 2010;97(2):172-5.

148. Yankeelov TE, Lepage M, Chakravarthy A, Broome EE, Niermann KJ, Kelley MC, et al. Integration of quantitative DCE-MRI and ADC mapping to monitor treatment response in human breast cancer: initial results. Magnetic resonance imaging. 2007;25(1):1-13.

149. Jaffray DA, Chung C, Cooleens C, Foltz W, Keller H, Menard C, et al. Quantitative Imaging in Radiation Oncology: An Emerging Science and Clinical Service. Semin Radiat Oncol. 2015;25(4):292-304.

150. Chen YB, Liu XY, Zheng DC, Xu LY, Hong L, Xu Y, et al. Diffusion-weighted magnetic resonance imaging for early response assessment of chemoradiotherapy in patients with nasopharyngeal carcinoma. Magnetic resonance imaging. 2014;32(6):630-7.

151. Le Bihan D, Poupon C, Amadon A, Lethimonnier F. Artifacts and pitfalls in diffusion MRI. Journal of magnetic resonance imaging : JMRI. 2006;24(3):478-88.

152. Veeraraghavan H, Do RKG, Reidy DL, Deasy JO. Simultaneous segmentation and iterative registration method for computing ADC with reduced artifacts from DW-MRI. Medical physics. 2015;42(5):2249-60.

153. Xiang QS, Ye FQ. Correction for geometric distortion and N/2 ghosting in EPI by phase labeling for additional coordinate encoding (PLACE). Magnetic resonance in medicine. 2007;57(4):731-41.

154. Lavdas I, Behan KC, Papadaki A, McRobbie DW, Aboagye EO. A phantom for diffusion-weighted MRI (DW-MRI). Journal of Magnetic Resonance Imaging. 2013;38(1):173-9.

155. Gatidis S, Schmidt H, Martirosian P, Schwenzer NF. Development of an MRI Phantom for Diffusion-Weighted Imaging with Independent Adjustment of Apparent Diffusion Coefficient Values and T2 Relaxation Times. Magnetic resonance in medicine. 2014;72(2):459-63.

156. Patel TR, McHugh BJ, Bi WL, Minja FJ, Knisely JP, Chiang VL. A comprehensive review of MR imaging changes following radiosurgery to 500 brain metastases. AJNR American journal of neuroradiology. 2011;32(10):1885-92.

157. Soliman H, Das S, Larson DA, Sahgal A. Stereotactic radiosurgery (SRS) in the modern management of patients with brain metastases. Oncotarget. 2016;7(11):12318-30.

158. Jakubovic R, Zhou S, Heyn C, Soliman H, Zhang L, Aviv R, et al. The predictive capacity of apparent diffusion coefficient (ADC) in response assessment of brain metastases following radiation. Clinical & experimental metastasis. 2016;33(3):277-84.

159. Jakubovic R, Sahgal A, Soliman H, Milwid R, Zhang L, Eilaghi A, et al. Magnetic resonance imaging-based tumour perfusion parameters are biomarkers predicting response after radiation to brain metastases. Clinical oncology. 2014;26(11):704-12.

160. Chu JP, Mak HK, Yau KK, Zhang L, Tsang J, Chan Q, et al. Pilot study on evaluation of any correlation between MR perfusion (Ktrans) and diffusion (apparent diffusion coef-

ficient) parameters in brain tumors at 3 Tesla. Cancer imaging : the official publication of the International Cancer Imaging Society. 2012;12:1-6.

161. Wesseling P, Ruiter DJ, Burger PC. Angiogenesis in brain tumors; Pathobiological and clinical aspects. J Neuro-Oncol. 1997;32(3):253-65.

162. Garcia-Barros M, Paris F, Cordon-Cardo C, Lyden D, Rafii S, Haimovitz-Friedman A, et al. Tumor response to radiotherapy regulated by endothelial cell apoptosis. Science. 2003;300(5622):1155-9.

163. Brown SL, Nagaraja TN, Aryal MP, Panda S, Cabral G, Keenan KA, et al. MRI-Tracked Tumor Vascular Changes in the Hours after Single-Fraction Irradiation. Radiation research. 2015;183(6):713-21.

164. Park HJ, Griffin RJ, Hui S, Levitt SH, Song CW. Radiation-induced vascular damage in tumors: implications of vascular damage in ablative hypofractionated radiotherapy (SBRT and SRS). Radiation research. 2012;177(3):311-27.

165. Horsman MR, Nielsen T, Ostergaard L, Overgaard J. Radiation administered as a large single dose or in a fractionated schedule: Role of the tumour vasculature as a target for influencing response. Acta oncologica. 2006;45(7):876-80.

Appendix

Appendix

Publications:

- Moisés Mera Iglesias**, David Aramburu Núñez**, José Luis del Olmo Claudio, Antonio López Medina, Iago Landesa-Vázquez, Francisco Salvador Gómez, Brandon Driscoll, Catherine Coolens, José L. Alba Castro, Victor Muñoz. *Multimodality Functional Imaging in Radiation Therapy Planning: Relationships between Dynamic Contrast-Enhanced MRI, Diffusion-Weighted MRI, and 18F-FDG PET*. Computational and Mathematical Methods in Medicine. Article ID 103843 (2015).

- Landesa-Vazquez, I.. Alba-Castro, J.L. ; Mera-Iglesias, M. **; Aramburu-Nunez, D**. ; Lopez-Medina, A. ; Munoz-Garzon, V. *ARTFIBio: A cross-platform image registration tool for tumor response quantification in head and neck cancer.* Biomedical and Health Informatics (BHI), 2014 IEEE-EMBS International Conference. 149 – 152. DOI: 10.1109/BHI.2014.6864326.

- Gonzalo Pradas Montilla, Victor M Muñoz-Garzón, Julio Vázquez Rodriguez, Jorge Pereira, Juan José Legarra, Rocío Casais, **David Aramburu Núñez** and Manuel Caeiro Muñoz. *Extra-Corporeal Membrane Oxygenation for Arrested Lung Ablative Radiation Therapy*. J Anesth Clin Res (2015), 6:1.

- I Hernández Girón, J Valverde Morán, R Méndez Fernández, **D Aramburu N**úñez, C Núñez de Villavicencio y A Calzado Cantera. *Estudio de los sistemas de modulación de dosis en dos equipos de tomografía computarizada multicorte*. Rev Fis Med (2009); 10(2):115-122.

Abstracts:

- ***Oral Presentations**:*

  - **David Aramburu Nuñez** , Kathryn Beal , Vaios Hatzoglou , Andrei Holodny , Ramesh Paudyal , Yonggang Lu , Joseph O Deasy , and Amita Shukla-Dave. *Assessment of early treatment response by IVIM DW-MRI and DCE-MRI in patients with brain metastases treated with stereotactic radiosurgery*.. ISMRM 24th Annual Meeting-Singapore (2016)*.

    ***Awarded with Merit Summa Cum Laude - Selection is based on meritorious work in the field.**

  - **David Aramburu Nuñez**, Antonio Lopez Medina, Moises Mera Iglesias, Francisco Salvador Gomez, Vaios Hatzoglou, Ramesh Paudyal, Alfonso Calzado, Joseph O Deasy, Amita Shukla-Dave and Victor M Muñoz. *Multimodality functional imaging in radiation therapy during treatment: relationship between DW-MRI and 18F FDG PET in head and neck squamous cell carcinoma*. ISMRM 24th Annual Meeting-Singapore (2016)*.

    ***Awarded with Merit Summa Cum Laude- Selection is based on meritorious work in the field.**

  - Mitchell C. Raeside, Andrea Agostini, Richard K.G. Do, Amita Shukla-Dave, **David Aramburu Nunez**, Ramesh Paudyal, Olga Smelianskaia, Monika Khan, David P. Kelsen, Lorenzo Mannelli. *Pilot Study of Rapid MR Pancreas Screening for Patients with BRCA Mutation Undergoing Screening Breast MRI – Preliminary Data*. ISMRM 24th Annual Meeting-Singapore (2016).

  - A. López Medina, **D. Aramburu**, M. Mera, J. Del Olmo, B. Andrade, V.Ochagavia, I. Nieto, M. Salgado, A. Calzado, V. Muñoz. *Tumor response: A multiparametric function*. Radiother & Oncol 111:S1. (2014) *.

    ***Poster Discussion at ESTRO.**

- ***Traditional and Electronic Posters:***

  - Ramesh Paudyal, Nadeem Riaz, Jung Hun Oh, Praveen Venigalla, Jiango Li, Vaois Hatzoglou, **David Aramburu Nunez,** Yonggang Lu, Joseph O. Deasy, and Nancy Lee, Amita Shukla-Dave. *Characterization of HPV positive oropharyngeal tumors using intravoxel incoherent motion DW-MRI before and during radiation therapy*. ISMRM 24th Annual Meeting-Singapore (2016).

  - Andrea Agostini, Mitchell C. Raeside, Richard K.G. Do, Amita Shukla-Dave, **David Aramburu Nunez,** Ramesh Paudyal, Olga Smelianskaia, Maggie M Fung, Monika Khan, David P. Kelsen, and Lorenzo Mannelli. *Implementing a fast MR screening protocol for pancreas in patients with mutations of BRCA1 and BRCA2: Preliminary data on Diffusion-Weighted Images*.. ISMRM 24th Annual Meeting-Singapore (2016).

  - Suchandrima Banerjee, **David Aramburu-Nunez**, Ramesh Paudyal, Thomas Chenevert, Michael Boss, and Amita Shukla-Dave. *Does reduced FOV Diffusion Weighted Imaging inherently yield lower ADC?*. ISMRM 24th Annual Meeting-Singapore (2016).

  - A. Lopez Medina, S. Reigosa, J. del Olmo, **D. Aramburu Nunez**, F. Salvador, I. Landesa, J. Alba, M. Salgado, I. Nieto, V. Ochagavia, V. Muñoz. *Improving Tumor Response Assessment using DWMRI corrected by reversed gradient method and DCEMRI*. ESTRO 35; Turín (2016).

  - **D. Aramburu Nuñez**, J. del Olmo Claudio, A. Lopez Medina, M. Mera Iglesias, F. Salvador, V. Ochagavia, I. Nieto, F. del Moral, A. Calzado, V. Muñoz. *Multimodality Functional Imaging for Biologically Guide Radiation Therapy***.** 3rd ESTRO forum; Barcelona (2015).

  - G. Pradas Montilla1, V. Muñoz Garzón, J. Vazquez Rodríguez, **D. Aramburu Núñez**, J. Pereira, J.J. Legarra, R. Casais, A. Teijeiro, E. Hernandez, A. Gonzalez,

J.R. Guitián, J.M. Nogueiras, M. Salgado, M. Hernandez, M. Caeiro. *"A New SBRT Technique with the Lung totally arrested (Arrested Lung Ablative Radiotherapy - ALART)."*. 3rd ESTRO forum; Barcelona (2015).

- Pradas-Montilla G, Muñoz-Garzón VM, **Aramburu-Núñez D**, Vázquez-Rodríguez J, Pereira J, Legarra JJ, Casais R, Teijeiro-García A, Hernandez Piñeiro E, GonzalezA, Guitián JR, Nogueiras JM, Salgado M, Hernandez M, Caeiro-Muñoz *Arrested Lung for External Radiotherapy Hypofractionated in Lung Cancer (Arrested Lung Ablative Radiotherapy - ALART)*. M. 4D Treatment Planning Workshop 2014. London (Cookham).University College of London (UCL) and Institute of Cancer Research (ICR). (28-29 November 2014)

- Munoz-Garzon, V.;Pradas, G; Vazquez, J; **Aramburu, D**; Legarra J.J; Pereira, J; Calvo,F; Hernandez, E; Salgado, M; Triñanes, A; Gonzalez, A; Martinez; M; Vazquez de la Torre, M; Vilariño, C; Marcos; P; Caeiro. *Nueva técnica radioterápia estereotáctica fraccionada con pulmón detenido (ALART*), M. Premio a la mejor comunicación oral en el XIV Congreso de la Sociedad Española de Radiocirugia. 24, 25, 26 Septiembre 2014. Baiona (PONTEVEDRA).

- Nuñez, A; Willisch, P; Martinez, M; **Aramburu, D**; Ochagavia, V; Meira, B; Gonzalez, A; Triñanes, A; Nieto, I; Martinez, P; Teijeiro, A. Muñoz, V. *Radiocirugía en la Neuralgia del Trigémino*. XIV Congreso de la Sociedad Española de Radiocirugia. 24, 25, 26 Septiembre 2014. Baiona (PONTEVEDRA).

- Pradas, G; Munoz-Garzon, V; Vazquez, J; Pereira, J; Calvo, F; Legarra, J; Pita-Romero, R; Hernandez, M; Hernandez, E; Piñón, M; **Aramburu, D**; Caeiro, M. *Oxigenación de membrane extracorporeal para la radioterapia ablative con pulmóndetenido (ALART)*. ExperienciaInicial. XIV Congreso de la Sociedad Española de Radiocirugia. 24, 25, 26 Septiembre 2014. Baiona (PONTEVEDRA).

- Nuñez, A; Triñanes, A; Alvarez, M; **Aramburu, D**; Willisch, P; Martinez, M;

Hernandez, M; Medina, M; Ochagavia, V; Rey, P; Nieto, I; Marcos, P; Lopez, M; Caeiro, M;Hernandez, E; Teijeiro, A. Muñoz, V; Salgado, M. *Dispositivos de Inmovilización con materiales avanzados para adecuar los dispositivos a las técnicas nuevas de estereotaxia*.. XIV Congreso de la Sociedad Española de Radiocirugia. 24, 25, 26 Septiembre 2014. Baiona (PONTEVEDRA).

- Munoz-Garzon, V.; Pradas, G; Vazquez, J; **Aramburu, D;** J.J; Pereira, J; Calvo, F; D; Legarra; Pita, R; Hernandez, E; Piñon, M; Triñanes, A; Gonzalez, A; Nuñez, A; Caeiro, M; Willisch, P; Nuñez, M; Arenas, L; Salgado, M. *Segundo Caso tratado con la nueva técnica de radioterapia estereotáctica fraccionada con pulmón detenido (ALART)*. XIV Congreso de la Sociedad Española de Radiocirugia. 24, 25, 26 Septiembre 2014. Baiona (PONTEVEDRA).

- **D. Aramburu N**úñez, M. Mera Iglesias, L. Pereira Ferradas, I. Landesa Vázquez, V. Ochagavía; Galilea, Í. Nieto Regueira, J. Nogueiras Alonso, J. Mañas Uxó, A. López Medina, V. Múñoz Garzón. *Artfibio project: Developing tools to see the treatment response*. Reports of Practical Oncology & Radiotherapy, Volume18, Supplement 1 June 2013, Page S129.

- **D. Aramburu N**úñ**ez**, M. Mera Iglesias, L. Pereira Ferradás, R. Leiva Urbina, I. Landesa Vazquez, A. Lopez Medina, V. Ochagavia Galilea, I. Nieto Regueira, F. Salvador Gomez, V. Muñoz Garzón. *Adaptative radiotherapy based on functional images***.** Reports of Practical Oncology & Radiotherapy, Volume18, Supplement1, June2013, PageS238.

- L. Pereira Ferradas, M. Mera Iglesias, **D. Aramburu N**úñ**ez**, A. Teijeiro, B. Andrade, J. Vazquez, D. Medal, F. Salvador Gomez, M. Salgado, A. Lopez Medina. *Modelling and commissioning of a radiosurgery cone system for trigeminal neuralgia*... Reports of Practical Oncology & Radiotherapy, Volume18, Supplement1, June2013, PageS345-6.

- B. Meira Montenegro ,A. Alfaya Virzi, A. Lamas Lorenzo, L. Pereira Ferradas, M. Mera Iglesias, **D. Aramburu Nuñez**, M.Salgado Fernandez, M.Hernandez Herrera, V. Muñoz Garzon. *Verification of positioning using a new immobilization system for craniospinal pediatric treatment*.. Reports of Practical Oncology & Radiotherapy, Volume18, Supplement1, June 2013, Page S384.

- Lopez Medina, **D. Aramburu**, M.Mera, L.Pereira, .Landesa, V.Ochagavia, I.Nieto, J.Mañas, J.M.Nogueiras, V.Muñoz. *ARTFIBio Project: quantifying tumor response voxel by voxel*.. Radiother & Oncol 2013; 106:S329.

- M.Mera, L.Pereira, **D. Aramburu**, A.Teijeiro, B.Andrade, J.Vazquez, A.LopezMedina, D.Medal F. Salvador, M.Salgado *Modelling and Commissioning a Brainlab© radiosurgery cone system for trigeminal neuralgia*. Radiother & Oncol 2013;106:S433.